

Dissertation  
submitted to the  
Combined Faculties for the Natural Sciences and for Mathematics  
of the Ruperto-Carola University of Heidelberg, Germany  
for the degree of  
Doctor of Natural Sciences

presented by

M. Sc.: Cheng-Ping Luo

born in: Miao-Li / TAIWAN

Oral examination: June 23, 2004



Detection of Antibody-Antigen Reactions  
using Surface Acoustic Wave and  
Electrochemical Immunosensors

Referees: Prof. Dr. Siegfried Hunklinger  
Priv. Doz. Dr. Gerhard Fahsold



## **Detektion von Antikörper-Antigen Reaktionen mit Hilfe von Oberflächenwellen- und elektrochemischen Sensoren**

Traditionelle Immunoassays für den Nachweis von spezifischen Antikörper-Antigen Reaktionen sind teuer, zeitaufwändig und kompliziert. In dieser Arbeit werden Immunosensoren vorgestellt, die mit akustischen Oberflächenwellen oder elektrochemischen Verfahren beruhen und die die hohe Spezifität konventioneller Immunoassays mit der Echtzeiterfassung kombinieren. Oberflächenwellen-Bauelemente sind in der Telekommunikation weit verbreitet, darüber hinaus kann ihre hohe Empfindlichkeit gegenüber Massenbelegungen auch für Mikrowaagen verwendet werden. Die Massenänderung bei einer Immunoreaktion kann deshalb mit Oberflächenwellen-Sensoren beobachtet werden. In dieser Arbeit wurden akustische Oberflächenwellen auf der Oberfläche von Lithiumtantalat über induktiv gekoppelte Interdigitalwandler angeregt, um Antikörper-Antigen Reaktionen zu detektieren. Die elektrischen Eigenschaften der Oberfläche eines Sensors ändern sich ebenfalls, wenn eine Immunoreaktion stattfindet, was mit einem elektrochemischen Sensor nachgewiesen werden kann. Es wurden kapazitiv gekoppelte Sensoren mit zwei und vier Elektroden hergestellt, um die Impedanzänderung an der Sensoroberfläche zu messen. Effekte aufgrund der Wechselwirkung zwischen den elektrischen Feldern und der elektrischen Doppelschicht werden ebenfalls diskutiert. Schließlich kann auch die Antikörperaffinität sowohl mit akustischen Oberflächenwellen als auch mit elektrochemischen Sensoren gemessen werden, was auf die großen Einsatzmöglichkeiten im klinischen Bereich hinweist.

## **Detection of antibody-antigen reactions using surface acoustic wave and electrochemical immunosensors**

Traditional immunoassays for the detection of specific antibody-antigen reactions are expensive, time-consuming and non-trivial. In this work, immunosensors based on surface acoustic wave and electrochemical techniques are presented, which provide high specificity like conventional immunoassays and the real-time monitoring of immunoreactions can be achieved. Surface acoustic wave devices have been widely used in the telecommunication. Besides their extremely high sensitivity to mass loading they can be utilized for microbalances. The mass change during an antibody-antigen binding can be therefore observed by SAW sensors. In this work, ultrasonic waves were generated on the surface of lithium tantalate by inductively coupled interdigital transducers to detect antibody-antigen reactions. The electrical properties at the surface of a sensor are also changed when an antibody-antigen reaction occurs. This can be detected by electrochemical sensors. Capacitively coupled two- and four-electrode sensors were developed to measure the impedance change at the sensor surface. Effects of the interaction between electric fields and the electrical double layer near the liquid-solid interface will also be discussed. Finally, the antibody affinities can be also measured with both SAW and electrochemical sensors, indicating a high potential in clinical application.



# Table of Contents

Chapter 1 Introduction	1
Chapter 2 Biological aspect of immunoreaction	5
2.1 Immune responses .....	5
2.2 Antigen recognition.....	6
2.3 Antibody structure.....	7
2.4 Antibody specificity and affinity.....	8
2.5 Kinetics of antigen-antibody interactions.....	9
Chapter 3 Theory of surface acoustic wave sensors	11
3.1 Elasticity in solids.....	11
3.1.1 Stress and strain.....	11
3.1.2 Elastic constitutive relation.....	13
3.1.3 Simplification of the elastic stiffness constant.....	14
3.1.4 Isotropic solid.....	15
3.1.5 Piezoelectric materials.....	16
3.2 Wave equations.....	17
3.2.1 Wave equation for non-piezoelectric solid.....	17
3.2.2 Wave equation for piezoelectric solids .....	18
3.3 Solutions of the wave equations.....	19
3.3.1 Bulk acoustic waves in isotropic solids .....	19
3.3.2 Surface acoustic waves in isotropic solids.....	20

3.3.3 Acoustic waves in piezoelectric solids.....	25
3.3.4 Rayleigh wave at liquid-solid interface.....	27
3.3.5 Shear horizontal wave.....	28
<b>3.4 Response of surface wave sensor.....</b>	<b>31</b>
3.4.1 Effect of elastic thin film coating (mass loading).....	32
3.4.2 Effect of viscosity.....	33
3.4.3 Effect of electrical conductivity.....	34
3.4.4 Effect of temperature.....	37
<b>Chapter 4 Design of surface acoustic wave immunosensors</b>	<b>39</b>
<b>4.1 Excitation and detection of surface waves.....</b>	<b>39</b>
4.1.1 Interdigital transducers.....	39
4.1.2 Delta function model.....	40
4.1.3 Double-electrode transducer.....	41
4.1.4 Impedance of interdigital transducers.....	42
<b>4.2 Contactless SAW device.....</b>	<b>44</b>
4.2.1 Inductively coupled SAW sensor.....	44
4.2.2 Impedance matching.....	45
4.2.3 Fabrication of SAW sensor.....	47
4.2.4 SiO <sub>2</sub> coating as waveguide.....	48
4.2.5 Measurement setup.....	50
<b>4.3 Measurements using SAW immunosensor.....</b>	<b>50</b>
4.3.1 Principle of measurement.....	50
4.3.2 Surface modification.....	52
4.3.3 Results.....	53
4.3.4 Polymethyl methacrylate (PMMA) coating.....	56
<b>Chapter 5 Theory of capacitively coupled electrochemical sensors</b>	<b>57</b>
<b>5.1 Electrical model for bare electrode.....</b>	<b>57</b>

5.2 Electrical model for insulated electrodes .....	58
5.3 Sensitivity of capacitively coupled sensors .....	59
<b>Chapter 6 Design of capacitively coupled electrochemical sensors</b>	<b>63</b>
6.1 Two-probe Sensor.....	63
6.1.1 Design and production of the electrode.....	63
6.1.2 Electrical Model.....	63
6.1.3 Required Electronics.....	64
6.1.4 System Setup.....	68
6.2 Four-probe Sensor.....	69
6.2.1 Design and production of the electrodes .....	69
6.2.2 Electrical Model.....	69
6.2.3 Required Electronics and Total Setup.....	70
6.2.4 System Setup.....	76
6.3 Measurements .....	77
6.3.1 Bare electrode.....	77
6.3.2 Antibody Immobilization.....	79
6.3.3 PMMA Coating .....	80
6.3.4 Polystyrene Coating.....	81
6.3.5 Influence of the gap width.....	82
<b>Chapter 7 Antibody activities in liquid - Effects of the AC electrokinetics</b>	<b>85</b>
7.1 Dielectrophoresis.....	87
7.2 Brownian motion and diffusion.....	91
7.3 Electrohydrodynamics.....	93
7.3.1 Joule heating by applied AC voltage .....	93
7.3.2 Coulomb and dielectric force.....	96
7.3.3 Convection .....	99

7.4 Electro-osmosis .....	100
7.4.1 Electrical double layer .....	100
7.4.2 Thickness of layers determination .....	101
7.4.3 Electro-osmosis .....	104
7.5 Binding kinetics of immunoreaction.....	108
Chapter 8 Summary and prospect	111
Appendix A	115
Reference	117

# Chapter 1

## Introduction

In our daily life, sensors are widely utilized in many fields. For example, from the thermometer in the electric cooker to the oxygen sensor in the car, they become the most important equipment in the past decades, not to mention the applications in the exploration of the universe in the 21<sup>st</sup> century. People may not know how these sensors work and where they hide, but they do deeply influence the efficiency and convenience of articles for daily use.

A sensor can convert the received physical or chemical stimulus, such as thermal, electromagnetic, magnetism, pressure, acoustic energies...etc, to interpretable, easily realized output signals. Likewise, a biosensor is defined as *a compact analytical device in incorporating a biological material or biologically-derived sensing element*, such as tissue, microorganisms, organelles, cell receptors, enzymes, antibodies, nucleic acids etc, *either integrated within or intimately associated with a physicochemical transducer or transducing microsystem, which may be optical, electrochemical, thermometric, piezoelectric or magnetic*. The usual aim of a biosensor is to produce either discrete or continuous digital electronic signals which are proportional to a single analyte or a related group of analytes [Turner 1987]. The principle of a biosensor is shown in Fig.1.

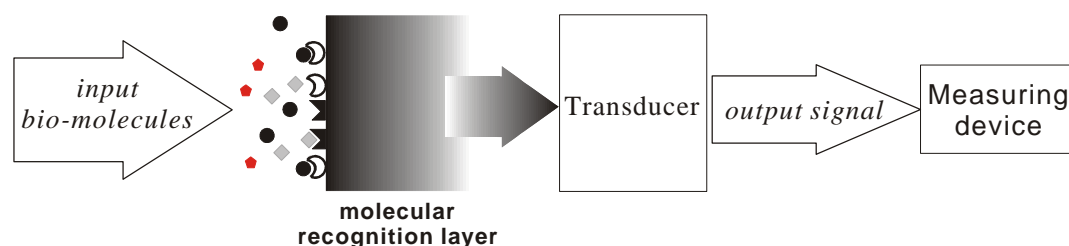


*Fig.1 Schematic diagram of the biosensor principle. Biological samples are selected specifically by the recognition elements of the biosensor and any physical or chemical property changes of the elements are transferred into measuring device by transducers.*

There are many applications of biosensors, for example, clinical diagnosis, food and drink production, pollution monitoring, pharmaceutical and drug analysis, toxic gases detection [Rogers 1996]. Biosensors concerned with monitoring merely antibody-antigen interactions can also be termed immunosensors [North 1985]. The detecting methods of immunosensors are based on the same principle of most commercial immunoassays, i.e. the solid-phase adsorption, while the read-out methods are quite different. Solid-phase adsorption means that either antibodies or antigens are immobilized at the sensor surface. The most commonly used read-out methods of the immunoassays are fluorescence staining and autoradiograph, for which the target objects are labelled ligands or radioactive tracers, respectively. The drawback of the commercial immunoassay is that the operation must be undertaken by professional personnel since the protocols are multifarious and complicated. Besides, it requires a long time to finish a probe, from several hours to days, and the equipments and reagents are costly.

To overcome these drawbacks, it is necessary to develop immunosensors. The advantages are:

(a) ***High specificity***

As in other immunoassays, immunosensors possess a remarkable ability to discriminate between the target analyte of interest and other similar substances or background noise with great accuracy.

(b) ***Real-time***

Since an immunosensor is an integrated system of receptor and transducers, the measurement procedures can be simplified. The time required for diagnose is reduced. The rapid interaction between antibody and antigen can be monitored and measured directly without any labels.

(c) ***Recyclable***

The sensing elements immobilized on the sensor surface can be easily regenerated for repeated usage. On the contrary, conventional immunoassays are used only once.

Much work in the development of immunosensors has been done over the past decades. For example, calorimetric immunosensors detect the heat production during an immunoreaction. Optical immunosensors utilize fiber-optic devices to measure the electromagnetic radiation absorbed or emitted by the molecules of the biological or immunological system. Electrochemical immunosensors work on the basis of potentiometric, amperometric, conductimetric transducers which convert the changes in

the electrochemical properties to electrical signals. Mass-detecting immunosensors are based on the mass change when the immunoreaction occurs, which is done with the use of piezoelectric crystals and acoustic wave techniques.

In this work, the developments of *surface acoustic wave* and electrochemical immunosensors will be introduced. Surface acoustic wave (SAW) immunosensors employ ultrasonic waves which propagate very close to the surface of piezoelectric substrate to detect the increasing mass due to the antibody-antigen interaction since they are sensitive to physical properties of the substrate surface. The surface acoustic waves are generated by imposing an alternating voltage onto the *interdigital transducers* (IDTs) deposited on the piezoelectric substrate; hence, the design of IDTs is the key to the SAW sensor development.

An alternative for detecting an immunoreaction is by measuring the changes in the electrical properties. The second type of the sensors introduced here is the electrochemical sensor, which measures the current changes during the immunoreaction with an alternating voltage source. This can be accomplished by the use of transducers with two or four electrodes on the substrate depending on the measuring principle.

The structure of this thesis is as follows: In the next chapter, a basic biological aspect of immunoreactions will be introduced. In chapter 3, the theory of surface acoustic waves and its application will be described in detail. The design of the IDTs for SAW and the integrated SAW immunosensor as well as the measurement results will be presented in chapter 4 to verify the reliability of the SAW immunosensors.

Theory and design of the electrochemical immunosensor, including the required electronic circuits, and measurement results will be discussed in chapters 5 and 6. *AC Electrokinetics*, the behavior of biomolecules on the sensor surface under the influence of liquid motion and electric field, which is generated by the voltage imposed on the electrodes, will be discussed in chapter 7. A comparison of the equilibrium constants of immunoreaction derived from the measurement results by both SAW and electrochemical immunosensors will be also presented. Summary and prospect are presented in the last chapter.



# Chapter 2

## Biological Aspect of Immunoreaction

Numbers of infectious microbes exist in our surrounding environment, such as viruses, bacteria, fungi, protozoa and multicellular parasites. Most infections in normal individuals are short-lived and leave little permanent damage since the immune system will resist infectious agents, which is offered by the functions of circulating antibodies and white blood cells. Antibodies are produced specifically to combine the antigens associated with different diseases, while white blood cells attack and destroy foreign particles in the blood and tissues, including antigen-antibody complexes. In the following sections a brief introduction to immune system and antibody-antigen interaction related to the development of immunosensor will be presented.

### 2.1 Immune responses

There are two major phases of any immune response:

1. Recognition of the pathogen or other foreign material,
2. Starting a reaction against it to eradicate it.

A variety of immune responses can be classified into two types: innate and adaptive immune responses. The innate response does not alter on repeated exposure to a given infectious agent; however, the adaptive response improves with each successive encounter with the same pathogen. Moreover, the adaptive immune system “remembers” the infectious agent and can prevent it from causing disease later, such as measles and diphtheria induce adaptive immune responses which generate a life-long immunity following an infection [Roitt 1996]. Therefore, the two important features of adaptive immune responses are highly specific for a particular pathogen and memory. The

specificity is consequently the key as well as the demand while developing an immunosensor.

Lymphocytes are an important type of leucocytes (white blood cells) for all adaptive immune responses, which have two main subclasses: T lymphocytes (or T cells) and B lymphocytes (or B cells). B cells deal with the extracellular pathogens and their products by releasing antibody, which is a protein molecule specifically recognizing and binding to a particular target molecule (antigen). The antigen may be a molecule on the surface of a pathogen, or a toxin which it products.

## 2.2 Antigen recognition

The original definition of the term antigen was: Any molecule that induced B cells to produce a specific antibody, i.e. *antibody generator*. Now it indicates any molecule that can be specifically recognized by the adaptive elements of the immune system, i.e. by either B or T cells or both. It should be noted that antibodies do not bind to the whole of an infectious agent. For each antibody molecule, only one of the molecules on the agent surface will be recognized and bound. Therefore, there are many several different antibodies for a given pathogen, each binding to a different antigen on the surface of the pathogen. The restricted part of an antigen bound by an antibody is called the “epitope”. A particular antigen can have several different epitopes or repeated epitopes [Roitt 1996]. As a result, antibody molecules are specific for the epitopes rather than the whole antigen molecule.

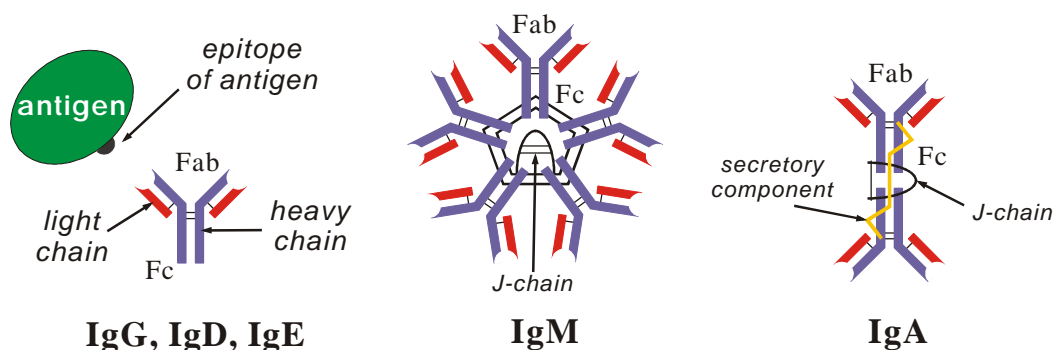


*Fig. 2-1 Subclasses of human antibodies. IgG, IgD and IgE molecules are similar in shape, only different in the length and amino sequences at the Fc fraction. IgM is found as a pentamer of 5 Y-shaped subunits with the Fc fraction bound together by J-chains (disulphide bonds). IgA is a dimer composed by 2 Y-shaped subunits by a J-chain and secretory component.*

## 2.3 Antibody structure

Antibody molecules are immunoglobulins (*Ig*), which are a group of glycoproteins and present in the serum and tissue fluids of all mammals. Five distinct classes of immunoglobulin molecule are recognized in most higher mammals, namely IgG, IgA, IgM, IgD and IgE. They are different in size, charge, amino acid composition and carbohydrate content [Roitt 1996]. The schematic illustrations of antibodies are shown in Fig.2-1.

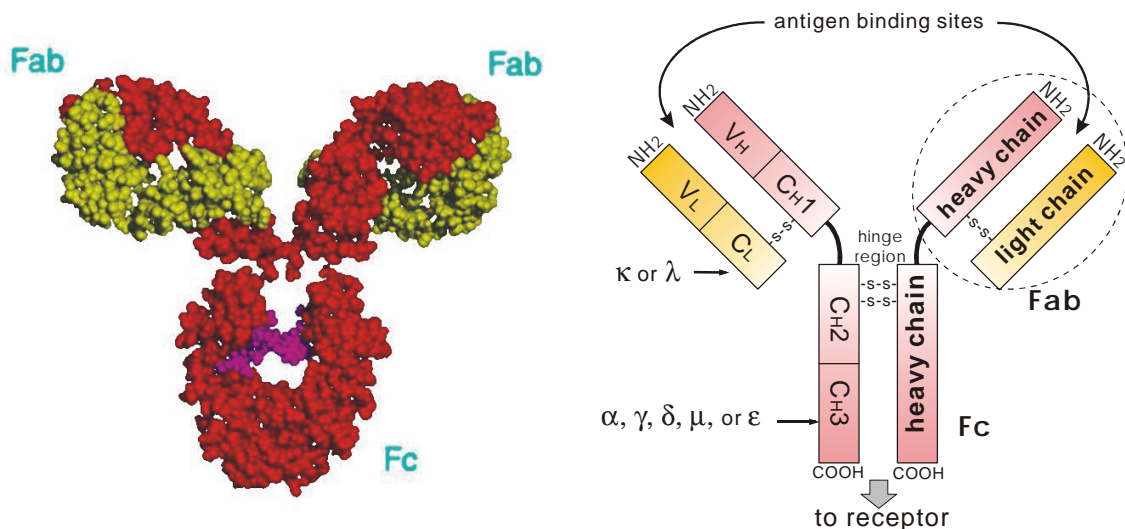
Since the type of antibodies used in this work was IgG, thus, only IgG's structure will be introduced here. The basic structural unit of most mammalian immunoglobulin molecules is a glycoprotein (molecular weight 150,000 Daltons) composed of four

Fig. 2-2 A computer simulated structure of an IgG molecule is shown (lower-left). The length of the IgG is about 10 nm. The red regions are heavy chains while the yellow parts are light chains. Two heavy chains are bound together by the disulphide bonds (pink regions).

The components of an IgG molecule is shown in the lower-right picture. Heavy chains and light chains are also bound together by disulphide bonds. The antigen-binding sites are at the Fab fractions. The Fc fraction can combine with the antibody-receptors on the surface of lymphocytes.

Table 2-1 List of subclasses of human antibodies.

Human antibodies			
	Light chain	Heavy chain	Subclasses
IgG	<i>k</i> or <i>l</i>	<i>g</i> <sub>1</sub>	IgG <sub>1</sub>
	<i>k</i> or <i>l</i>	<i>g</i> <sub>2</sub>	IgG <sub>2</sub>
	<i>k</i> or <i>l</i>	<i>g</i> <sub>3</sub>	IgG <sub>3</sub>
	<i>k</i> or <i>l</i>	<i>g</i> <sub>4</sub>	IgG <sub>4</sub>
IgA	<i>k</i> or <i>l</i>	<i>a</i> <sub>1</sub>	IgA <sub>1</sub>
	<i>k</i> or <i>l</i>	<i>a</i> <sub>2</sub>	IgA <sub>2</sub>
IgE	<i>k</i> or <i>l</i>	<i>e</i>	none
IgD	<i>k</i> or <i>l</i>	<i>d</i>	none
IgM	<i>k</i> or <i>l</i>	<i>m</i>	none



polypeptide chains - two light chains, and two heavy chains, which are connected by disulfide bonds, as shown in Fig.2-2. Each light chain has a molecular weight of about 25,000 Daltons and is composed of two domains, one variable domain ( $V_L$ ) and one constant domain ( $C_L$ ). There are two types of light chains, lambda ( $\lambda$ ) and kappa ( $\kappa$ ). In humans, 60% of the light chains are  $\kappa$ , and 40% are  $\lambda$ . A single antibody molecule contains either  $\kappa$ -light chains or  $\lambda$ -light chains, but never both.

Each heavy chain has a molecular weight of about 50,000 Daltons and consists of a constant and variable region. The heavy and light chains contain a number of homologous sections consisting of similar but not identical groups of amino acid sequences. These homologous units consist of about 110 amino acids and are called immunoglobulin domains. The heavy chain contains one variable domain ( $V_H$ ) and either three or four constant domains ( $C_{H1}$ ,  $C_{H2}$ ,  $C_{H3}$ , and  $C_{H4}$ , depending on the antibody class or isotype). The region between the  $C_{H1}$  and  $C_{H2}$  domains is called the hinge region and permits flexibility between the two  $F_{ab}$  arms of the Y-shaped antibody molecule, allowing them to open and close to accommodate binding to two antigenic determinants separated by a fixed distance.

The heavy chain also serves to determine the functional activity of the antibody molecule. The classes of immunoglobulin are distinguished by their heavy chains  $\gamma$ ,  $\alpha$ ,  $\mu$ ,  $\epsilon$  and  $\delta$ , respectively [Table 2-1]. The IgD, IgE and IgG antibody classes are each made up of a single structural unit, whereas IgA antibodies may contain either one or two units and IgM antibodies consist of five disulfide-linked structural units. IgG antibodies are further divided into four subclasses although the nomenclature differs slightly depending on the species producing the antibody.

## 2.4 Antibody specificity and affinity

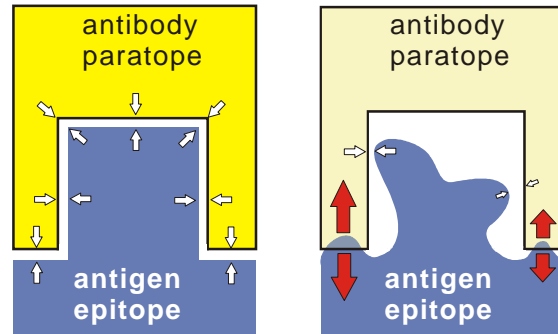
The binding of antigen to antibody involves the formation of multiple non-covalent bonds between the antigen and amino acids of the binding site, including hydrogen bonds, and electrostatic, Van der Waals and hydrophobic forces. Although they are weak by comparing with the covalent bonds individually, the sum of a great number of non-covalent forces are still considerable.

The conformations of target antigen and binding site are complementary. Before these forces become substantial, the interaction groups must be close enough. Fig.2-3 shows the specific and non-specific bindings between antigen epitope and antibody paratope, which is defined as the binding sites for antigens of an antibody. The shapes of

paratope and epitope must be complementary to form sufficient numbers of binding forces to resist the thermodynamic disruption of the bond. If the shapes overlap or can not fit, steric repulsive forces may be greater than the binding forces, and therefore the antigen will be separated from the antibody. This is called the high specificity of the antigen-antibody reaction since each antibody can recognize only one particular epitope on the surface of a given antigen. For example, antibodies against to a virus of hepatitis will not combine with unrelated viruses such as AIDS (*acquired immunodeficiency syndrome*) or SARS (*Severe Acute Respiratory Syndrome*).

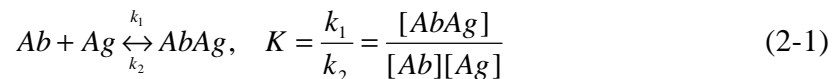
Antibody affinity indicates the strength of a single antigen-antibody bond. It is the sum of the attractive and repulsive forces. The non-covalent bonds are dissociable; hence the overall combination of an antibody and antigen must reversible.

Fig. 2-3 The specific binding (left) and non-specific binding (right) between antigen and antibody. The shapes of paratope and epitope should be fit to earn sufficient attractive forces against repulsive forces to accomplish specific binding.



## 2.5 Kinetics of antigen-antibody interactions

The antibody affinity is dependent on the equilibrium conditions of the antibody-antigen reaction. The law of mass action can be applied to the reaction for the determination of the equilibrium constant  $K$ , which is also termed as the antibody affinity constant:



where  $k_1$  [ $\text{mol}^{-1}\text{s}^{-1}$ ] and  $k_2$  [ $\text{s}^{-1}$ ] are the constants of the forward and reverse reaction rates, respectively. At equilibrium the ratio of the two constants gives the equilibrium constant. The symbol “[ ]” denotes the concentration of the objects. Since each antibody has two binding sites for antigens, antibodies are potentially multivalent in their reaction with antigen. It should be noted that antigen can also be monovalent (e.g. haptens) or multivalent (microorganisms), as shown in Fig.2-4. Table 2-2 indicates the influence of the effective valences of antibody and antigen to the equilibrium constant.

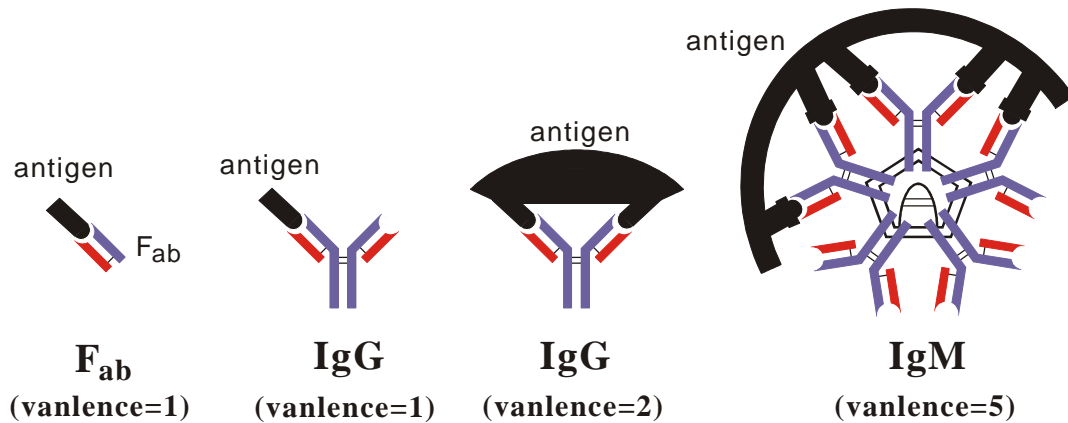


*Fig.2-4 The Multivalent bindings between antibodies and antigen results in a considerable increase in the equilibrium constants when comparing with to the monovalent binding. There may be a 1000-fold increase in the binding energy of IgG when both binding sites are utilized. The IgM can reach even a  $10^7$ -fold increase.*

*Table 2-2. Effective antibody valence and equilibrium constants. [Roitt 1996]*

antibody	F <sub>ab</sub>	IgG	IgG	IgM
effective antibody valence	1	1	2	Up to 10
antigen valence	1	1	n	n
equilibrium constant $K$ [ l/mol]	$10^4$	$10^4$	$10^7$	$10^{11}$
advantage of multivalence	-	-	$10^3$ - fold	$10^7$ - fold

Many methods have been developed to measure the equilibrium constant. The quantities of free and combined antigens are measured by physical methods, such as dialysis, gel filtration, centrifugation and selective precipitation, or fluorescent properties of the combined antigen or antibody.

From equation (2-1), the when half the binding sites of antibodies are occupied by antigens, then  $[Ab] = [AbAg]$ . The equilibrium constant becomes  $K = 1 / [Ag]$ , implying that a high-affinity antibody only requires a low antigen concentration to achieve binding of antigen to half its combining sites. On the contrary, a low-affinity antibody requires a much higher concentration of antigen to achieve this aim.

In this work, the high specificity of the antibody-antigen interactions will be demonstrated by the use of both SAW and electrochemical immunosensors in chapters 4 and 6. Besides, the equilibrium constants of immunoreactions were also measured. The results will be presented in chapter 7.

# Chapter 3

## Theory of Surface Acoustic Wave Sensors

The first type of immunosensors in this work is the surface acoustic wave (SAW) sensor. As implied by the name, this kind of sensor is based on the characteristics of acoustic wave propagating in a specially designed solid sensing structure, i.e., in our case, on the surface of a substrate. Any alteration in the properties of the substrate will influence the propagation of an acoustic wave. In this chapter, the theory of surface acoustic waves and their application to immunosensors will be introduced.

### 3.1 Elasticity in solids

#### 3.1.1 Stress and strain

Consider an infinite homogeneous as well as isotropic solid. If the solid is not subject to external forces from outside, then each volume element of solid components has a stable position described by a position vector  $\vec{x}_0$  with respect to the origin. If the solid is

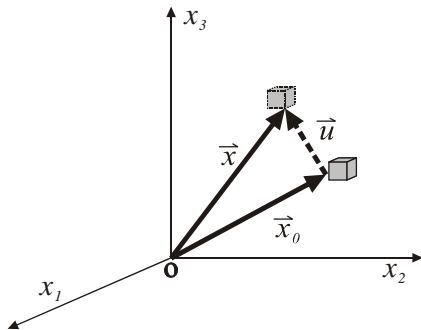


*Fig.3-1 Displacement of a volume element in a solid from its equilibrium position  $\vec{x}_0$  to final position  $\vec{x}$  can be described by the displacement vector  $\vec{u} = \vec{x} - \vec{x}_0$ .*

subject to a force, simple translation, rotation and deformation of the solid may happen. The displacement  $\vec{u}$  of an element from their original equilibrium position  $\vec{x}_0$  can be

expressed by  $\bar{\mathbf{u}} = \bar{\mathbf{x}} - \bar{\mathbf{x}}_0$ , where  $\bar{\mathbf{x}}$  is the new position of the element after the displacement [Fig.3-1]. This vector  $\bar{\mathbf{u}}$  includes the contributions due to translation, rotation and deformation. Since the translation and rotation are a macroscopic collective behavior of the whole solid, they are not responsible for the local deformation of a solid. In order to describe the deformation of a solid by forces, the gradient of the displacement is introduced:

$$(\nabla \bar{\mathbf{u}})_{ij} \equiv \frac{\partial u_i}{\partial x_j} \quad (3-1)$$

where  $i$  denotes the  $i^{\text{th}}$  component of the displacement, and  $j$  is a derivative with respect to the  $j^{\text{th}}$  spatial coordinate. The displacement caused by simple translation can be successfully excluded by the gradient of the displacement. The displacement due to rotation is also not of interest and has to be eliminated, either.

For the rotation of a rigid body, the displacement gradient  $(\nabla \bar{\mathbf{u}})_{ij}$  equals negative transpose of its own, i.e.  $(\nabla \bar{\mathbf{u}})_{ij} = -(\nabla \bar{\mathbf{u}})_{ji}$ ; thus, the deformation can be represented by sum of a displacement gradient and its transpose, which is called ‘‘Strain tensor’’ [Landau 1975]:

$$S_{ij} \equiv \frac{1}{2} [(\nabla \bar{\mathbf{u}})_{ij} + (\nabla \bar{\mathbf{u}})_{ji}] = \frac{1}{2} \left( \frac{\partial u_i}{\partial x_j} + \frac{\partial u_j}{\partial x_i} \right) \quad (3-2)$$

Strain is defined as the change in length per unit length in the solid at equilibrium. The diagonal strain terms  $S_{ii}$  represent axial strains, while the off-diagonal terms,  $S_{ij}$  with  $i \neq j$ , are shear strains. It is noted that the strain tensor in equation (3-2) is symmetric and has at most six independent components.

Strain is caused by the application of forces to a unit volume element  $dV$  of a solid. These forces which give rise to deformation and act on a unit volume element  $dV$  of a solid can be represented by

$$dF_i = f_i dV = \sum_j \frac{\partial T_{ij}}{\partial x_j} dV = \sum_j T_{ij} ds_j \quad (3-3)$$

where  $f_i$  is the force density of the  $i^{\text{th}}$  component,  $T_{ij}$  is the stress tensor,  $s_j$  is the surface of the solid normal to the  $j^{\text{th}}$  component of the force. The stress tensor denotes the state of stress at each point in a solid. Each element of the stress tensor  $T_{ij}$  represents the  $i^{\text{th}}$  component of force per area acting on the  $j^{\text{th}}$  face of an infinitesimal volume element. Stress in any direction on any plane interior to the solid can be determined by the stress tensor. In equation (3-3),  $\sum_j T_{ij} ds_j$  denotes the  $i^{\text{th}}$  component of the sum of forces acting on the surface element  $ds$ . Like the strain tensor, the stress tensor has a maximum of six independent components, too. Fig.3-2(a) shows the geometric relations between the elements of the stress tensor.

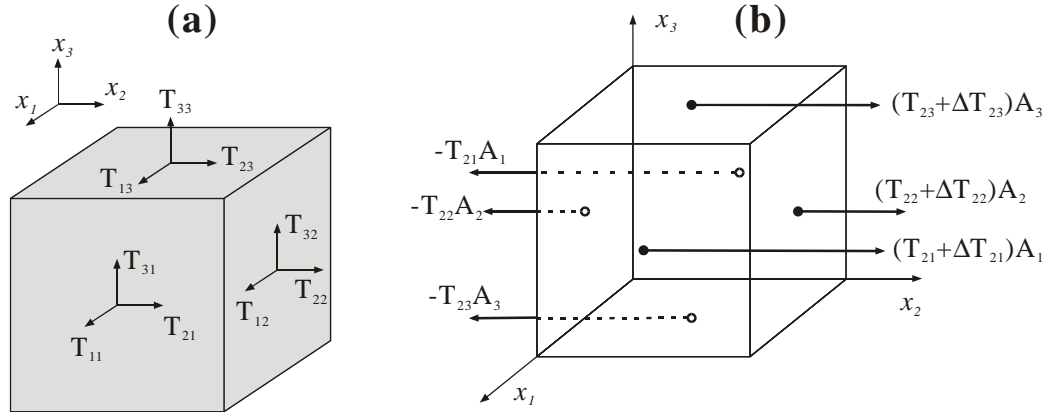


Fig.3-2 (a) Scheme of the components of a stress tensor  $T_{ij}$  in a unit volume element, and (b) Forces in the direction of the  $x_2$ -axis on each face are the sum of the corresponding stress tensor multiplied with the area of the face.  $\Delta T_{ij}$  means the change of the  $i^{\text{th}}$ -component of stress across the faces which are normal to  $x_j$ -axis.

### 3.1.2 Elastic constitutive relation

Fig.3-2(b) illustrates a deformation of a unit volume element along  $x_2$ -axis. It is assumed that the stress has merely changed an infinitesimal amount  $\Delta T_{ij}$  across the elemental length  $\Delta x_j$ . The total force that causes the deformation in the  $x_2$ -direction can be written as:

$$F_2 = [(T_{22} + \Delta T_{22})A_2 - T_{22}A_2] + [(T_{23} + \Delta T_{23})A_3 - T_{23}A_3] + [(T_{21} + \Delta T_{21})A_1 - T_{21}A_1] \quad (3-4)$$

$$= \Delta T_{22}A_2 + \Delta T_{23}A_3 + \Delta T_{21}A_1$$

The area of each face in the  $x_i$  direction is  $A_i = \sum_{j,k} d_{ijk} \Delta x_j \Delta x_k$  with  $i \neq j \neq k$ . From Newton's second law of motion, the total force in the  $x_2$ -direction can be written as

$$F_2 = \Delta T_{22}A_2 + \Delta T_{23}A_3 + \Delta T_{21}A_1$$

$$= \Delta T_{22} \Delta x_3 \Delta x_1 + \Delta T_{23} \Delta x_2 \Delta x_1 + \Delta T_{21} \Delta x_2 \Delta x_3 \quad (3-5)$$

$$= m \ddot{u}_2 = \mathbf{r} \Delta x_1 \Delta x_2 \Delta x_3 \frac{\partial^2 u_2}{\partial t^2}$$

where  $\mathbf{r}$  is the mass density of the solid,  $t$  is the time,  $m$  is the mass of the unit volume element, and  $\ddot{u}_2$  is the acceleration of the faces in the  $x_2$ -direction. Combining equation (3-3) and (3-5), and dividing by the volume of the element, a one-dimensional partial differential equation of motion:

$$\frac{\partial T_{2j}}{\partial x_2} = \mathbf{r} \frac{\partial^2 u_2}{\partial t^2} \quad (3-6)$$

Equation (3-6) can be generalized to the three-dimensional equation of motion which

associates the gradient of stress tensor and total force:

$$\sum_{j=1}^3 \frac{\partial T_{ij}}{\partial x_j} = \mathbf{r} \frac{\partial^2 u_i}{\partial t^2} \quad (3-7)$$

For small deformation, the stress tensor can be related to the strain tensor by Hooke's law. This linearity relation is known as the *constitutive relation* of non-piezoelectric solids [Auld 1990]:

$$T_{ij} = \sum_{k,l=1}^3 c_{ijkl} S_{kl} \quad (3-8)$$

where  $c_{ijkl}$  are called the *elastic stiffness constants* in analogy to the spring constant of Hooke's law. The elastic stiffness constants represent the elastic characteristic of a material.

### 3.1.3 Simplification of the elastic stiffness constant

There are totally 81 ( $3^4$ ) elements in the elastic stiffness tensor  $c_{ijkl}$ . The stress tensor elements  $T_{ij}$  are symmetric, i.e.  $T_{ij} = T_{ji}$ , which results in

$$c_{ijkl} S_{kl} = c_{jikl} S_{kl}, \text{ therefore } c_{ijkl} = c_{jikl} \quad (3-9)$$

Also, the strain tensor elements  $S_{kl}$  are symmetric, i.e.  $S_{kl} = S_{lk}$ , resulting in

$$c_{ijkl} S_{kl} = c_{ijlk} S_{lk} \text{ and consequently } c_{ijkl} = c_{ijlk} \quad (3-10)$$

Furthermore, in order to minimize the elastic energy of a solid, the elastic stiffness constants are invariant under exchange of the rear index pair with the front index pair:

$$c_{ijkl} = c_{klij} \quad (3-11)$$

Table 3-1 Reduced index notations

Index $ij \leftrightarrow$ Index $I$
11 $\leftrightarrow$ 1
22 $\leftrightarrow$ 2
33 $\leftrightarrow$ 3
23 or 32 $\leftrightarrow$ 4
13 or 31 $\leftrightarrow$ 5
12 or 21 $\leftrightarrow$ 6

Thus, these constraints on the elastic stiffness constant ensure that four subscripts in the equation (3-8) can be reduced to two by using abbreviated subscript notations shown in Table 3-1. The double index  $ij$  is replaced by a single index  $I$ , and the number of elements in the elastic stiffness tensor is reduced to 36. Equation (3-8) is also reduced and hence given by

$$T_I = \sum_{J=1}^6 c_{IJ} S_J \quad (3-12)$$

and is termed “reduced elastic constitutive relation”. The reduced index  $I$  and  $J$  are from 1 to 6. According to equation (3-11), the index  $I$  and  $J$  of elastic stiffness constants can also be exchanged, i.e.  $c_{IJ}$  is symmetric and can be simplified in advance to only 21 independent elements, in which there are 6 diagonal terms and 15 off-diagonal entries.

### 3.1.4 Isotropic solid

For an isotropic solid, the physical constants are unaffected by the choice of orthonormal coordinate axes. Especially, the elastic stiffness constant  $c_{ijkl}$  must also be invariant for any change of axes. But, only the scalar or unit tensor  $\mathbf{d}_{ij}$  satisfies the invariance of the orthogonal transformations. Accordingly, the elements of  $c_{ijkl}$  can be described by components of the unit tensor. Only three distinct combinations include the four index  $ijkl$  since the unit tensor is symmetric ( $\mathbf{d}_{ij} = \mathbf{d}_{ji}$ ):  $\mathbf{d}_{ij}\mathbf{d}_{kl}$ ,  $\mathbf{d}_{ik}\mathbf{d}_{jl}$ ,  $\mathbf{d}_{il}\mathbf{d}_{jk}$ . The elastic stiffness constant can be written as:

$$c_{ijkl} = \mathbf{l} \mathbf{d}_{ij} \mathbf{d}_{kl} + \mathbf{m}_1 \mathbf{d}_{ik} \mathbf{d}_{jl} + \mathbf{m}_2 \mathbf{d}_{il} \mathbf{d}_{jk} \quad (3-13)$$

where  $\mathbf{l}$ ,  $\mathbf{m}_1$  and  $\mathbf{m}_2$  are constants. Besides, because of the symmetry of the elastic stiffness tensor,  $c_{ijkl} = c_{jikl}$ ,  $\mathbf{m}_1$  has to be equal to  $\mathbf{m}_2$ , i.e.  $\mathbf{m}_1 = \mathbf{m}_2 = \mathbf{m}$ . Thus, equation (3-13) becomes

$$c_{ijkl} = \mathbf{l} \mathbf{d}_{ij} \mathbf{d}_{kl} + \mathbf{m} (\mathbf{d}_{ik} \mathbf{d}_{jl} + \mathbf{d}_{il} \mathbf{d}_{jk}) \quad (3-14)$$

The  $\mathbf{l}$  and  $\mathbf{m}$  are the Lamé constants, which also specify the properties of an isotropic solid are specified. Applying abbreviated subscript notations from Table 3-1, we get

$$\begin{aligned} c_{11} &= c_{22} = c_{33} = \mathbf{l} + 2\mathbf{m} \\ c_{12} &= c_{23} = c_{13} = \mathbf{l} \\ c_{44} &= c_{55} = c_{66} = \mathbf{m} = (c_{11} - c_{12})/2 \end{aligned} \quad (3-15)$$

and the rest of elements are zero since they have odd number of distinct indices by equation (3-14). Then the tensor  $c_{IJ}$  of an isotropic material is given by

$$c_{IJ} = \begin{pmatrix} c_{11} & c_{12} & c_{12} & 0 & 0 & 0 \\ c_{12} & c_{11} & c_{12} & 0 & 0 & 0 \\ c_{12} & c_{12} & c_{11} & 0 & 0 & 0 \\ 0 & 0 & 0 & c_{66} & 0 & 0 \\ 0 & 0 & 0 & 0 & c_{66} & 0 \\ 0 & 0 & 0 & 0 & 0 & c_{66} \end{pmatrix} \quad (3-16)$$

Hooke's law in an isotropic solid is also simplified. Equation (3-8) can be expressed in terms of Lamé constants in equation (3-15) as followed

$$T_{ij} = I (S_{11} + S_{22} + S_{33})d_{ij} + 2md_{ij} \quad (3-17)$$

### 3.1.5 Piezoelectric materials

The above discussion has focused on the elasticity of an isotropic solid, but materials suitable for generating surface acoustic waves for the application in biosensors are just piezoelectric crystals. Piezoelectricity arises from the coupling between strain and electrical polarization in some crystals. For piezoelectricity to occur, the crystal must lack a center of symmetry [Royer 2000]. Under this condition, the application of strain due to mechanical forces changes the distribution of charge on the atoms and bonds such that a macroscopic and electrical polarization of the crystal takes place. This is the so called *direct piezoelectric effect*. On the other hand, the crystal will be also mechanically deformed by an applied electric field (*inverse piezoelectric effect*).

Since strain and electric field are coupled together for a piezoelectric material, the elastic constitutive relation in equation (3-12) has to be modified as [Royer 2000]

$$T_{ij} = \sum_{kl=1}^6 c_{ij,kl}^E S_{kl} - \sum_{k=1}^3 e_{k,ij} E_k \quad (3-18)$$

with

$$c_{ij,kl}^E = \left( \frac{\partial T_{ij}}{\partial S_{kl}} \right)_E \quad \text{and} \quad e_{k,ij} = - \left( \frac{\partial T_{ij}}{\partial E_k} \right)_E \quad (3-19)$$

where  $c_{ij,kl}^E$  indicates that the elastic stiffness constants in the generalized Hooke's law relate stress and strain at constant electric field,  $e_{k,ij}$  is the piezoelectric tensor with units of (charge)/(length)<sup>2</sup>,  $E_k$  are components of the electric field. Since the stress tensor  $T_{ij}$  is symmetric, the piezoelectric tensor  $e_{k,ij}$  is symmetric, too. The first term in equation (3-18) is a purely elastic effect, while the second term is the piezoelectric effect, which relates the electric field with the stress tensor linearly.

Moreover, a modification of the electrical displacement for piezoelectric materials is also necessary:

$$D_i = \sum_{j=1}^3 \mathbf{e}_{ij}^S E_j + \sum_{jk=1}^6 e_{i,jk} S_{jk} \quad (3-20)$$

where  $\mathbf{e}_{ij}^S$  is the dielectric constant measured under constant mechanical stress, and again, the piezoelectric constants  $e_{i,jk}$  relate changes of the electric displacement components  $D_i$  to the strain  $S_{jk}$  in the solid with the electric field held constant:

$$e_{i,jk} = \left( \frac{\partial D_i}{\partial S_{jk}} \right)_E \quad (3-21)$$

Equations (3-18) and (3-20) are *piezoelectric constitutive relations*, which describe completely the interplay of stress, strain, and electric field in a piezoelectric solid. From equation (3-18), the strain in a piezoelectric material is composed of the mechanical stress term and from the term of the applied electric field. In equation (3-20), the electric displacement relates the applied electric field and the mechanical strain, implying that even if the applied electric field vanishes, any strain due to the mechanical stress will still result in an external field ( $D$ ) in a piezoelectric material.

In this section, only the static characteristics of elasticity, such as the deformation, stress and strain in a solid, have been generally discussed. In the next section, the dynamics in a solid, for example, the wave propagation and the wave equation of motion will be discussed.

## 3.2 Wave equations

### 3.2.1 Wave equation for non-piezoelectric solid

To understand the dynamic properties of acoustic waves in solids is essential, since their behaviors are closely related to the practicability of utilizing acoustic waves for sensor applications.

Acoustic waves propagating in elastic solids can be described by a wave equation. Starting from the equation (3-2), the strain tensor  $S_{kl}$  can be written as

$$S_{kl} = \frac{\partial u_k}{\partial x_l} \quad (3-22)$$

since the strain tensor is symmetric ( $S_{kl} = S_{lk}$ ). Then the wave equation for a non-piezoelectric solid can be easily derived from the equation of motion and the elastic constitutive relation. Putting equation (3-22) into equation (3-8) and differentiating with respect to  $x_j$  gives

$$\sum_{j=1}^3 \frac{\partial T_{ij}}{\partial x_j} = \sum_{j,k,l=1}^3 c_{ijkl} \frac{\partial^2 u_k}{\partial x_j \partial x_l} \quad (3-23)$$

Combining equation (3-23) and (3-7), we get the *wave equation for non-piezoelectric solids*:

$$\mathbf{r} \frac{\partial^2 u_i}{\partial t^2} = \sum_{j,k,l=1}^3 c_{ijkl} \frac{\partial^2 u_k}{\partial x_j \partial x_l} \quad (3-24)$$

where  $i = 1, 2, 3$ , indicates three solutions of the wave equations in each direction of particle displacement  $u_1, u_2, u_3$ , respectively, with summation over the indices  $j, k, l$ . Thus, there are three kinds of polarization associated with the different particle displacements, i.e. three possible wave types exist in a solid. One of them is a quasi-compressional (or quasi-longitudinal) wave with the polarization closest to the direction of propagation. The other two waves are quasi-shear (or quasi-transverse) waves whose polarizations is perpendicular to the direction of propagation, but still orthogonal to each other. The quasi-transverse waves usually travel slower than the quasi-longitudinal wave, and only in particular propagation directions are the waves purely longitudinal and transverse [Royer 2000].

### 3.2.2 Wave equation for piezoelectric solids

From the piezoelectric constitutive relations [equation (3-18) and (3-20)], we know that the mechanical elastic effect and the electromagnetic effect are coupled for a piezoelectric material. The velocity of elastic waves at which a stress or strain propagates is about  $10^4$  to  $10^5$  times less than that of an electromagnetic wave. Therefore, the magnetic field associated with mechanical vibrations is negligibly small since it arises from an electric field traveling with a velocity much less than the velocity of the electromagnetic waves. This implies that the electromagnetic field associated with an elastic field is quasi-static, so that the Maxwell equations reduce to

$$\nabla \times \bar{\mathbf{E}} = -\frac{\partial \bar{\mathbf{B}}}{\partial t} \cong 0 \quad \text{and} \quad \bar{\mathbf{E}}(\bar{\mathbf{x}}, t) = -\nabla \Phi(\bar{\mathbf{x}}, t) \quad (3-25)$$

The electric field  $\mathbf{E}$  associated with the piezoelectric effect can be expressed by a gradient of a scalar potential  $\Phi$  like in the electrostatic case. Under this quasi-static approximation, substituting equation (3-2) and (3-25) into (3-18), the stress tensor becomes

$$T_{ij} = \sum_{kl=1}^6 c_{ij,kl}^E \frac{\partial u_l}{\partial x_k} + \sum_{k=1}^3 e_{k,ij} \frac{\partial \Phi}{\partial x_k} \quad (3-26)$$

and substituting the above equation above into Newton's second law of motion in equation (3-7) gives

$$\mathbf{r} \frac{\partial^2 u_i}{\partial t^2} = \sum_{kl=1}^6 c_{ij,kl}^E \frac{\partial^2 u_l}{\partial x_j \partial x_k} + \sum_{k=1}^3 e_{k,ij} \frac{\partial^2 \Phi}{\partial x_j \partial x_k} \quad (3-27)$$

Furthermore, the electric displacement in equation (3-20) becomes

$$D_i = \sum_{j=1}^3 \mathbf{e}_{ij}^S E_j + \sum_{jk=1}^6 e_{i,jk} S_{jk} = \sum_{j=1}^3 \mathbf{e}_{ij}^S \frac{\partial \Phi}{\partial x_j} - \sum_{jk=1}^6 e_{i,jk} \frac{\partial u_j}{\partial x_k} \quad (3-28)$$

and for insulating solids,  $D_i$  must satisfy Poisson's equation  $\partial D_i / \partial x_i = 0$ , hence

$$\sum_{j=1}^3 \mathbf{e}_{ij}^S \frac{\partial^2 \Phi}{\partial x_i \partial x_j} = \sum_{jk=1}^6 e_{i,jk} \frac{\partial^2 u_j}{\partial x_k \partial x_i} \quad (3-29)$$

So, equation (3-29) and (3-27) are the wave equations for a piezoelectric solid. For non-piezoelectric solids, for which  $e_{ijk}$  equals 0, then the wave equations return to equation (3-24).

## 3.3 Solutions of the wave equations

### 3.3.1 Bulk acoustic waves in isotropic solids

For isotropic solids, the elements of the elastic stiffness tensor can be expressed by only two independent parameters [ $\mathbf{l}$  and  $\mathbf{m}$  in equation (3-15)]. Now, the equation of motion [equation (3-7)] for an isotropic solid can be rearranged by  $\mathbf{l}$  and  $\mathbf{m}$ . From equation (3-15) and (3-17), the stress tensor becomes

$$T_{ij} = (c_{11} - 2c_{44})S \mathbf{d}_{ij} - 2c_{44} S_{ij} = (c_{11} - 2c_{44})S \mathbf{d}_{ij} + c_{44} \left( \frac{\partial u_i}{\partial x_j} + \frac{\partial u_j}{\partial x_i} \right) \quad (3-30)$$

where  $S$  is the dilatation defined by  $S = S_{ii} = \nabla \cdot \mathbf{u} = \partial u_i / \partial x_i$ . Substituting the equation above into the equation of motion, we get

$$\mathbf{r} \frac{\partial^2 u_i}{\partial t^2} = \frac{\partial}{\partial x_i} \left[ (c_{11} - 2c_{44}) \frac{\partial u_i}{\partial x_i} \right] + c_{44} \frac{\partial^2 u_i}{\partial x_j^2} + c_{44} \frac{\partial}{\partial x_i} \left( \frac{\partial u_j}{\partial x_j} \right) \quad (3-31)$$

In the vector form, the above equation becomes

$$\mathbf{r} \frac{\partial^2 \bar{\mathbf{u}}}{\partial t^2} = (c_{11} - c_{44}) \nabla (\nabla \cdot \bar{\mathbf{u}}) + c_{44} \nabla^2 \bar{\mathbf{u}} = (\mathbf{l} + \mathbf{m}) \nabla (\nabla \cdot \bar{\mathbf{u}}) + \mathbf{m} \nabla^2 \bar{\mathbf{u}} \quad (3-32)$$

In last section we have concluded that in an infinitely large solid without boundary

conditions, three plane waves with orthogonal polarization can propagate in the same direction with different velocity. These plane waves propagating in the  $x_1$  direction are

$$u_i(x_1, t) = A_i e^{i(k_i x_1 - \omega_i t)}, \quad i = 1, 2, 3 \quad (3-33)$$

where  $A_i$  are amplitudes,  $\omega_i = \mathbf{u}_i k_i$  the angular frequencies and  $\mathbf{u}_i$  the velocities of the plane wave. Substituting equation (3-33) into equation (3-32) gives three wave equations:

$$\frac{\partial^2 u_{x_1}}{\partial x_1^2} - \frac{1}{\mathbf{u}_1^2} \frac{\partial^2 u_{x_1}}{\partial t^2} = 0, \quad \frac{\partial^2 u_{x_2}}{\partial x_1^2} - \frac{1}{\mathbf{u}_t^2} \frac{\partial^2 u_{x_2}}{\partial t^2} = 0, \quad \frac{\partial^2 u_{x_3}}{\partial x_1^2} - \frac{1}{\mathbf{u}_t^2} \frac{\partial^2 u_{x_3}}{\partial t^2} = 0 \quad (3-34a)$$

with the phase velocities

$$\mathbf{u}_l = \sqrt{\frac{l + 2m}{\mathbf{r}}} = \sqrt{\frac{c_{11}}{\mathbf{r}}}, \quad \text{and} \quad \mathbf{u}_t = \sqrt{\frac{(c_{11} - c_{12})}{2\mathbf{r}}} = \sqrt{\frac{c_{44}}{\mathbf{r}}} \quad (3-34b)$$

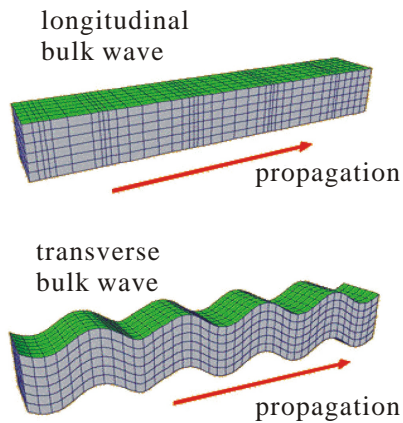


Fig.3-3 Scheme of transverse and longitudinal bulk waves propagating in a solid.

where  $\mathbf{u}_l$  and  $\mathbf{u}_t$  are velocities of the quasi-longitudinal and quasi-transverse plane waves, respectively. Fig.3-3 shows the differences between these two wave types. Since  $c_{12}$  is positive, the transverse waves will always propagate slower than the longitudinal wave with the relation

$$\mathbf{u}_t < \frac{\mathbf{u}_l}{\sqrt{2}}. \quad (3-35)$$

### 3.3.2 Surface acoustic waves in isotropic solids

Surface acoustic waves, as implied by the name, are acoustic waves which spread out and propagate on the surface of a substrate. As a result, in order to characterize the behavior of surface wave precisely, the material can not be treated as an infinite bulk size, but with a limited dimension with special mechanical and electrical boundary conditions.

In Fig.3-4, the wave propagates in the  $x_1$ -direction on the surface of a half-infinite substrate, which extends infinitely in the  $x_1$ - and  $x_2$ -directions as well as in the negative  $x_3$ -direction. Therefore, the plane with  $x_3 = 0$  is the boundary of the substrate and the interface between vacuum and solid. The wave vector and the normal vector of the boundary compose a cross section, called sagittal plane, as shown in Fig.3-4.

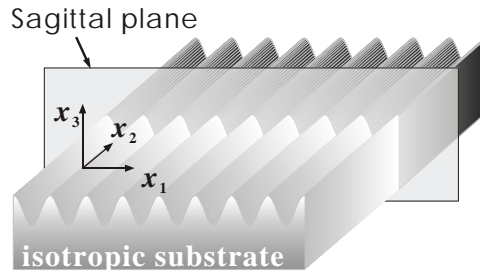


Fig.3-4 A half-space material. The solid is infinite in  $x_1$  and  $x_2$  and negative  $x_3$  directions. The wave travels on the surface with  $x_3=0$  and in  $x_1$ -direction.

At the plane  $x_3 = 0$ , the mechanical boundary condition is that the stress must be zero since the particles at the plane do not experience restoring force:

$$T_{13} = T_{23} = T_{33} = 0 \quad (3-36)$$

For a piezoelectric solid, the electrical boundary conditions are that the continuity of the potential  $\Phi$  at the interface must be satisfied for a charge free interface

$$\Phi_{Solid}|_{x_3=0} = \Phi_{Vacuum}|_{x_3=0} \quad \text{and} \quad \nabla^2 \Phi_{Vacuum}|_{x_3>0} = 0 \quad (3-37)$$

The vertical component (in the  $x_3$ -direction) of the electric displacement should be continuous at the boundary:

$$D_{3-Solid}|_{x_3=0} = D_{3-Vacuum}|_{x_3=0} \quad (3-38)$$

If the surface is electrically shorted, the electric potential on the total surface must be zero. Finding the solutions for the wave equations in anisotropic, piezoelectric solids is usually complicated. There are no analytical solutions for most crystals; therefore numerical methods must be used for the solutions. Thus, we focus on the analytical solution for isotropic materials first, and then it will be modified to fit the characteristics of anisotropic solids.

In order to solve the equation of motion for isotropic solids in equation (3-24) concerning the *surface* acoustic wave, an additional boundary condition is required. The amplitude of the wave should decrease with the depth of the substrate, and vanishes at  $x_3 = -\infty$  to fit the definition of the “surface” acoustic wave i.e.

$$\bar{\mathbf{u}}(\bar{\mathbf{x}}, t)|_{x_3=-\infty} = 0 \quad (3-39)$$

Thus, the special solution for the wave equation (3-24) is a linear combination of partial waves traveling in the  $x_j$ -direction

$$u_j = \mathbf{a}_j e^{ikbx_3} e^{ik(x_1 - \mathbf{u}t)}, \quad j = 1, 2, 3 \quad (3-40)$$

where  $\mathbf{a}_j$  is the amplitude,  $k$  is the wave vector,  $\mathbf{u}$  is the velocity, and  $b$  is the decay constant, which must be a negative, purely imaginary number, so that the boundary condition [equation (3-39)] can be satisfied. Substituting equation (3-40) into equation (3-24) gives

$$\Gamma_{ij} \mathbf{a}_j = \mathbf{r} \mathbf{u}^2 \mathbf{a}_j \quad (3-41)$$

where

$$\Gamma_{ij} = \begin{pmatrix} c_{11} + c_{44} b^2 & 0 & (c_{11} - c_{44})b \\ 0 & c_{44}(1 + b^2) & 0 \\ (c_{11} - c_{44})b & 0 & c_{44} + c_{11} b^2 \end{pmatrix}$$

It is obvious that the equation of motion now becomes an eigenvalue equation of matrix  $\Gamma$  with eigenvalue  $\mathbf{b}$  and eigenvector  $\mathbf{a}_j$ . By solving the characteristic polynomial of the matrix  $\Gamma$ , the eigenvalues of the above equation can be found, i.e. by solving

$$\det(\Gamma_{ij} - \mathbf{b} \mathbf{d}_{ij}) = 0 \quad (3-42)$$

the eigenvalues will be obtained:

$$\mathbf{b}_{(1)} = c_{11} + c_{11} b^2, \quad \text{and} \quad \mathbf{b}_{(2)} = \mathbf{b}_{(3)} = c_{44} + c_{44} b^2 \quad (3-43)$$

And the corresponding eigenvectors are:

$$\mathbf{a}^{(1)} = \begin{pmatrix} 1 \\ 0 \\ b \end{pmatrix}, \quad \mathbf{a}^{(2)} = \begin{pmatrix} 0 \\ 1 \\ 0 \end{pmatrix}, \quad \mathbf{a}^{(3)} = \begin{pmatrix} -b \\ 0 \\ 1 \end{pmatrix} \quad (3-44)$$

The eigenvalues derived from equation (3-42) and (3-41) should be identical,  $\mathbf{b} = \rho v^2$ , therefore, the decay constants for each eigenvalue can be solved. For  $\mathbf{b}^{(1)}$ :

$$\begin{aligned} \mathbf{b}_{(1)} = c_{11} + c_{11} b^2 = \mathbf{r} \mathbf{u}^2 &\Rightarrow b_{(1)} = \pm \sqrt{\frac{\mathbf{r} \mathbf{u}^2}{c_{11}} - 1} = \pm \sqrt{\frac{\mathbf{u}^2}{\mathbf{u}_t^2} - 1} \\ &\Rightarrow \text{choose } b_{(1)} = -i \sqrt{1 - \frac{\mathbf{u}^2}{\mathbf{u}_t^2}} \end{aligned} \quad (3-45)$$

The reason why only the negative term was chosen in the above equation is that the decay constant must satisfy the boundary condition, by which the amplitude decreases with depth in the negative  $x_3$ -direction.

For the other two eigenvalues,  $\mathbf{b}_{(2)}$  and  $\mathbf{b}_{(3)}$ , using the same method we get

$$\begin{aligned} \mathbf{b}_{(2)} = \mathbf{b}_{(3)} = c_{44} + c_{44} b^2 = \mathbf{r} \mathbf{u}^2 &\Rightarrow b_{(2)} = b_{(3)} = \pm \sqrt{\frac{\mathbf{r} \mathbf{u}^2}{c_{11}} - 1} = \pm \sqrt{\frac{\mathbf{u}^2}{\mathbf{u}_t^2} - 1} \\ &\Rightarrow \text{choose } b_{(2)} = b_{(3)} = -i \sqrt{1 - \frac{\mathbf{u}^2}{\mathbf{u}_t^2}} \end{aligned} \quad (3-46)$$

Now, with these decay constants, eigenvalues and eigenvectors, for every partial wave can be deduced. The final step to solve the surface acoustic wave equation is to take into account the boundary condition in equation (3-36) into. This can be done by considering that the general solution is the linear combination of all partial waves [equation (3-40)]

$$\mathbf{u}_j = \sum_m C_m \mathbf{u}_j^{(m)} = \left( \sum_m C_m \mathbf{a}_j^{(m)} e^{ikb_{(m)}x_3} \right) e^{ik(x_1 - \mathbf{u}_t t)} \quad (3-47)$$

Inserting this general solution into equation (3-36) gives

$$B_{im} C_m = 0 \quad (3-48a)$$

with

$$B_{im} = \begin{pmatrix} 2c_{44}b_{(1)} & 0 & c_{44} - c_{44}b_{(3)}^2 \\ 0 & c_{44}b_{(2)} & 0 \\ c_{11} - 2c_{44} + c_{11}b_{(1)}^2 & 0 & 2c_{44}b_{(3)} \end{pmatrix} \quad (3-48b)$$

The characteristic polynomial for the above matrix is

$$c_{44}b_{(2)} \left[ 4c_{44}^2b_{(1)}b_{(3)} - c_{44}(1 - b_{(3)}^2)(c_{11} - 2c_{44} + c_{11}b_{(1)}^2) \right] = 0 \quad (3-49)$$

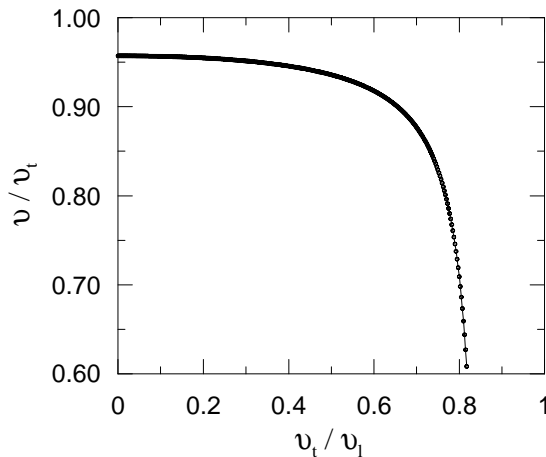
One obvious solution is that  $b_{(2)}$  in this polynomial is zero, this decay constant belongs to a bulk shear wave, which propagates in the  $x_2$ -direction and its displacement is parallel to the surface of the substrate (the  $x_3 = 0$  plane) and independent of the  $x_3$  in the negative  $x_3$ -direction. The other solution of the characteristic polynomial is when the terms in bracket are zero

$$-4b_{(1)}b_{(3)} = (1 - b_{(3)}^2)^2 \Rightarrow 4\sqrt{1 - \frac{\mathbf{u}^2}{\mathbf{u}_l^2}}\sqrt{1 - \frac{\mathbf{u}^2}{\mathbf{u}_t^2}} = \left( 2 - \frac{\mathbf{u}^2}{\mathbf{u}_t^2} \right)^2 \quad (3-50)$$

which implies that the phase velocity of the surface wave in an isotropic solid depends only on the longitudinal and transverse velocity. The ratio of the phase velocity and transverse velocity is approximately [Viktorov 1967]

$$\frac{\mathbf{u}}{\mathbf{u}_t} \approx \frac{0.718 - (\mathbf{u}_l/\mathbf{u}_t)^2}{0.75 - (\mathbf{u}_l/\mathbf{u}_t)^2} \quad (3-51)$$

Since the ratio of the transverse and longitudinal velocity from equation (3-35) is always smaller than  $\sqrt{1/2}$ , the ratio above will be always smaller than one, implying that the



velocity of a surface acoustic wave is always smaller than that of the transverse bulk wave in an isotropic solid forever [Fig.3-5].

*Fig.3-5 Ratio of surface wave velocity and velocity of transverse bulk wave versus  $\mathbf{u}_t / \mathbf{u}_l$  of the bulk wave. It is obvious that the fastest surface wave velocity is lower than the smallest velocity of a bulk wave in a solid.*

Fig.3-5 and equation (3-40) give the evidence that the decay constants in equations (3-45) and (3-46) are purely negative imaginary, resulting in an exponential decrease in the wave amplitudes with the depth of a solid; Using relation (3-50) to solve equation (3-48) gives that  $C_2 = 0$  and  $C_3 = -C_1 [2b_{(1)} / (1 - b_{(3)}^2)]$ . Since  $C_2 = 0$ , the component of amplitude in the  $x_2$ -direction is zero, i.e. the motion of the particles is limited to the sagittal plane shown in Fig.3-3. Therefore, this kind of wave is localized near the surface of the substrate, namely “*surface acoustic wave*” or “*Rayleigh wave*”, which was firstly described by Lord Rayleigh in 1885. Since the velocity of the Rayleigh wave is always much smaller than that of the bulk wave in solids, they can not couple with each other. Therefore, for surface acoustic waves, energy dissipation into the bulk will not occur. The amplitude for each component can be calculated as

$$\begin{aligned} u_1 &= \frac{2C_1}{1 - b_{(3)}^2} \left( \frac{1 - b_{(3)}^2}{2} e^{ikb_{(1)}x_3} + b_{(1)}b_{(3)} e^{ikb_{(3)}x_3} \right) e^{ik(x_1 - ut)} \\ u_2 &= 0 \\ u_3 &= \frac{2C_1 b_{(1)}}{1 - b_{(3)}^2} \left( \frac{1 - b_{(3)}^2}{2} e^{ikb_{(1)}x_3} - e^{ikb_{(3)}x_3} \right) e^{ik(x_1 - ut)} \end{aligned} \quad (3-52)$$

The components  $u_1$  and  $u_3$  are non-zero, indicating that there are two partial waves of surface wave traveling on the surface of the substrate: A longitudinal ( $u_1$ ) and a transverse ( $u_3$ ) one. The trajectory of the movement of a volume element on the surface is an ellipse on the sagittal plane ( $x_1 x_3$ -plane) shown in Fig.3-4.

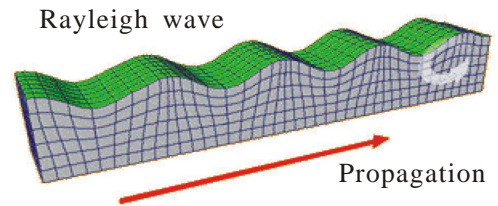
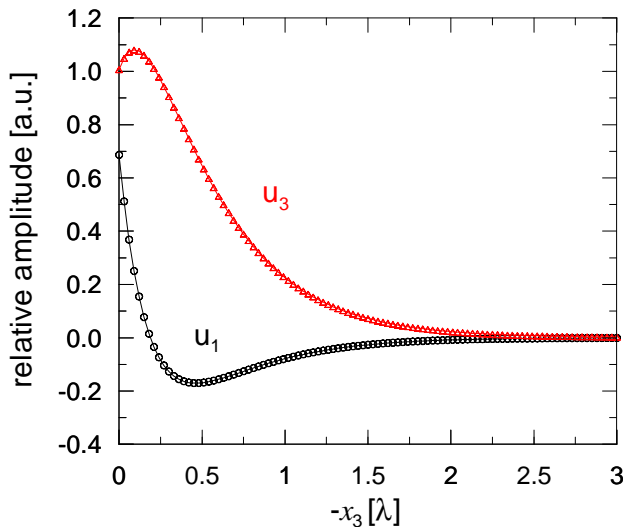


Fig.3-6 Scheme of motion of volume elements for a “Rayleigh wave” in a solid (above).

The transverse component ( $u_3$ ) and longitudinal component ( $u_1$ ) of the displacement versus penetration depth in a solid (Left).

In Fig.3-6, the motions of the volume elements and the amplitudes of longitudinal and transverse components versus depth (normalized with respect to the wave length  $\lambda$ ) in an isotropic solid are shown. Obviously, the longitudinal component  $u_1$  is about 1.75 times

smaller than the transverse component  $u_3$  at the surface ( $x_3 = 0$ ). Both components decrease with depth in the solid, the longitudinal component decays more quickly than the transverse component. At a depth of about  $0.2 \lambda$ , the longitudinal component passes zero, and only the transverse component exists. The direction of the circling movement of a volume element will change when  $x_3$  is less than  $-0.2 \lambda$ , i.e. from clockwise to counterclockwise. At a depth of  $3 \lambda$ , the longitudinal amplitude as well as the transverse amplitude have nearly vanished.

The relation between amplitude components and the power which a Rayleigh wave delivers can be written as [Fasold 1984]

$$\begin{aligned} \frac{P}{\omega u_1^2} &= \frac{2}{(1-b_{(2)}^2)^2} (c_{11}A - c_{12}B) \\ \frac{P}{\omega u_3^2} &= \frac{(1+b_{(2)}^2)^2}{2b_{(1)}^2(1-b_{(2)}^2)^2} (c_{11}A - c_{12}B) \end{aligned} \quad (3-53)$$

where  $P$  is the power per beam width,  $\omega$  is the frequency of the Rayleigh wave, and  $A$  and  $B$  are functions of  $b_{(m)}$ . Taking cadmium sulfide as example, at 50 MHz and a power density of 1 mW / mm, the longitudinal amplitude is  $u_1 = 0.2$  nm, and the transverse amplitude  $u_3 = 0.33$  nm. In this case, both components are by a factor of  $10^5$  smaller than the wave length ( $\lambda = \omega / f = 34.6 \mu\text{m}$ ).

### 3.3.3 Acoustic waves in piezoelectric solids

Consider a  $x_3$ -polarized shear bulk wave propagating in,  $x_1$ -direction in a piezoelectric crystal, according to the wave equations (3-27) and (3-29) for piezoelectric material, the wave equations can be rewritten as

$$\mathbf{r} \frac{\partial^2 u_3}{\partial t^2} = c_{55} \frac{\partial^2 u_3}{\partial x_1^2} + e_{x_1,5} \frac{\partial^2 \Phi}{\partial x_1^2} \quad \text{and} \quad \mathbf{e}_{11} \frac{\partial^2 \Phi}{\partial x_1^2} = e_{x_1,5} \frac{\partial^2 u_3}{\partial x_1^2}$$

Eliminating the electric potential  $\Phi$  gives

$$\mathbf{r} \frac{\partial^2 u_3}{\partial t^2} = \left( c_{55} + \frac{e_{x_1,5}^2}{\mathbf{e}_{11}} \right) \frac{\partial^2 u_3}{\partial x_1^2}$$

It should be noted that this equation is identical in form to the wave equation for non-piezoelectric materials in equation (3-24) with the substitution for the term in parentheses:

$$c'_{55} = c_{55} \left( 1 + \frac{e_{x_1,5}^2}{c_{55} \mathbf{e}_{11}} \right) = c_{55} (1 + K^2)$$

The stiffness parameters have been increased by the factor  $(1+K^2)$ , which represents the influence of piezoelectric effect, known as piezoelectric stiffening, to the elastic stiffness constants. The wave velocity will be increased through piezoelectric stiffening relative to that of non-piezoelectric materials. The general expression is

$$c'_{ijkl} \equiv c_{ijkl} (1 + K^2_{ijkl}) \quad (3-54)$$

where  $K_{ijkl}$  is the electromechanical coupling coefficient. Since  $K^2$  is less than unity, the perturbation in wave velocity caused by piezoelectric stiffening can be written as

$$\frac{\Delta \mathbf{u}}{\mathbf{u}} = \left[ (1 + K^2)^{1/2} - 1 \right] \cong \frac{K^2}{2} \quad (3-55)$$

where the velocity  $\mathbf{u}$  is given by equation (3-34) and  $\mathbf{D} \mathbf{u} = \mathbf{u}' - \mathbf{u}$ . The velocity of a piezoelectric material without influence of piezoelectric stiffening can be done by metalised surface cover.

For most crystalline materials the internal structure is referenced to an orthogonal set of axes denoted by upper-case symbols X, Y, Z, with directions defined in relation to the crystal lattice. The convention usually adopted is to define the surface normal direction, followed by the propagation direction. For example, "YZ-lithium niobate" means that the surface is normal to the crystal Y-axis and propagation direction is parallel to the crystal Z-axis. The orientation of the surface normal is also referred to as the cut, so that for YZ-lithium niobate the crystal is Y-cut.

For a piezoelectric material it is necessary to use an electrical boundary condition at the surface in addition to the stress-free condition which applies for isotropic materials. Two cases are usually considered. In the first case the space above the surface is vacuum, so that there are no free charges. This is known as the *free-surface* case, where there will be a potential in the vacuum above the surface. In the second case, the surface is assumed to be covered with a thin metal layer with infinite conductivity, which shorts out the horizontal component of the electric field on the surface but retains the mechanical boundary conditions. This is called *metallised* case. Therefore the piezoelectric effect will vanish because of the lack of an electrical potential difference. These two cases generally have different velocities of wave propagation giving rise to the piezoelectric stiffening in equation (3-55). The electromechanical coupling coefficient  $K^2$  depends not only on the substrate types, but also on the propagating direction and the type of wave [Gentes 1994]. Table 3-2 lists popular piezoelectric materials and their properties.

In the case of surface wave, for example, the Rayleigh wave solutions for an isotropic half-space was obtained by adding partial waves, namely longitudinal and transverse waves, with  $x_1$ -component of their wave vectors equal. For anisotropic, piezoelectric solids, the properties of Rayleigh waves are quite similar to those in an isotropic solid. The trajectory of the movement of a volume element on the surface of an

anisotropic solid is also an ellipse; however, it does not have to be limited to the sagittal plane. The amplitude of the Rayleigh waves in anisotropic solids decays with the distance from surface, therefore, the energy of the wave concentrates mostly near the surface. But now the components of the displacement  $u_i$  must not be real numbers anymore, the additional imaginary part indicates that the decay of the wave is exponentially attenuated and has an oscillatory behavior in  $x_3$ -direction. The most difference is that the particle displacement couples strongly to the electric potential. Therefore, besides the mechanical counterforce, there is a contribution to the propagating velocity from the electric potential raising the velocity.

Table 3-2 Properties of Piezoelectric materials

Material	Cut	direction	$K^2$	$u$ [m/s]	Wave type
quartz	ST	X	0.18	3158	Rayleigh wave
quartz	ST	Y	0.3-0.4	4994	Love wave
LiNbO <sub>3</sub>	41° rot Y	X	0.35	4792	Leaky wave (Shear wave)
LiTaO <sub>3</sub>	126° rot Y	X	2.1	3425	Leaky wave (Rayleigh wave)
LiTaO <sub>3</sub>	36° rot Y	X	4.7	4177	Leaky wave (Shear wave)

### 3.3.4 Rayleigh wave at liquid-solid interface

The Rayleigh wave discussed in the above sections propagates on the surface of a solid and can be treated as a combination of two partial waves, one of which is a transverse (shear vertical) wave with polarization perpendicular to the propagating direction; the other is a longitudinal wave with polarization parallel to the propagation.

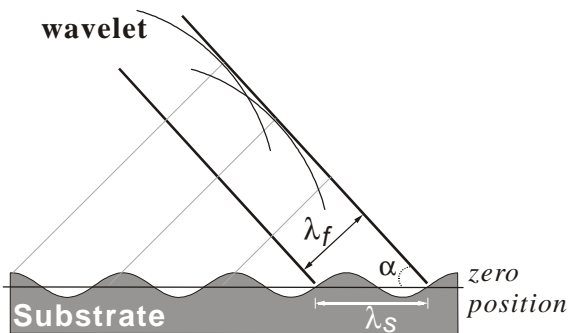


Fig.3-7 The Rayleigh wave with wavelength  $\lambda_s$  propagating at the liquid-solid interface will generate compressional waves with a wavelength  $\lambda_f$  into the liquid. The energy of the Rayleigh wave will therefore decay and result in a great attenuation.  $\alpha$  is the angle between the wave front of radiated waves and substrate surface.

It was obtained by assuming that the lower half-space consists of piezoelectric material and the upper half-space is vacuum. If the half-space in contact with the solid surface is not vacuum, but a gas or a liquid, then the influences of pressure, liquid viscosity, electrical conductance, dielectric constant...etc, have to be taken into account for the properties of wave propagation. For liquid sensing, like for immunosensors, liquid loading

contributes to acoustic wave attenuation and velocity change. If the aqueous solution is incompressible and the restoring force against stress is negligible, then the longitudinal wave on the surface will travel with a higher velocity than that without liquid loading. The situation is different for the transverse (shear vertical) component of a Rayleigh wave traveling at the liquid-solid interface. As shown in Fig.3-7, for transverse wave, the displacement of a volume element is vertical to the surface, resulting in a pressure oscillation at the solid-liquid interface. In this case, the attenuation will be very strong due to the generation of periodic compressional waves in the liquid in contact with the substrate. In other words, the transverse component of the Rayleigh wave results in a coupling of acoustic wave energy from the substrate into the liquid. The constructive superposition of these compressional waves in the liquid forms a wave front which is at an angle  $\mathbf{a}$  to the surface of the substrate. Let the velocities of the compressional wave in the liquid and of the Rayleigh wave in the substrate be  $\mathbf{u}_f$  and  $\mathbf{u}_s$ , respectively, then the compressional waves in the liquid will be radiated at an angle  $\mathbf{a}$  :

$$\sin \mathbf{a} = \frac{l_f}{l_s} = \frac{\mathbf{u}_f}{\mathbf{u}_s}. \quad (3-56)$$

From the above relation, a constructive superposition of wavelets in liquid will always exist as long as the velocity of the compressional wave is less than that of the Rayleigh wave and results in a strong attenuation. In Table 3-2, the listed Rayleigh wave velocities of different piezoelectric materials are much higher than the acoustic wave velocities in liquid. For example, in distilled water the acoustic velocity is only 1483 m/s, and 1522 m/s in sea water [Kohlrausch 1986]. Therefore, the utilization of the Rayleigh waves with liquid loading environments is not possible [Shiokawa 1988]. However, for the application in gaseous environments, the attenuation of Rayleigh wave is not as strong as under liquid loading, since the decay factor for amplitude of a Rayleigh wave is  $e^{(-\mathbf{w}lZ_{gas})}$ , where  $Z_{gas} = \mathbf{u} \cdot \mathbf{r}_{gas}$  is the acoustic impedance of the gas,  $\mathbf{r}_{gas}$  is the mass density of gas,  $l$  is the length the Rayleigh wave has travelled, and  $\mathbf{w}$  is the frequency of the Rayleigh wave. Since density and acoustic wave velocity of a gas are very small, as a result, as long as the frequency is not in the giga-hertz range, the energy dispersion from the substrate into the gas is quite small [Auld 1990].

### 3.3.5 Shear horizontal wave

Acoustic waves with a vertical polarization component are not suitable for operating in liquid environments. Only waves with pure shear horizontal polarization are not subject to strong attenuation and can be utilized for sensing in liquids. The particle displacement of such a shear horizontal wave is vertical to the propagating direction and also

perpendicular to the sagittal plane. Surface shear horizontal acoustic waves (SH-SAW) can be roughly sorted in three groups:

### 1. Surface-Skimming Bulk Wave (SSBW)

The surface-skimming bulk wave has the propagation characteristics of a transverse bulk wave with a dominant shear horizontal polarization. It travels close to and under the surface with a very small angle  $q$  against the surface, and is therefore called a “*surface-skimming bulk wave*”, or SSBW. Thus,

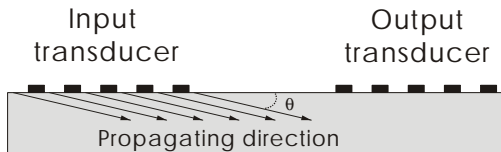


*Fig.3-8 Surface-skimming bulk waves propagate closely to the surface with an angle  $q$  against the surface.*

the energy of a SSBW wave is localized near the surface and decays very slowly into the bulk. A SSBW wave can propagate with the wave vector  $k$  parallel to the surface, while satisfying the surface boundary condition, and equal to the bulk velocity and attenuation essentially

unchanged in the infinite medium. At large distances a wave generated at  $x = 0$  can be expected to have an amplitude proportional to  $x^{-1/2}$ , as deduced from power conservation [Lewis 1977].

### 2. Leaky wave

For some special propagating directions in a crystal, surface wave solutions can not exist without including a partial wave corresponding to a shear-vertical bulk wave. In this case, the wave will decay into the bulk due to the bulk wave component. However, if the shear wave component only contributes a small fraction of the total displacement, the energy lost will be small. In this manner, the property of the wave is quite similar to the real surface wave, except that there is a small amount of attenuation into the bulk. Therefore, it is called “*Leaky surface wave*”.

### 3. Love wave

Love waves are also shear horizontal polarized waves and carried in a thin layer medium lying on a semi-infinite solid [Love 1911]. As shown in Fig.3-9, the wave in the upper layer will be guided by the shear horizontal bulk wave generated at the boundary of a substrate, if the velocity of transverse bulk wave is higher than that of the wave in the layer. At high frequencies, such that the wavelength is less

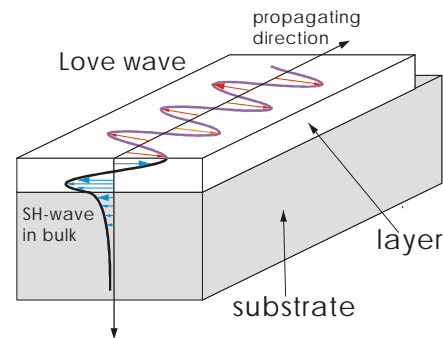


*Fig.3-9 Scheme of the propagation of a Love wave. Love waves are SH-surface waves existing only on the layered-surface of a substrate.*

than the layer thickness, the wave will be concentrated in the layer and has a velocity close to the shear horizontal wave velocity in the free layer. At low frequencies, the love wave velocity will be close to the shear horizontal bulk wave velocity of the substrate and the penetration depth into the substrate will be large.

The substrate we use for generating surface acoustic waves is a  $36^\circ$  rotation, YX cut lithium tantalate ( $36^\circ$  rot YX-LiTaO<sub>3</sub>). Under such a cut of LiTaO<sub>3</sub>, the attenuation of the leaky surface wave will be reduced to minimum. The attenuation of a leaky surface wave on YX-cut LiTaO<sub>3</sub> surfaces with respect to the angle of rotation relative to the wave propagating direction is shown in Fig.3-10(a). The lowest attenuation occurs when the propagating direction is along the Y axis with an angle of 36 degree from the X axis; thus, this orientation is also chosen as the optimal cut of LiTaO<sub>3</sub>.

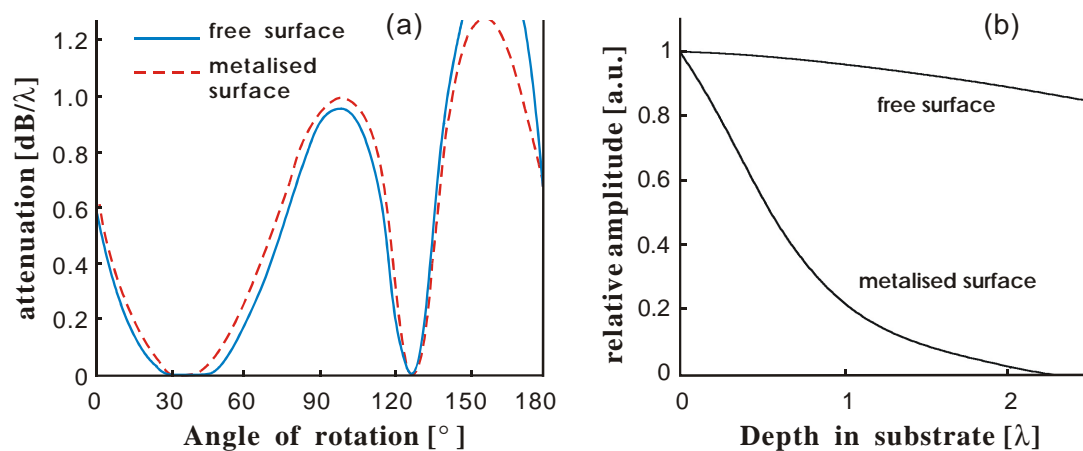


Fig.3-10 (a) Attenuation of the leaky surface wave on YX-LiTaO<sub>3</sub> crystal with different cuts of rotation angles. The minimal attenuation occurs when the angle is  $36^\circ$ . (b) The relative amplitude of surface waves about depth from the free and metalised surface of  $36^\circ$  rot YX-LiTaO<sub>3</sub> crystal. The surface wave concentrates closely to the metalised surface, while at free surface the wave penetrates deep into the substrate. [Yamanouchi 1979].

Fig.3-10(b) shows the attenuation of the leaky surface wave in a slice of  $36^\circ$  rot YX-LiTaO<sub>3</sub> crystal under different boundary condition on the surface. In the free surface case, the penetration depth of the wave is about  $10\lambda$ , while in the case of metalised surface (i.e. the piezoelectric effect is annihilated) the penetration depth is reduced to only  $2\lambda$ , where  $\lambda$  is the wave length of the surface wave. This result shows that the piezoelectric effect contributes greatly to the propagation of surface wave on this crystal cut of crystal [Yamanouchi 1979].

In practice, a thin layer of different materials, such as SiO<sub>2</sub> or polymer, was used to coat the surface of the LiTaO<sub>3</sub> to generate a “Love wave”. The main advantage of this

design is that such shear horizontal surface wave can be easily “transformed” from a bulk shear wave. Since the Love wave exists only close to the thin coating layer, the decay of surface wave into substrate can be minimized.

### 3.4 Response of surface wave sensor

The above sections have indicated parameters relevant for a surface wave on or near the surface of a substrate. The factors which may influence the propagation of surface waves are the keys to develop a surface wave sensor. Since the wave travels near the surface and its energy is concentrated within a depth of several wave lengths, any interaction between the substrate surface and the outer surroundings may easily affect the propagation of the surface wave. The most commonly used propagation property for developing a surface wave sensor is the phase velocity of the surface wave. The parameters which affect the propagation velocity of a surface wave are various and can be expressed in the following formula:

$$\frac{\Delta \mathbf{u}}{\mathbf{u}_0} = \frac{1}{\mathbf{u}_0} \left[ \frac{\partial \mathbf{u}}{\partial m} \Delta m + \frac{\partial \mathbf{u}}{\partial c} \Delta c + \frac{\partial \mathbf{u}}{\partial e} \Delta e + \frac{\partial \mathbf{u}}{\partial s} \Delta s + \frac{\partial \mathbf{u}}{\partial T} \Delta T + \frac{\partial \mathbf{u}}{\partial p} \Delta p + \frac{\partial \mathbf{u}}{\partial h} \Delta h + \dots \right] \quad (3-57)$$

where  $\mathbf{u}_0$  is the initial phase velocity of the surface wave,  $m$  the mass loading on the surface,  $c$  the stiffness,  $e$  the dielectric constant,  $s$  the surface conductivity,  $T$  the temperature,  $p$  the pressure, and  $h$  the viscosity. The influence of a certain parameter which affects the wave propagation can be obtained by keeping the other factors constant, and using a perturbational approach with appropriate boundary conditions [Auld 1990]. In our case, the additional mass on the surface due to specific binding of antigens and antibodies is the most significant factor which influences the propagation velocity of a surface wave. Therefore, it is necessary to suppress parameters other than the mass loading.

Besides the phase velocity, the attenuation of a surface wave also plays an important role to reflect the interaction between surroundings and the surface of a substrate. The parameters giving rise to a change in phase velocity and attenuation will be discussed in the following subsections.

### 3.4.1 Effect of elastic thin film coating (mass loading)

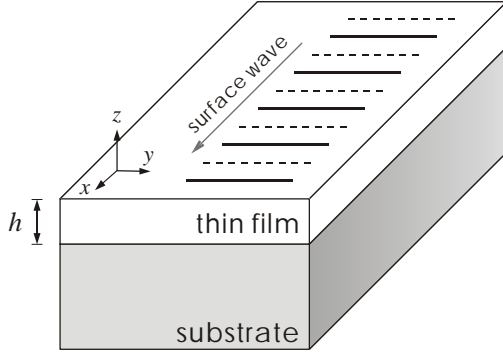


Fig. 3-11. The thin film with the thickness  $h$  is coated on the substrate surface. The surface wave propagates in the  $x$ -direction.

Mass loading on a substrate surface is a special mechanical disturbance to surface wave propagation. Many of surface wave sensors are based on velocity variation due to the mass change on the substrate surface. Mass loading is the most important mechanism that perturbs the propagation of surface wave. Consider a lossless, thin, isotropic film as waveguide resting on a substrate which can be characterized by a mass density  $\mathbf{r}'$ , a thickness  $h$  and Lamé constants  $\mathbf{I}' = c'_{12}$  and  $\mathbf{m}' = c'_{44}$ . Note that the primes

represent the quantities of the thin film. Suppose that the surface does not suffer any forces from outside (i.e. stress-free) [Fig.3-11]. For simplification, new indexes  $x, y, z$  are substituted for the old coordinate indexes  $x_1, x_2, x_3$ . If the surface wave propagates in  $x$ -direction while the  $z$ -direction is normal to the surface, then the equation of motion (equation 3-7) can be re-written as

$$\frac{\partial T'_{ix}}{\partial x} + \frac{\partial T'_{iz}}{\partial z} = \mathbf{r}' \frac{\partial^2 u_i}{\partial t^2} \quad (3-58)$$

since the assumption has been made that amplitude of the surface wave remains unchanged in  $y$ -direction and varies with  $x$  as  $e^{-\mathbf{g}x}$  in  $x$ -direction, i.e. the continuous propagation of a wave in the  $x$  direction is  $\bar{\mathbf{u}}(\mathbf{x}, \mathbf{y}, \mathbf{z}, \mathbf{t}) = \bar{\mathbf{u}}(\mathbf{y}, \mathbf{z}) \cdot \exp(i\omega t - \mathbf{g}x)$ . The factor  $\mathbf{g}$  is the complex propagation factor representing both attenuation and wave number:

$\mathbf{g} = \mathbf{a} + ik = \mathbf{a} + i(\omega/\mathbf{u}_0)$ , where  $\mathbf{a}$  is the attenuation constant,  $k$  is the wave number and  $\mathbf{u}_0$

the phase velocity of the wave. If the frequency is constant, then the changes in wave propagation factor can thus be represented by

$$\Delta \mathbf{g} = \Delta \mathbf{a} - ik_0 \frac{\Delta \mathbf{u}}{\mathbf{u}_0} \Rightarrow \frac{\Delta \mathbf{g}}{k_0} = \frac{\Delta \mathbf{a}}{k_0} - i \frac{\Delta \mathbf{u}}{\mathbf{u}_0} \quad (3-59)$$

where  $k_0$  is the unperturbed wave number. The real part and the imaginary part of equation (3-59) are attenuation and phase velocity, respectively. Furthermore, equation (3-58) can be rewritten as

$$\frac{\partial}{\partial z} T'_{iz} - \mathbf{g}' T'_{ix} = i\omega \mathbf{r}' \mathbf{u}'_i \quad i = x, y, z \quad (3-60)$$

here  $\mathbf{u}'_i = \partial u_i / \partial t$ . Using perturbation theory the solution of the above equations results in

a perturbation formula for a very thin isotropic film [Auld 1990]

$$\frac{\Delta \mathbf{g}}{k_0} = -\frac{\Delta \mathbf{u}}{\mathbf{u}_0} = \frac{\mathbf{u}_0 h}{4P} \left[ \left( \mathbf{r}' - \frac{4\mathbf{m}'}{\mathbf{u}_0^2} \frac{\mathbf{l}' + \mathbf{m}'}{\mathbf{l}' + 2\mathbf{m}'} \right) |\mathbf{u}_x|^2 + \left( \mathbf{r}' - \frac{\mathbf{m}'}{\mathbf{u}_0^2} \right) |\mathbf{u}_y|^2 + \mathbf{r}' |\mathbf{u}_z|^2 \right]_{z=0} \quad (3-61)$$

where  $P$  is the average unperturbed power flow per unit width in  $y$ -direction. For shear horizontal waves the above equation can be simplified since  $\mathbf{u}_x = \mathbf{u}_z = 0$  in the ideal case

$$\frac{\Delta \mathbf{u}}{\mathbf{u}_0} = -\frac{\mathbf{u}_0 h}{4P} \left[ \left( \mathbf{r}' - \frac{\mathbf{m}'}{\mathbf{u}_0^2} \right) |\mathbf{u}_y|^2 \right]_{z=0} = \frac{\Delta m}{4P \mathbf{u}_0} (\mathbf{u}_f^2 - \mathbf{u}_0^2) |\mathbf{u}_y|^2 \quad (3-62)$$

where  $\mathbf{u}_f = \sqrt{\mathbf{m}'/\mathbf{r}'}$ , is the surface wave velocity in the thin film, and  $\Delta m = h\mathbf{r}$  is the surface mass density. In general, the velocity  $\mathbf{u}_f$  in thin film is less than that in substrate  $\mathbf{u}_0$ . A comparison of the values  $|\mathbf{u}_i|^2/P$  of free and metallised surface of  $36^\circ$  rot-YX-LiTaO<sub>3</sub> are listed in Table 3-3 in units of  $10^{-12} \text{ m}^3 \text{ s}^{-2} / \text{W}$  [Shiokawa 1987]. These values are frequency dependent, where  $\omega$  is the angular frequency of the surface wave. If the thickness of a thin film is larger than half the surface wave length, the film cannot be treated as a perturbation of the wave and the above approaches are not valid any more. If the film is non-elastic, then the attenuation term will be not zero [Kondoh 1993]

$$\frac{\Delta \mathbf{a}}{k_0} = \frac{\mathbf{wh}}{4P\mathbf{u}_0} \mathbf{h} |\mathbf{u}_z|^2 \quad (3-63)$$

where  $\mathbf{h}$  is viscosity of the film. In practical application, a certain wave type will be preferred only if it has minimal attenuation, i.e. the particle velocities should be as small as possible in  $x$ - and  $z$ -direction in order to fit the equation (3-62) and (3-63).

Table 3-3 SAW velocities on the free- and metallised surface of  $36^\circ$  rot YX LiTaO<sub>3</sub>.

Substrate	Velocity [m/s]	$ \mathbf{u}_x ^2/P$	$ \mathbf{u}_y ^2/P$	$ \mathbf{u}_z ^2/P$
<i>36° rot-YX-LiTaO<sub>3</sub> (free surface)</i>	4172	0.0064 $\omega$	3.6864 $\omega$	0.0196 $\omega$
<i>36° rot-YX-LiTaO<sub>3</sub> (metallised surface)</i>	4077	0.0169 $\omega$	5.2441 $\omega$	0.0576 $\omega$

### 3.4.2 Effect of viscosity

Viscosity of the medium loaded on the substrate will also affect the surface wave especially for thick, highly concentrated solutions since viscosity represents the inner friction of liquid, in which the mechanical energy will be converted into thermal energy. Therefore, the main effect of viscosity is that the attenuation at a surface under liquid coating will be larger than in air or in vacuum. If we assume that a Newtonian fluid with a

viscosity  $h$  and a mass density  $r_l$  is loaded on the surface of a substrate, the velocity change and normalized attenuation are [Shiokawa 1987, Kondoh 1995]

$$\frac{\Delta u}{u_0} = -\frac{u_0 \cdot |u_y|^2}{4wP} \left( \sqrt{\frac{wh'r'_l}{2}} - \sqrt{\frac{whr_l}{2}} \right) \quad (3-64)$$

$$\frac{\Delta a}{k_0} = \frac{u_0}{4wP} \left[ |u_y|^2 \left( \sqrt{\frac{wh'r'_l}{2}} - \sqrt{\frac{whr_l}{2}} \right) + |u_z|^2 \left( \sqrt{r'_l c' - \frac{c'^2}{u_0^2}} - \sqrt{r_l c - \frac{c^2}{u_0^2}} \right) \right]$$

where  $\chi$  is the elasticity of a volume element. The primed (') values are for the perturbed surface wave. The first term of attenuation is the contribution of internal friction in the liquid i.e. the viscosity effect; the second term means the attenuation caused by the compressional wave generated in the liquid by the  $z$ -component of the surface wave (normal to the substrate surface).

### 3.4.3 Effect of electrical conductivity

Since the particle movement in a piezoelectric substrate on which a surface wave propagates is always associated with an electric field, electrical conductivity at the liquid-solid interface is another mechanism which has an important effect on the velocity and attenuation of ultrasonic surface wave. This perturbation due to the change of surface conductivity has been exploited for liquid-phase detection of ionic species using Love wave devices.

When a surface acoustic wave propagates in a piezoelectric material, a layer of bound charges at the surface is generated. These bound charges are the sources of the wave potential  $F$  discussed previously. If a conductive film is placed onto the surface of the piezoelectric substrate, charge carriers in the film will redistribute to compensate for the bound charges generated by the surface wave. Thus, the piezoelectric effect will be weakened. The velocity change of the surface wave in a piezoelectric material coated with a conductive film is [Ricco 1985]

$$\frac{\Delta u}{u_0} = -\frac{K^2}{2} \frac{s^2}{s^2 + u_0^2 C_s^2} \quad (3-65)$$

where  $K^2$  is the electromechanical coupling constant,  $s$  is the electrical conductivity of the film, and  $C_s = e_s + \epsilon_0$  where  $\epsilon_s$  is the dielectric permittivity per unit length of the substrate. These bound charges also cause an ohmic power loss

$$\frac{\Delta a}{k_0} = \frac{K^2}{2} \frac{u_0 C_s s}{s^2 + u_0^2 C_s^2} \quad (3-66)$$

Furthermore, if the surface is covered by a conducting liquid instead of a conducting film, equations (3-65) and (3-66) have to be modified. In this case the polarization of the

liquid has to be taken into account.

Generally, electronic and atomic polarizations occur on timescales corresponding to frequencies in excess of  $10^6$  MHz when an electric field is applied to a dielectric medium. Hence, these polarizations have little effect at typical ultrasonic wave operating frequencies. However, molecular reorientations occur in the picosecond range, i.e. corresponding to frequencies of  $10^4$ - $10^6$  MHz, which implies that the electric potential wave accompanying the surface acoustic wave can couple through induced dipole reorientation, resulting in a dielectric loss term. For piezoelectric material with high electromechanical coupling constant ( $K^2$ ), such as lithium niobate and lithium tantalate, the dielectric loss may be quite serious.

The dielectric relaxation frequency is given by [Alder 1971]

$$\mathbf{w}_R = \frac{\mathbf{s}_f}{\mathbf{e}_s + \mathbf{e}_f} \quad (3-67)$$

where  $\mathbf{s}_f$  is the liquid conductivity,  $\mathbf{e}_s$  and  $\mathbf{e}_f$  are dielectric constant of the substrate and solution, respectively. When the applied frequency is greater than  $\mathbf{w}_R$ , ions in solution cannot redistribute fast enough to follow the changing potential, which results in that the electrical double layer is never fully formed, so the electric field penetrates into the bulk solution and causes energy loss. The fractional velocity shift and attenuation per wave number under conducting liquid loading is given by [Josse 1991]

$$\begin{aligned} \frac{\Delta \mathbf{u}}{\mathbf{u}_0} &= K^2 \left( \frac{\mathbf{e}_s}{\mathbf{e}_s + \mathbf{e}_f} \right) \frac{\mathbf{s}_f^2}{\mathbf{s}_f^2 + \mathbf{w}^2 (\mathbf{e}_s + \mathbf{e}_f)^2} \\ \frac{\Delta \mathbf{a}}{k_0} &= K^2 \left( \frac{\mathbf{e}_s}{\mathbf{e}_s + \mathbf{e}_f} \right) \frac{\mathbf{w} \mathbf{s}_f (\mathbf{e}_s + \mathbf{e}_f)}{\mathbf{s}_f^2 + \mathbf{w}^2 (\mathbf{e}_s + \mathbf{e}_f)^2} \end{aligned} \quad (3-68)$$

Fig.3-12 and 3-13 show the velocity shift and attenuation versus liquid conductivities with respect to quartz and lithium tantalate respectively. It is obvious to see that the velocity changes in both cases are saturated and become stable at higher liquid conductivities. The attenuations also reach a maximum when the liquid conductivity satisfies equation (3-67) at a fixed operating frequency (400 MHz, in these cases). It is noted that due to the larger  $K^2$  the sensitivity of the velocity change of lithium tantalate with respect to liquid conductivity is higher than that of quartz as expected from equation (3-65).

Equation (3-68) also shows that the acoustoelectric interaction has the least effect for low-conductivity solutions since in such case the liquid conductivity does not dominate the denominators of the above equations i.e.  $\mathbf{s}_f \leq \mathbf{w} (\mathbf{e}_s + \mathbf{e}_f)$ ; for solutions with higher conductivities, the interaction should be either taken into account or be minimized by deposition of a metal film onto the surface of the piezoelectric substrate.

1. Solutions of high conductivity are recommended for SAW biosensor application, because the sensitivities to attenuation and velocity are always in saturation.
2. Since both, velocity and attenuation of a SAW device are proportional to the

electromechanical coupling constant  $K^2$  when loaded with conducting liquid, it is preferred to choose piezoelectric materials with small  $K^2$  for practical application.

- Alternatively, it is recommended to deposit a thin metal film on the substrate surface in order to shield it from the conducting liquid, so that the conductivity change does not affect the surface wave. Thin insulator films can also partially degrade the negative effect of liquid conductivity, which will be discussed later.

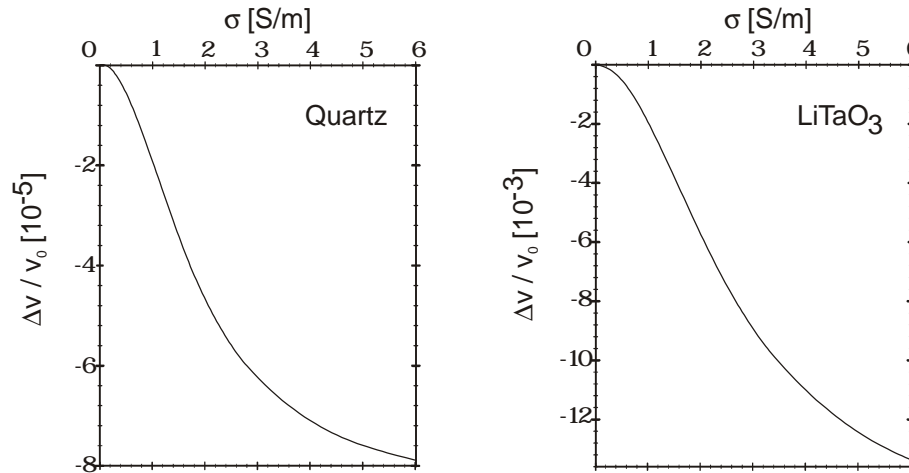


Fig.3-12 Normalized velocity change of surface acoustic waves against the conductivities of loaded liquid on the quartz (left) and LiTaO<sub>3</sub> (right). The operation frequency is 400 MHz. It should be noted that the relative velocity change of waves in quartz is about 100 times smaller than that of LiTaO<sub>3</sub>.

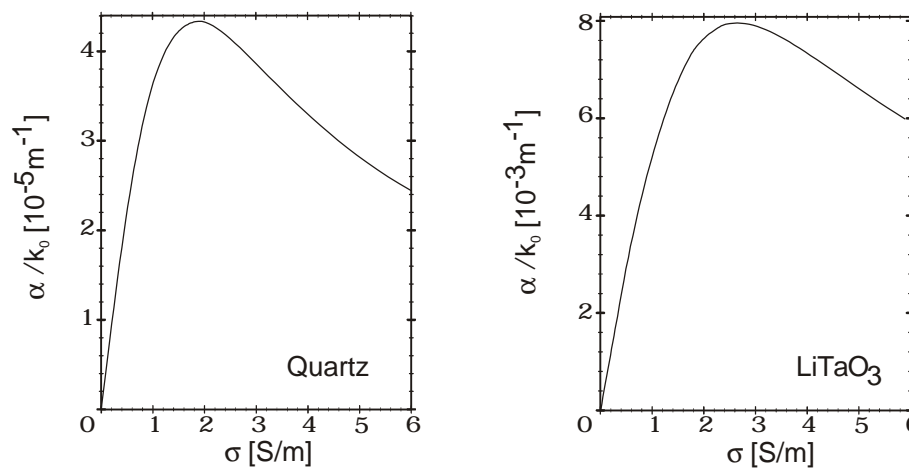


Fig.3-13 Attenuation of surface acoustic waves against the conductivities of the loaded liquid on the quartz(left) and LiTaO<sub>3</sub>(right). There are maximums for both substrates with given conductivities. Likewise, the attenuation in quartz is 100 times less than that in LiTaO<sub>3</sub> for a given change in the liquid conductivities.

### 3.4.4 Effect of temperature

Deformation and particle motions of a substrate are directly affected by the substrate temperature. As a result, mechanical and electrical properties of a substrate, such as elasticity, dielectricity, piezoelectricity, which have a relationship with the propagation of the surface wave, will also be changed when a temperature variation occurs in the substrate. The temperature dependence of the surface wave velocity can be expressed by a velocity function of temperature in Taylor series:

$$\mathbf{u}(T) = \mathbf{u}(T_0) + \left. \frac{\partial \mathbf{u}}{\partial T} \right|_{T_0} (T - T_0) + \frac{1}{2} \left. \frac{\partial^2 \mathbf{u}}{\partial T^2} \right|_{T_0} (T - T_0)^2 + \dots \quad (3-69)$$

from which we get the first and second order temperature coefficients of the surface wave

$$\mathbf{g}_1 = \left. \frac{\partial \mathbf{u}}{\partial T} \right|_{T_0} \quad \text{and} \quad \mathbf{g}_2 = \left. \frac{\partial^2 \mathbf{u}}{\partial T^2} \right|_{T_0} \quad (3-70)$$

Temperature coefficients depend on the direction of wave propagation in a given substrate; there often exists a special direction along which the temperature coefficients compensate precisely, i.e. the temperature dependence of the wave velocity vanishes. Such a cut for a given piezoelectric material is called “Cut of temperature compensation”. For example,  $\mathbf{g}_1$  is just compensated by  $\mathbf{g}_2$  for ST cut quartz. But for  $\text{LiTaO}_3$  crystal, there is no such cut that can avoid the effect of temperature. However, the wave velocity will have minimal temperature dependence only at an optimal direction about 40 degrees for YX- $\text{LiTaO}_3$  [Fig. 3-14].

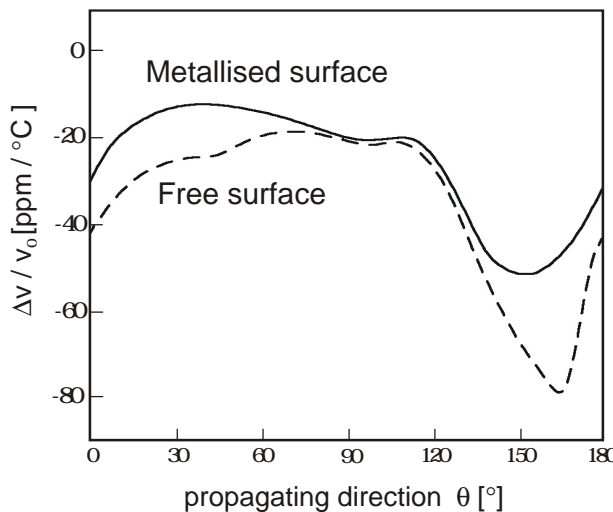


Fig.3-14 Velocity changes per degree ( $^{\circ}\text{C}$ ) against propagating direction in free- and metallised surface on a  $\text{LiTaO}_3$  substrate. This temperature effect always exists, but at smaller angles this temperature effect is minimized.

### 3.4.5 Mass sensitivity

In the case of the surface wave immunosensor, the antibody-antigen binding results

in a mass change on the device surface. The propagation of the surface wave will therefore be perturbed which leads to a change in phase velocity and attenuation. The mass sensitivity at constant wave frequency of the device is given by

$$S = \lim_{\Delta M \rightarrow 0} \frac{1}{\mathbf{u}} \frac{\Delta \mathbf{u}}{\Delta M} \cong \lim_{\substack{\Delta M \rightarrow 0 \\ \mathbf{u} \rightarrow \mathbf{u}_0}} \frac{1}{\mathbf{u}_0} \frac{\Delta \mathbf{u}}{\Delta M} \quad (3-71)$$

which means the change of phase velocity with respect to the actual velocity for an increase in the mass per unit area, where  $\mathbf{u}_0$  and  $\mathbf{u}$  are velocity before and after mass deposition, respectively. Mass sensitivity has the dimension of [area/mass]. For practical application, what we measure is not the phase velocity but the phase angle since

$$\frac{\Delta \mathbf{u}}{\mathbf{u}_0} = - \frac{\Delta \Phi}{\Phi_0} \quad (3-72)$$

where the phase angle  $F_0 = \mathbf{w}L / \mathbf{u}_0$  and  $L$  is the length of delay line of the device which will be discussed in the next chapter. From equation (3-62) and (3-72) the mass change per unit area can be written as

$$\Delta m = \frac{\Delta \Phi}{\Phi_0} \cdot \frac{4P}{|\mathbf{u}_y|^2} \cdot \frac{\mathbf{u}_0}{(\mathbf{u}_f^2 - \mathbf{u}_0^2)} \quad (3-73)$$

Since  $|\mathbf{u}_y|^2/4P \sim \mathbf{w}$  [Falshold 1984], the relative velocity change is proportional to the wave frequency according to equation (3-62), then the absolute change in phase angle  $\mathbf{DF} = F_0 \Delta \mathbf{u} / \mathbf{u}_0$  due to the mass effect is therefore proportional to  $\mathbf{w}^2$ . Similarly, from equation (3-64), the absolute phase change due to viscosity effect is proportional to  $\mathbf{w}^{3/2}$ . Consequently, the sensitivity to mass change of a SAW device is determined by the minimal phase change  $\mathbf{DF}_{\min} / F_0$ , since all other terms in equation (3-72) are already

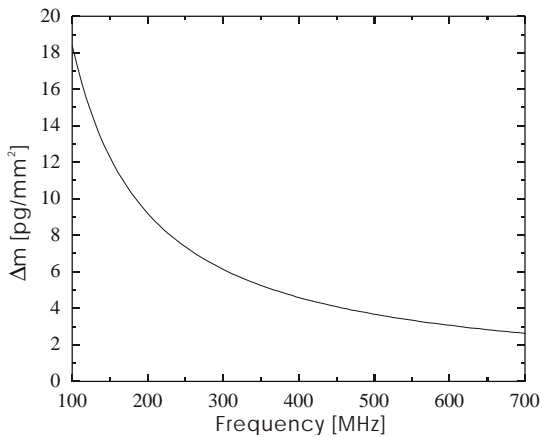


Fig.3-15 The minimal detectable mass change is proportional to the inverse of the wave frequency on LiTaO<sub>3</sub>.

known. For example, the minimal mass change  $\mathbf{D}m_{\min}$  which can be detected by SAW device based on 36° rot YX-LiTaO<sub>3</sub> at an operating frequency of 430 MHz is about  $\mathbf{D}m_{\min} \sim 17000 \cdot (\mathbf{DF}_{\min} / F_0)$  [ng/mm<sup>2</sup>]. It should be noted that for a given phase change,  $\mathbf{D}m$  in equation (3-73) is proportional to  $1/\mathbf{w}$  [Fig.3-15]. For Love wave sensors, the surface coating as waveguide will also affect the sensitivity. In the following chapter, the compromise between the thickness of surface coating and input attenuation of the Love wave sensor will be introduced in detail.

# Chapter 4

## Design of Surface Acoustic Wave Immunosenors

In last chapter, the theory and basic properties of surface acoustic waves propagating on a piezoelectric substrate were introduced. Now, the development of an immunosensor based on surface acoustic waves and its application will be discussed further, including the techniques to excite and receive ultrasonic waves on the substrate surface. The electronic signal processing for the ultrasonic wave device will also be presented and, finally, a number of practical investigations of antibody-antigen binding using this SAW immunosensor will be demonstrated.

### 4.1 Excitation and detection of surface waves

#### 4.1.1 Interdigital transducers

Two sets of symmetrical *interdigital transducer* (IDT) are the most commonly used design for generating and receiving surface waves by exploiting the piezoelectric effect of the substrate, which is illustrated in Fig.4-1. The transducers consist of identical electrodes connected alternatively to metal bus-bars. When an oscillatory voltage is applied, the

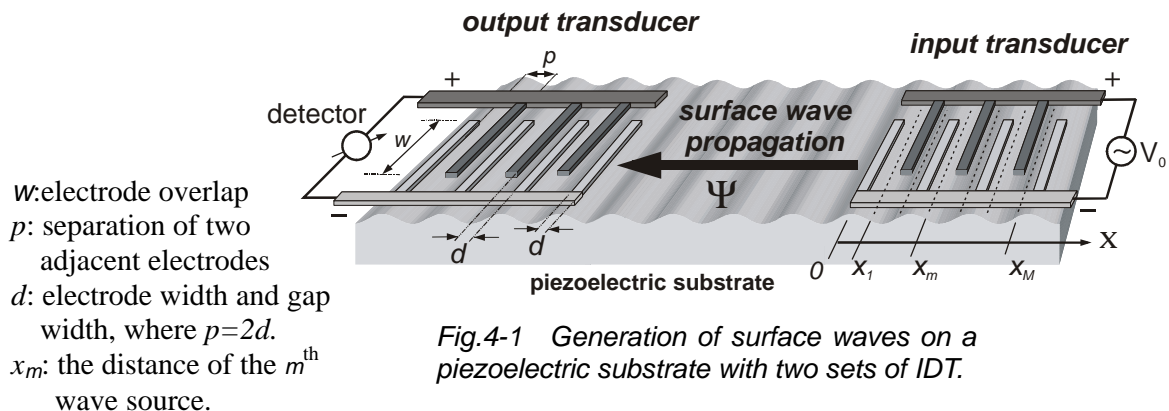


Fig.4-1 Generation of surface waves on a piezoelectric substrate with two sets of IDT.

input transducer generates an electric field which is spatially periodic with a length  $2p$ , where  $p$  is the spacing of adjacent electrodes. A consistent pattern of mechanical displacements are induced due to the inverse-piezoelectric effect. If the transducer spatial period  $2p$  is equal to the wavelength  $\lambda$  of the surface wave, the wave will couple with the output transducer and be converted to a voltage appearing at the output transducer owing to the direct-piezoelectric effect. It should be noted that the surface waves generated by the input transducer propagate always in two directions: one is toward the output transducer and the other one is in the opposite direction. Therefore, half of the power is radiated in the unwanted direction, giving a power loss of 3 dB [decibel]. For devices with two sets of transducers the loss is 6 dB.  $W$  is the length of overlap between two adjacent electrodes, which influences the diffraction spreading (relevant for attenuation) of the surface wave and the transducer impedance.

### 4.1.2 Delta function model

The fundamental center frequency  $f_0$  is defined as the frequency at which the transducer periodicity equals the wavelength of the surface wave, i.e.  $f_0 = \mathbf{u}_0/2p$ , where  $\mathbf{u}_0$  is the velocity of the surface wave for a given substrate. In practice, the waves generated by the source electrodes will be disturbed by the other electrodes that they pass under. In order to study the ideal transducer behavior, this disturbance is neglected in the delta function model [Tancrell 1971]. The total amplitude of the surface waves generated by an IDT with an alternating voltage  $V_0$  is given by

$$\Psi(x) = V_0 \cdot E \cdot A(\mathbf{w}) \cdot \exp[i(kx - \mathbf{w}t)], \quad \text{where } A(\mathbf{w}) = \sum_{m=1}^M C_m \exp(-ikx_m) \quad (4-1)$$

where  $E$  is associated with the substrate and IDT geometry and varies a little with frequency, thus it can be treated as a constant;  $A(\mathbf{w})$  is the superposition of individual waves generated from each source electrode and  $M$  is the total number of source electrodes. The position of the  $m^{\text{th}}$  source can be expressed by  $x_m = mp$ . The factor  $C_m = \pm 1$  depends on the polarity of the electric field. In the case of a single-electrode IDT structure, the width of an electrode is normally the same as the separation between electrodes ( $d = p/2 = \lambda/4$ ). The factor  $A(\mathbf{w})$  can be simplified to

$$A(\mathbf{w}) = -\exp[i(M-1)\mathbf{q}/2] \cdot \frac{\sin(-M\frac{\mathbf{q}}{2})}{\sin(-\frac{\mathbf{q}}{2})} \Rightarrow |A(\mathbf{w})| = \left| \frac{\sin(M\frac{\mathbf{q}}{2})}{\sin(\frac{\mathbf{q}}{2})} \right| \approx M \cdot \left| \frac{\sin(\frac{\mathbf{q}}{2})}{\sin(\frac{\mathbf{q}}{2})} \right| \quad (4-2)$$

where  $\mathbf{q} = p - k p = p(\mathbf{w}_0 - \mathbf{w})/\mathbf{w}_0$  with  $\mathbf{w}_0 = 2pf_0$ . The magnitude of  $A(f = \mathbf{w}/2p)$  is shown as a function of frequency in Fig.4-2. The first maximum appears at frequency  $f_0$  called the fundamental response. The zeros nearest to  $f_0$  are at  $f = f_0 \pm 2f_0/M$ , so the bandwidth of this single-electrode IDT configuration is  $\Delta f = f - f_0 = 4f_0/M$ . Harmonic modes of the same amplitude happen at odd multiples of  $f_0$ , where  $N = (M-1)/2$ , the number of electrode pairs.

It is noted that the maximal magnitude of  $A(\omega)$  is proportional to the number of electrodes  $M$  for the single-electrode IDT configuration, but the bandwidth is proportional to the operating frequency  $f$  and *inverse* of electrode number  $M$ .

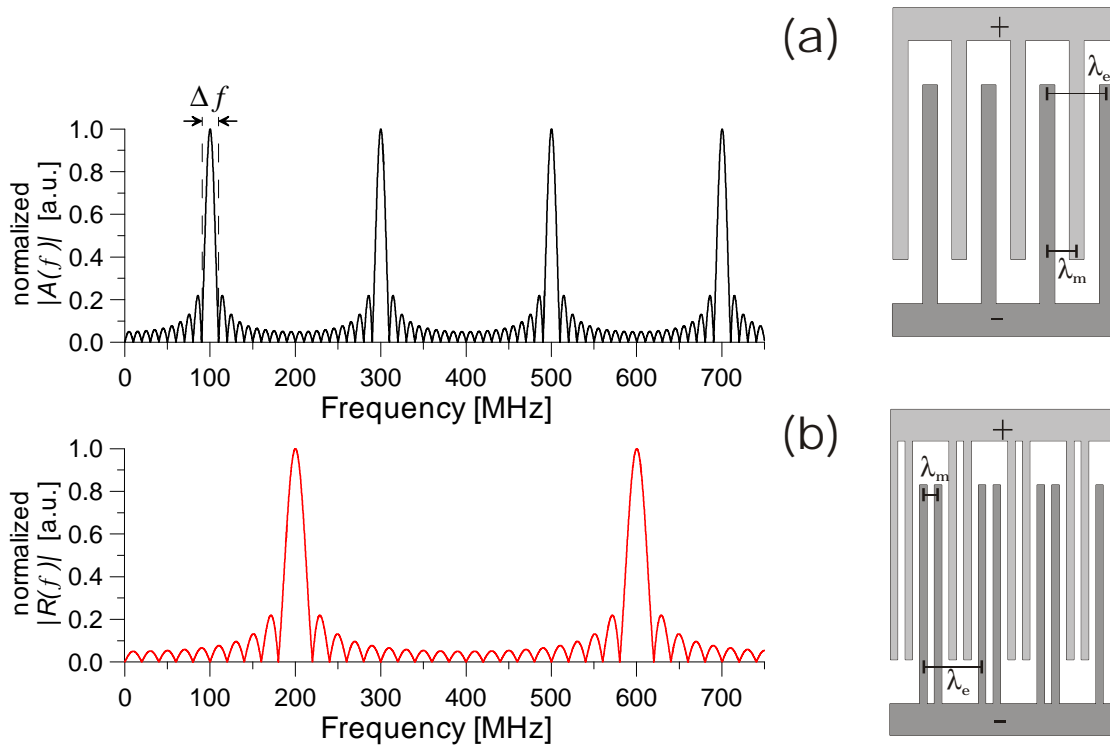


Fig.4-2 (a) The spectrum of normalized factor  $A(f)$  of a normal single-electrode IDT. The spatially mechanical period  $l_m$  is half the electrical period  $l_e$  (also the wavelength of surface wave). (b) The spectrum of the reflection coefficient  $R(f)$  of a double-electrode IDT. The  $R(f)$  of the single-electrode IDT has the maxima at the same frequencies as  $A(f)$ . But, for double-electrode IDT, the maxima of  $R(f)$  are between those of  $A(f)$ , therefore, the reflection of surface waves caused by the IDT electrodes can be minimized, where the mechanical period  $l_m$  is one fourth the electrical period  $l_e$ .

### 4.1.3 Double-electrode transducer

Although the delta function model can explain the generation of surface waves by an IDT in a simple way for first-order analysis, some important second-order effects cannot be specified by this model, for example, the reflection of incident surface waves by the IDT. The IDT fingers are constructed by depositing a thin metal film on the piezoelectric substrate with the following consequences: First, SAW velocities and acoustic impedance ( $Z_{ac} = \rho \mathbf{u}$ , where  $\rho$  and  $\mathbf{u}$  are mass density and SAW velocity of the substrate) of gap regions and metalised regions are different due to the fact that the metal electrodes shield the electric potential accompanying the SAW; and second, the metallised regions has an additional mass loading. Consequently, reflection occurs mostly at the boundary between

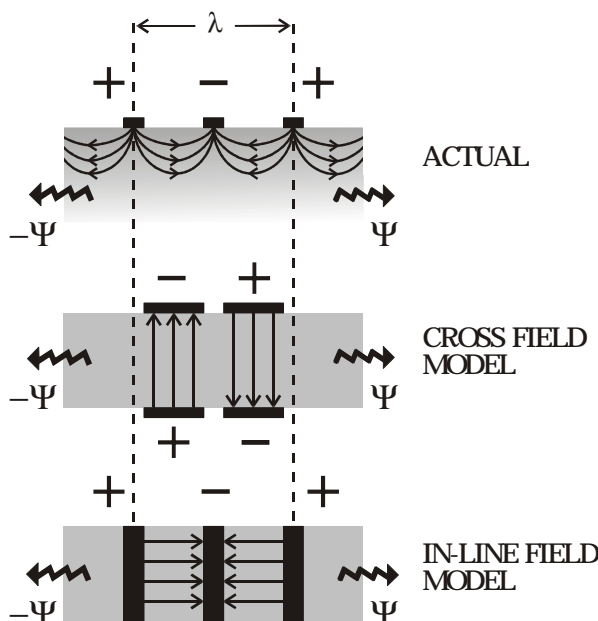
free and metallised surface because the electrodes cause mechanical and electrical perturbations of the surface. The surface waves reflected between IDT fingers result in unwanted ripple signals following or even coherently overlapping the main output signals if the electrode spacing  $I_m$  equals half the wavelength  $I_e$  (electrical period) [Fig.4-2(a)]. The reflection coefficient of single-electrode IDT with M electrodes is given by [Williamson 1977]

$$R(\mathbf{w}) \propto \tilde{r}(\mathbf{w}) \left| \frac{\sin(M \frac{\mathbf{q}}{2})}{\sin(\frac{\mathbf{q}}{2})} \right| \quad (4-3)$$

where  $\tilde{r}(\mathbf{w})$  is the reflection coefficient of single electrode. Except for the factor  $\tilde{r}(\mathbf{w})$ , equation (4-3) exhibits the same frequency response as the  $A(\mathbf{w})$  in equation (4-2). The maximum of the reflection occurs also at the fundamental center frequency  $f_0$  and other higher harmonic modes. This drawback can be overcome by using a “double-electrode” transducer, whose maximal reflection coefficient occurs between two maxima of  $A(\mathbf{w})$ , which is shown in Fig.4-2(b). For a double-electrode transducer, the mechanical period  $I_m$  is just one fourth the electrical period  $I_e$ .

The drawback of the double-electrode IDT is that for the same electrode spacing the fundamental center frequency is only half that of the single-electrode IDT. As described in the previous chapter, the sensitivity of surface wave devices is higher at high frequencies; therefore, in order to keep the same operating frequency, the electrode spacing of double-electrode IDT has to be reduced to half the spacing of a single-electrode IDT device.

#### 4.1.4 Impedance of interdigital transducers

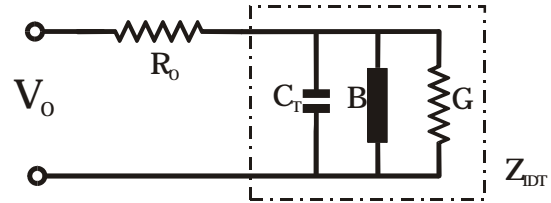


Since the IDTs are utilized for converting electrical energy into mechanical (acoustic) energy and vice versa, the electrical properties of the IDT itself have to be considered in order to characterize the energy transmitted by the IDT. A theoretical discussion of IDT impedance has been given by Smith *et al* [Smith 1969]. Fig.4-3 shows the actual electric field patterns between transducer electrodes in the substrate.

Fig.4-3 The actual electric fields between IDT electrodes are shown at the top, which can be modeled by “cross field” and “in-line field” models, depending on the piezoelectric properties of a substrate.

There are two models for IDT impedance analysis. In the “cross field” model, the electric field is assumed to be perpendicular to the substrate surface and SAW propagation, while in the “in-line field” model the field is parallel to both surface and SAW propagation. The substrate we use in this work, lithium tantalate, has a perpendicular piezoelectric effect which is stronger than parallel to the surface. Thus, the cross field model will be used for IDT impedance analysis.

Fig.4-4 Equivalent circuit of an IDT in the “cross field” model, where  $C_T$  is the static capacitance between electrodes,  $B$  and  $G$  are real and imaginary parts of acoustic admittance  $Y(\omega)$ .



According to the cross field model, the equivalent circuit for an IDT functioning as an acoustic wave generator is shown in Fig.4-4, where  $V_0$  is the voltage source,  $R_0$  is the ohmic resistance of the metal leads,  $C_T$  is the capacitance between two adjacent electrodes and depends on the overlap of opposing electrodes and the substrate material,  $B$  is the susceptance and  $G$  is the radiation conductance. The acoustic admittance  $Y(\omega)$  is defined as [Smith 1969]

$$Y(\omega) = G(\omega) + iB(\omega) \quad (4-4)$$

where

$$G(\omega) = 2G_0 \left( \tan \frac{q}{4} \cdot \sin \frac{Nq}{2} \right)^2, \quad q = \frac{2p\omega}{w_0}$$

$$B(\omega) = G_0 \tan \frac{q}{4} \left[ 4N + \tan \frac{q}{4} \cdot \sin Nq \right], \quad G_0 = \frac{w_0 C_T K^2}{2pN}$$

$N$  = number of electrode pairs.

$C_p$  = static capacitance of each electrode pair

$K^2$  = electromechanical coupling constant

$C_T = NC_p$  total capacitance of electrodes

Since the operating frequency is very close to the fundamental center frequency  $f_0$  of the IDT, at which an approximation of the trigonometric function possible, we get

$$G(\omega) \approx \hat{G} \left( \frac{\sin x}{x} \right)^2 \approx \frac{4}{p} K^2 w_0 C_p N^2, \quad x = Np \frac{\omega - \omega_0}{\omega_0}$$

$$B(\omega) \approx \hat{G} \left( \frac{\sin 2x - 2x}{2x^2} \right) \approx 0, \quad \hat{G} = \frac{4}{p} K^2 w_0 C_p N^2 = \frac{4}{p} K^2 w_0 C_T N$$

The only variables are finger pairs  $N$  and the capacitance of each finger pair  $C_p = W C_s$ , where  $C_s$  is the capacitance per unit length and  $W$  is the overlap of adjacent electrodes.

The parameter  $N$  will be determined according to the required bandwidth from the frequency response of the IDT, so that the impedance can be matched by an appropriate overlap  $W$ . The total impedance including the IDT capacitance in Fig.4-4 can then be written as

$$Z_{IDT}(\omega) = [G(\omega) + iB(\omega) + i\omega NC_p]^{-1} \quad (4-5)$$

Usually, the impedance of IDTs should match  $50 \Omega$  in the real part of  $Z_{IDT}$  and  $0 \Omega$  in the imaginary part since the cable leads and read-out devices have a impedance of  $50 \Omega$ . Fig.4-5 shows a simulation of DT impedance. The parameters are: 30 finger pairs, electrode overlap 2.2 mm, and  $C_p = 3.8 \text{ pF/cm}$  for  $36^\circ$  rot YX-LiTaO<sub>3</sub> with  $K^2 = 0.047$ . It should be noted that the best expected impedance matching region (gray zone) does not coincide with the fundamental center frequency ( $f_0 = 435 \text{ MHz}$ ) of this IDT configuration.

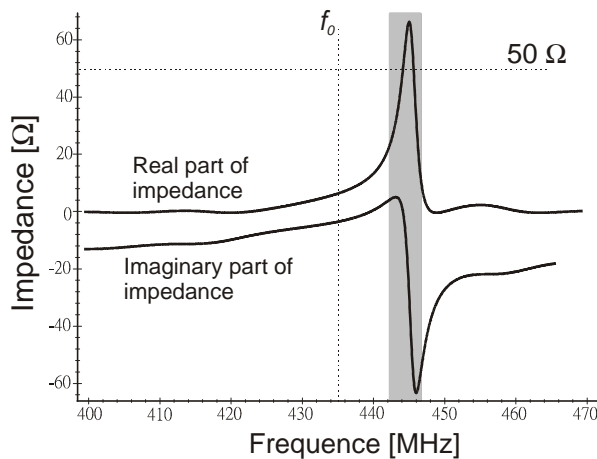


Fig.4-5 Impedance of IDTs with a center frequency  $f_0 = 435 \text{ MHz}$  on  $36^\circ$  rot YX LiTaO<sub>3</sub>. The operating frequency of SAW devices at which the impedance equals  $50 \Omega$  must not match the  $f_0$ .

## 4.2 Contactless SAW device

### 4.2.1 Inductively coupled SAW sensor

Typical transducers are connected to the voltage source and read-out device by metal wires using a micro-bonding or conductive silver paste method. The drawbacks for these methods are:

1. The touching point between lead wire and IDT may have a poor conductivity.
2. The metal micro-bonds are very sensitive to corrosion.
3. Micro-bonds are easily destroyed while performing liquid sensing, especially during the coating and cleaning process after experiments.

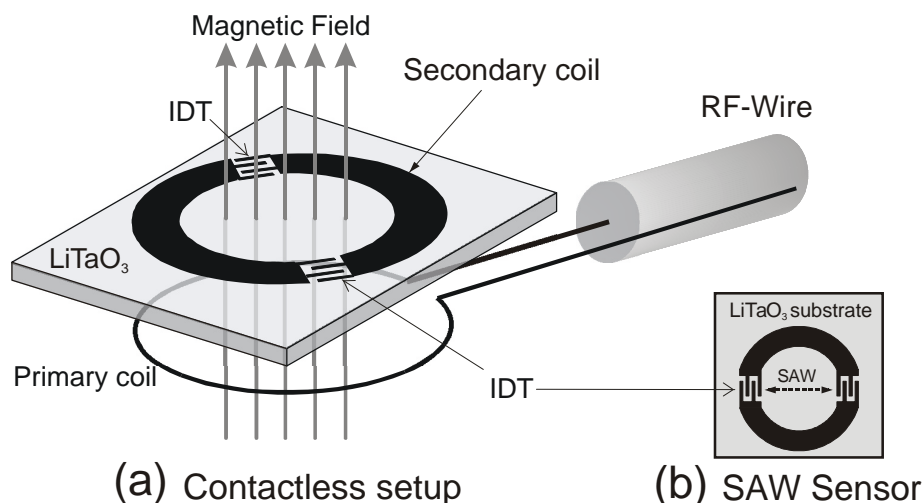


*Fig.4-6 (a) Setup of a contactless SAW sensor. The sensor is placed directly on the primary coil. The input and output RF-signals are transmitted between the coils by inductive coupling. (b) Top view of a contactless SAW sensor on LiTaO<sub>3</sub>. Surface waves propagate between IDTs.*

An alternative solution to the above drawbacks of direct contact is the “contactless”, inductively coupled sensor [Fig.4-6(a)]. The SAW sensor lies on the top of a primary coil and the bus-bars of the IDTs are connected together to form a ring shape [Fig.4-6(b)]. A RF-signal is sent to the primary coil, followed by the induced magnetic field generated within the coil center. Another corresponding RF-signal will then be induced in the second coil on the SAW sensor owing to the fluctuation of the magnetic field. As a result, both IDTs generate surface waves and each IDT receives waves coming from the opposite one after a few microseconds. The received signals will be induced back to the primary coil and then detected by the read-out device.

This contactless setup simplifies the fabrication and handling of the SAW sensor element since the direct contact of lead wires with the IDTs hinders the deposition of the required homogenous coating of waveguides for the Love wave sensor. The cleaning process becomes also easier because it is not necessary to pay attention to the lead wires any more.

### 4.2.2 Impedance matching

Since the contactless SAW devices are based on the inductive coupling between two coils, the inductivities of coils and mutual inductivity have to be taken into account, so that the impedances of the total devices are matched to achieve the lowest energy loss during the conversion of electrical to mechanical energy and vice versa. The equivalent

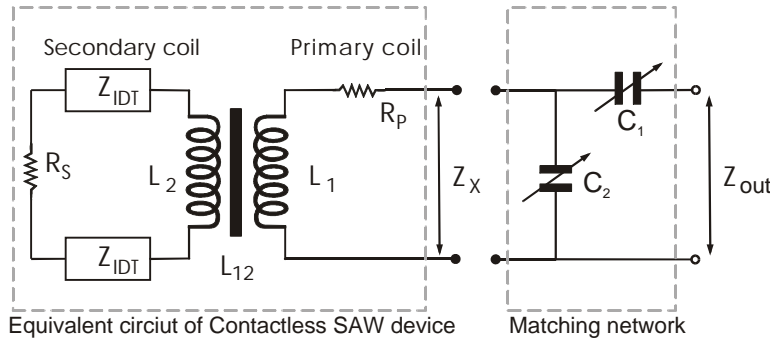


**Fig. 4-7**  
Equivalent circuit of the inductively coupled SAW sensor and its impedance matching network.  $C_1$  and  $C_2$  are tunable capacitors by which the total output impedance of the system  $Z_{out}$  can be matched with 50  $\Omega$ .

circuit for contactless device  $Z_X$  is shown in Fig. 4-7. The Primary and secondary coil form a transformer. The impedances of two IDTs  $Z_{IDT}$  are in series with the ohmic resistance and inductance of the secondary coil  $L_2$  and  $R_s$ , respectively, while the resistance of the primary coil  $R_p$  is also in series with inductance  $L_1$ .  $L_{12}$  is the mutual inductance. The total impedance of the SAW device is then given by

$$Z_X = R_p + i\omega L_1 + \frac{(\omega L_{12})^2}{i\omega L_2 + R_s + 2 \cdot Z_{IDT}} \quad (4-6)$$

The resulting total impedance  $Z_X$  may not match the impedance of the RF-electronics, thus, a matching network is needed to adjust the impedance of the contactless SAW device. This can be done by putting two variable capacitors  $C_1$  and  $C_2$  in series and parallel with the SAW device, respectively. The total impedance after impedance matching is

$$Z_{out} = \frac{1}{i\omega C_1} + \frac{1}{i\omega C_2 + (1/Z_X)} \quad (4-7)$$

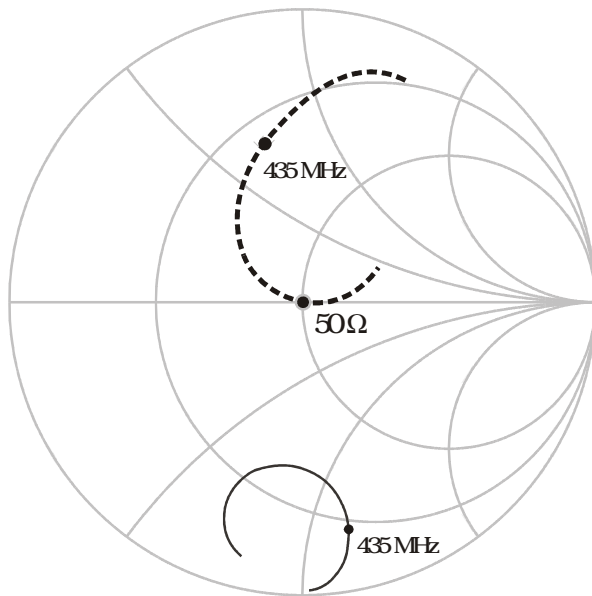


**Fig. 4-8** Impedance matching on a smith chart. The solid line is the unmatched impedance curve of SAW sensor. After matching, the impedance curve (dashed line) will pass through the center of the smith chart (50  $\Omega$ ). The frequency at the center is the optimal operating frequency for the sensor.

With proper trimming of  $C_1$  and  $C_2$ , the total impedance  $Z$  can be tuned to 50  $\Omega$ . Fig. 4-8 shows an example of impedance matching on a smith chart. The solid curve is the impedance of a 36° rot YX-LiTaO<sub>3</sub> contactless SAW sensor operating at a center frequency of 435 MHz and a span of 30 MHz without impedance matching. After impedance matching by using  $C_1 = 2.86$  pF and  $C_2 = 3.37$  pF, the impedance curve (dashed line) has been shifted to meet the center of the smith chart (the 50  $\Omega$  point). It should be noted that at the position of 50  $\Omega$  the frequency is 421.84 MHz, which is not the original center frequency of the given IDT configuration.

### 4.2.3 Fabrication of SAW sensor

Table 4-1 lists parameters of one of the IDT design for the inductively coupled SAW sensor which was the most commonly used in our laboratory. With the computer simulation software developed by [Beck 1999] and [Hoffmann 1999], the impedance of such IDT structure can be calculated to find the best matching network. Then, a mask with IDT patterns is required for mass fabrication of SAW sensors. This can be done by laser lithography. The mask consists of a color center glass substrate where one of the faces is doped with color centers. These normally absorb light very strongly, but can be bleached by illumination with a focused laser beam. In order to make a useful mask, the IDT structure patterns was first constructed by a CAD program and then transferred into a special format which can be read by the laser lithography instrument of our institute [Wagner 1998].

Table 4-1 The parameters of the IDTs in this work.

Substrate	SAW Frequency [MHz]	SAW wavelength [mm]	Finger overlap [mm]	Finger pairs	Delay line [mm]
36°rot YX-LiTaO <sub>3</sub>	430 MHz	9.6	700	30	3.5

The SAW sensor can then be mass fabricated using the mask and a LiTaO<sub>3</sub> wafer, on which a thin photo resist layer has already been deposited [Fig.4-9]. After UV-light exposure, the exposed photo resist was washed out by developer. Metallization is

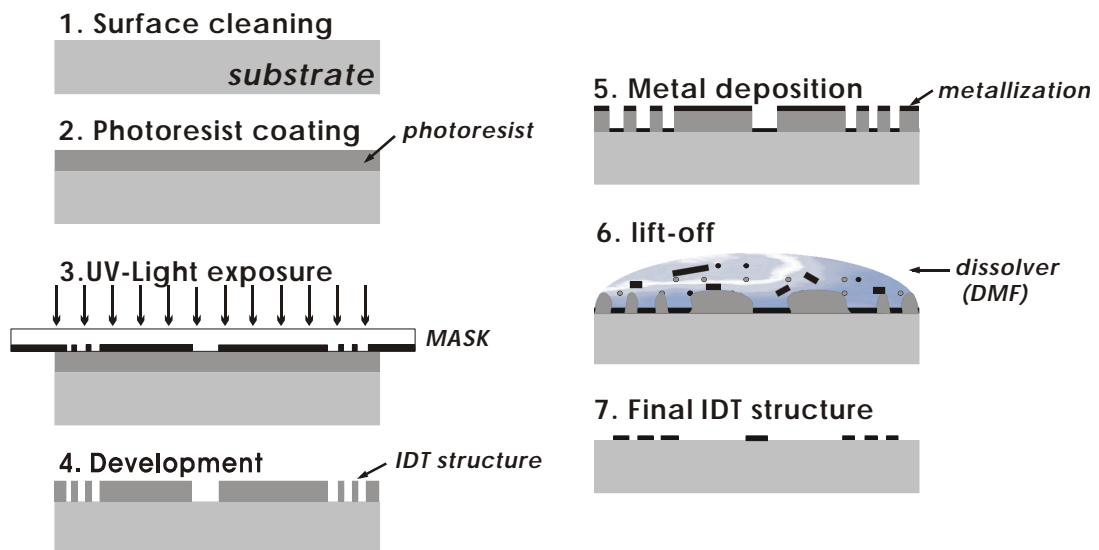


Fig.4-9 Fabrication of a SAW sensor. The IDT structures are deposited on a LiTaO<sub>3</sub> wafer by UV- light lithography techniques and lift-off processes.

done by sputtering a 5 nm Chromium adhesion layer followed by 100 nm gold. The wafer with the metallized IDT structure was then put into the DMF (DiMethylFormamide) solvent for lifting off the residue of photo resist and metal. In order to protect the IDT structure from aggressive solution when applying to liquid sensing, a thin SiO<sub>2</sub> layer of 1 μm was sputtered onto the surface of the wafer to form a coating on the IDTs. All the above processes were done in the clean room of our institute.

#### 4.2.4 SiO<sub>2</sub> coating as waveguide

Besides protection, another advantage of a thin SiO<sub>2</sub> coating is that it can act as waveguide for the Love wave sensor. Although 36° rot YX-LiTaO<sub>3</sub> can support a shear horizontal leaky surface wave even without any waveguide, the acoustic energy is not well localized at the surface. Computer simulation [Gentes 1994] shows that when SiO<sub>2</sub> is coated on lithium tantalate, the penetration depth of the wave will be reduced [Fig.4-10(a)]. Furthermore, the acoustic wave velocity decreases with increasing SiO<sub>2</sub> thickness [Fig.4-10(b)]. This is because the acoustic velocity in the SiO<sub>2</sub> layer is less than in LiTaO<sub>3</sub>. Since the acoustic wave is partially guided in the SiO<sub>2</sub> layer, the acoustic velocity will decrease when the localization of the wave in the SiO<sub>2</sub> layer increases.

Fig.4-10(c) indicates the normalized velocity change between free- and metallized surface when the substrate is coated with SiO<sub>2</sub>. The velocity change decreases with the increasing thickness of SiO<sub>2</sub>. It should be noted that when the thickness of SiO<sub>2</sub> is thicker than about 0.7λ, there is almost no difference between free and metallized surface in velocity. This implies that for larger thickness the effect of the SiO<sub>2</sub> layer is equivalent to a metallization, i.e. the SiO<sub>2</sub> layer provides shielding from surface conductivity as long as it is thick enough even without metallized surface. This can strongly reduced the contribution of liquid conductivity while performing liquid sensing. This is also shown in the computer simulation below. In Fig.4-10(d), the SH-mode has maximal amplitude when the thickness is near 0.1λ, while the amplitudes of the longitudinal and the vertical modes are nearly minimal. Therefore, the optimal thickness of SiO<sub>2</sub> layer is about one tenth of the SAW wavelength. When liquid sensing is performed, the influences of liquid conductivity and dielectricity have to be considered.

As described above, a SiO<sub>2</sub> layer provides a good shielding. The results of the simulation using the finite element software “Quick Field” are shown in Fig.4-11. When there is nothing but air above the SiO<sub>2</sub> layer, the electric fields generated by the IDTs can penetrate through the coating into the air. On the contrary, the electric fields are concentrated in the thin SiO<sub>2</sub> layer and LiTaO<sub>3</sub> substrate to a large extent while the surface is loaded with water. Thus, the influences of dielectric and conductive properties of loaded liquid can be shielded by the SiO<sub>2</sub> layer.

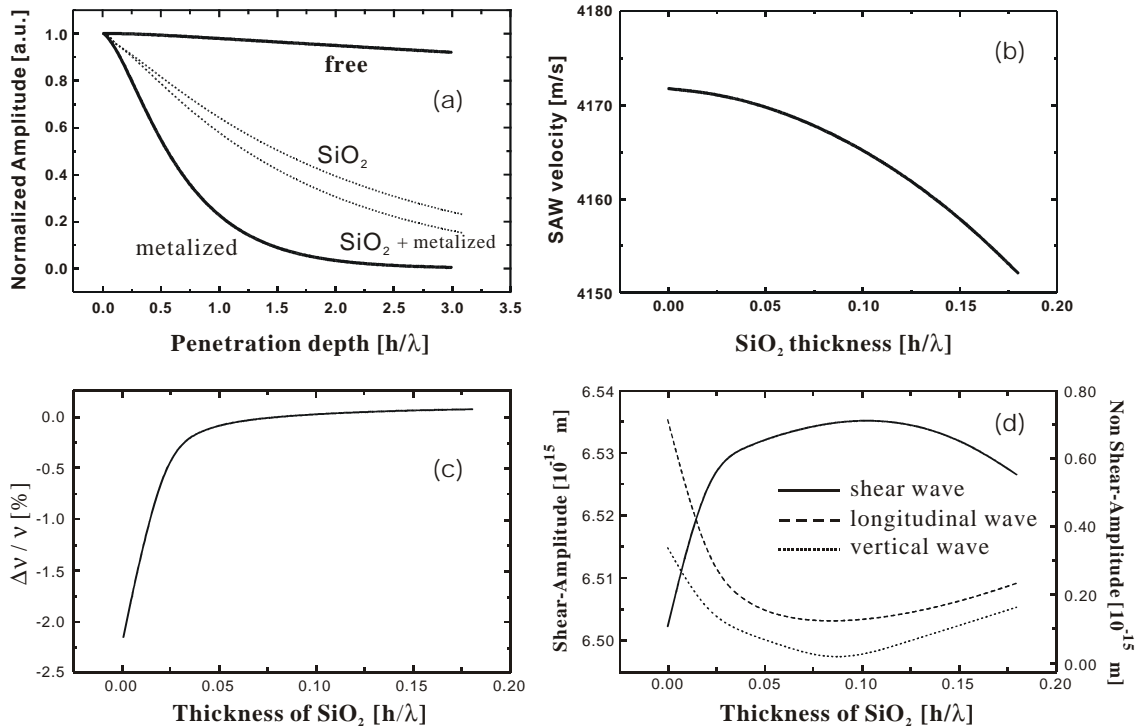


Fig.4-10 (a) Normalized amplitude of surface waves with different coatings on LiTaO<sub>3</sub>. The wave can be well localized near the surface when propagating at metallised and SiO<sub>2</sub> coated surface. (b) The wave velocity decreases with the increase of SiO<sub>2</sub> thickness. (c) Normalized SAW velocity difference against the thickness of SiO<sub>2</sub> layer between free- and metallised surface. It shows that when the SiO<sub>2</sub> layer is thick, the differences between free- and metallised surface are very limited. (d) The amplitudes of SH-wave and non-shear waves. The optimal thickness of SiO<sub>2</sub> waveguide is chosen where the amplitudes of non SH-waves are minimal.

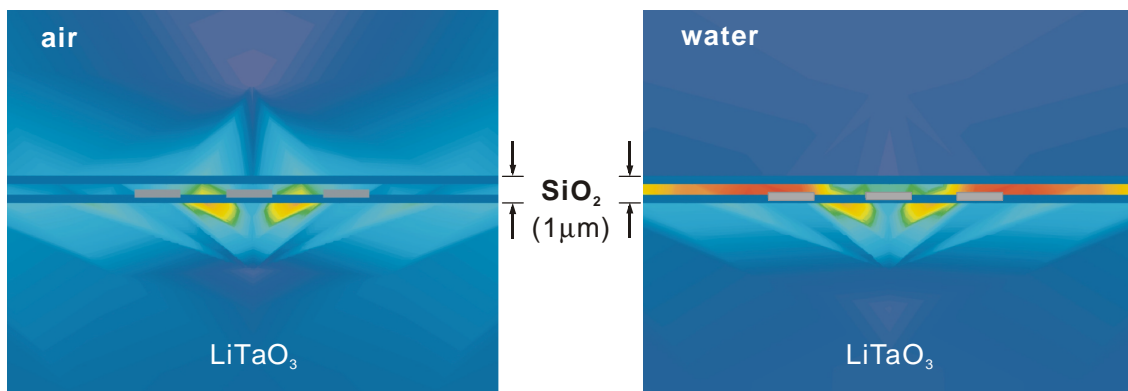


Fig.4-11 Computer simulations show that if the SiO<sub>2</sub> coated SAW sensor is loaded with water, most of the electric fields in the water is suppressed, unlike the case of exposing in the air. The fields are concentrated in the SiO<sub>2</sub> layer. The gray parts are IDT fingers and the red color represents strong field regions and the blue color means weak field regions. The SiO<sub>2</sub> layer prevents the surface waves from the influences of surface conductivity and dielectricity from the water solution.

### 4.2.5 Measurement setup

The complete setup is shown in Fig.4-12. The SAW sensor lies on an insulating plate of boron nitride, in which the primary coil is located. The plate is then housed in a brass socket, both of them have good heat conductivities. Under the socket is a Peltier element followed by a heat sink, which is regulated by an “Eurotherm” temperature controller. The RF-signals are generated by a network analyser which also receives the reflected RF-signals. Between the network analyser and the primary coil is the impedance matching network. All of the instruments and data are processed by a personal computer through a GBIP interface.

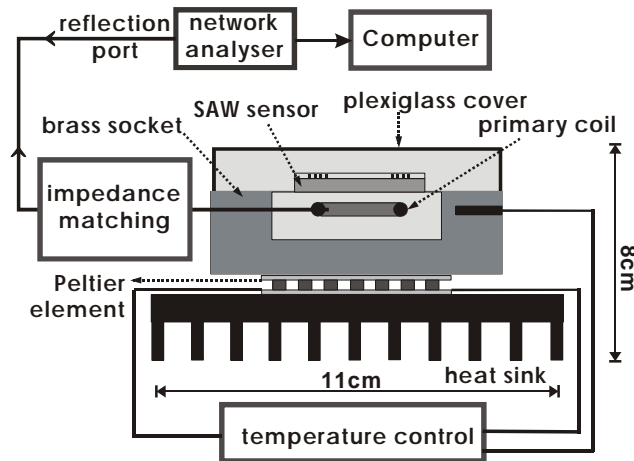


Fig. 4-12 Complete setup of a SAW immunosensor.

## 4.3 Measurements using SAW immunosensor

### 4.3.1 Principle of measurement

A series of RF-signals is sent from the network analyser to the SAW sensor. The reflected signals are also received by the network analyser and their relative amplitudes are measured in unit of decibel [dB] relative to the input signals. The original frequency response near the center frequency of the SAW sensor shows a strong interference pattern [Fig.4-13(a)]. The network analyser converts these data from the frequency-domain into the time-domain through Fourier transformation [Fig.4-13(b)]. With the “Gate” function,

only the useful signal will be selected, i.e. the crosstalk signals which appears before and all other reflected signals which appear later than the delay time ( $\tau$ ) will be filtered out.  $\tau$  is the period that acoustic waves need to travel across the delay line between input and output IDTs. With the “gating” sequence, the frequency response now presents a broad and smooth curve [Fig.4-13(c)]. The frequency at which the maximum of the relative amplitude arises is exactly the operating frequency of the SAW sensor.

Although the relative amplitude of the surface wave can be measured by the network analyser, but this quantity is not used for sensing purposes. Therefore, only quantities which relate to the wave velocity are of interest. In the case of the inductively coupled SAW sensor with network analyser, the frequency is held constant; thus, the phase of the surface wave is equivalent to the wave velocity: It is assumed that the delay line has a length of  $l$ , hence, the phase  $j$  refers to the number of waves located in the delay line:

$$j = w \cdot t = w \cdot \frac{l}{u} \Rightarrow \Delta j = w \cdot \frac{l}{u^2} \Delta u \Rightarrow \left| \frac{\Delta j}{j} \right| = \left| \frac{\Delta u}{u} \right| \quad (4-8)$$

where  $t$  is delay time of the device. Therefore, it is demonstrated that the phase change of

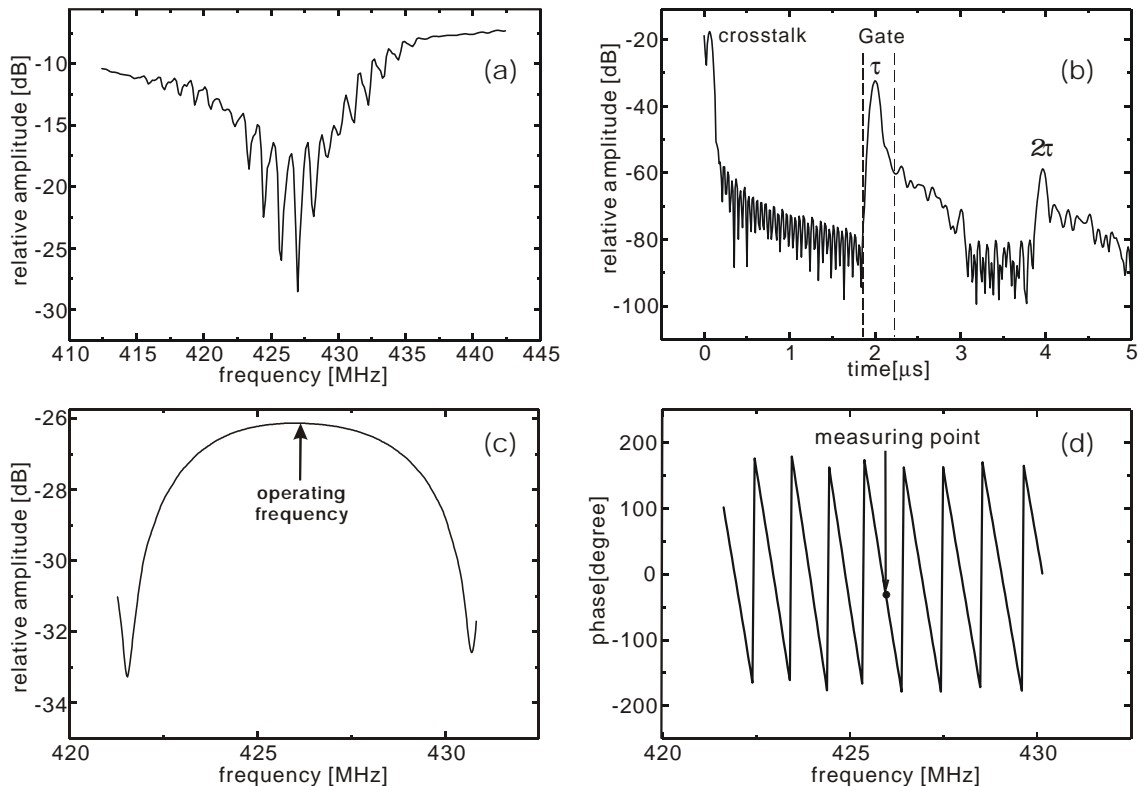
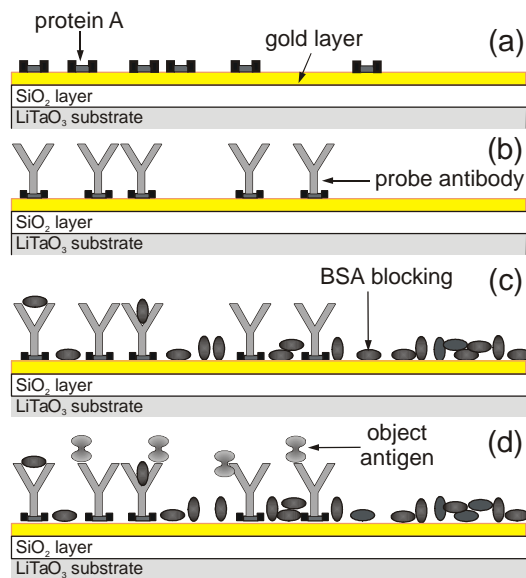


Fig. 4-13 (a) Spectrum of the frequency response of a SAW device. The impedance of the device has matched to 50  $\Omega$ . (b) The same response in the time domain. The second peak appears at the time  $t$ , delay time of the device. By using the “gate” function, other signals are filtered out. (c) The “gated” response in the frequency domain. The frequency at which the relative amplitude is maximal is the best operating frequency for the SAW sensor. (d) Phase spectrum in the frequency-domain. The phase change is equivalent to the velocity change when the device operates at constant frequency.

the surface wave at constant frequency also means the change in wave velocity. The measurement of phase change can also be performed by the network analyser [Fig.4-13(d)].

### 4.3.2 Surface modification

The thin  $\text{SiO}_2$  layer which covers the sensor surface provides both good mechanical and electrical characteristics to serve the propagation of surface wave. But unfortunately,  $\text{SiO}_2$  is not that biocompatible, i.e. it lacks the affinity to biomolecules. Since our SAW sensor functions as a microbalance owing to its high sensitivity to the mass change on the surface, the surface affinity to biomolecules is significant for the development of an efficient biosensor. To overcome the poor bio-affinity of  $\text{SiO}_2$ , the surface must be modified. In this work, the object of the SAW sensors is associated with the immunoglobulin, therefore, immobilization of antibodies on the  $\text{SiO}_2$  surface is the main task and a medium that connects with the antibody molecule and the surface is required.



*Fig.4-14 Surface modification with protein A and BSA blocking. Antibodies will immobilized with their binding sites ( $F_{ab}$  fraction) upwards, when they bind with protein A by the  $F_c$  fractions. BSA are used for blocking the unbound surface to prevent non-specific binding.*

Additionally, protein A can bind strongly with the gold surface through Van der Waals forces [Horisberger 1984] and Thiol-bonds [Yang 93]. With the two advantages of protein A, the probe antibodies can be specifically immobilized on the SAW sensor, as

Many methods for antibody immobilizing on solid surface have been presented in the literatures, such as covalent binding methods, physical attachment, polymer embedding...etc. The method used here is the immobilization using “protein A”.

Protein A (molecular weight 42000) is a major cell wall component of most strains of *Staphylococcus aureus* [Harlow 1988]. The main feature of protein A is its extraordinary affinity for immunoglobulin, especially class G (IgG). Protein A has binding sites for the Fc fragment of mammalian IgG, notably IgGs from human, mouse, cat, dog, guinea pig and rabbit. Owing to the highly specific binding orientation between protein A and IgG, the active sites of an antibody, the  $F(ab')_2$  fragment, will not lose their binding abilities to object antigens.

long as a thin gold layer is deposited on the sensor surface. After the purification of the gold surface by Piranha acid (a 3:1 mixture of 95% sulfuric acid and hydrogen peroxide), a specific sensing surface with probe antibodies on the SAW sensor is prepared with the following protocol [Fig.4-14]:

1. Incubation of Protein A: pipet 10  $\mu\text{l}$  protein A solution (500  $\mu\text{g}/\text{ml}$ ) on the gold surface for 1 hour.
2. Cleaning process: wash out the residue of protein A solution with 0.01M PBS (phosphate buffered saline). Wash the surface again with distilled water, blow off the water with compressed nitrogen to dry the surface.
3. Incubation of Antibody: pipet 10  $\mu\text{l}$  solution of probe antibody on the gold surface for 1 hour.
4. Cleaning process again to wash out the unbound antibodies.
5. Blocking process: block the unoccupied positions on the gold surface with BSA solution (bovine serum albumin, 30  $\text{mg}/\text{ml}$ ) for 30 minutes, in order to avoid non-specific binding between object antigen and gold surface.
6. Cleaning process again to move out all weakly bound proteins.

Now the SAW sensor is ready for experiment since the sensing area is already specifically activated by the above incubation process. After each measurement, the sensor can be recycled again by removing all the biomolecules with the Piranha acid and the same cleaning process listed above, until the gold layer is damaged.

### 4.3.3 Results

Fig.4-15 shows the phase and relative amplitude behavior of a surface wave regarding to different object antigens using an inductively coupled SAW immunosensor. The operating frequency is 425 MHz at 25°C. Before the measurement, the surface was already prepared with immobilized anti-goat IgG (from rabbit). When the experiment started, the sensor surface was loaded with 5 $\mu\text{l}$  buffer solution (PBS). At 80 seconds, 5  $\mu\text{l}$  of goat anti-human IgG was pipetted on the sensing area of the SAW sensor. This step caused obvious changes in both phase and relative amplitude since the goat IgG and the anti-goat IgG were bound specifically, resulting in an appreciable mass change on the sensor surface. Therefore, the wave velocity becomes slower. The relative amplitude was also measured but so far there is no appropriated interpretation for it. At 300 seconds, 5 $\mu\text{l}$  of non-specific antibody (rabbit anti-human IgG) was added to the sensing surface, but did not result in a notable change in phase since the non-specific antibody did not bind with

the antibodies on the sensor surface.

To confirm this result, specific antibodies were added again at the 380 seconds and 470 seconds, the changes in both quantities of the SAW sensor appeared again, demonstrating a high selectivity for distinguishing between specific and non-specific antibodies.

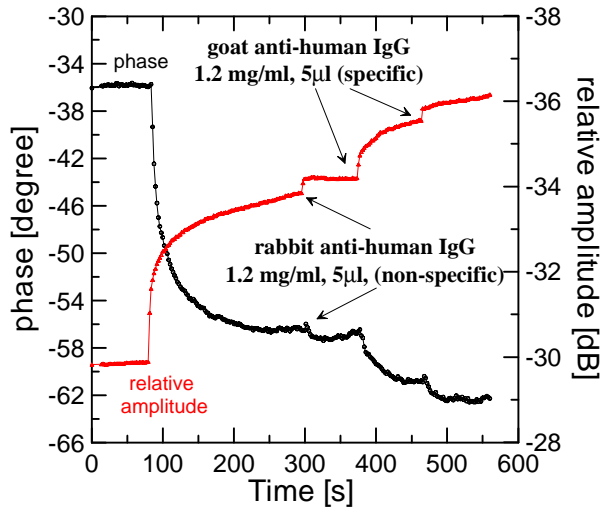


*Fig.4-15 Sensor responses of an antibody-antigen reaction. The specific antigen caused a great phase shift at 100 seconds. But the non-specific antigen did not result in a notable change in phase.*

*The phase shift decrease further when specific antigens were added again.*

*It should be noted that the origin of the scale for relative amplitude is at the bottom, and the quantities decreases upwards.*

Another test was done by increasing the concentration of probe antibody while the immobilization process was carried out. Anti-goat IgG (from rabbit) solution of 2.5 mg/ml, which is two times higher than that before, was incubated on the gold surface. With this high concentration of probe antibody on the surface, more object antigens may be

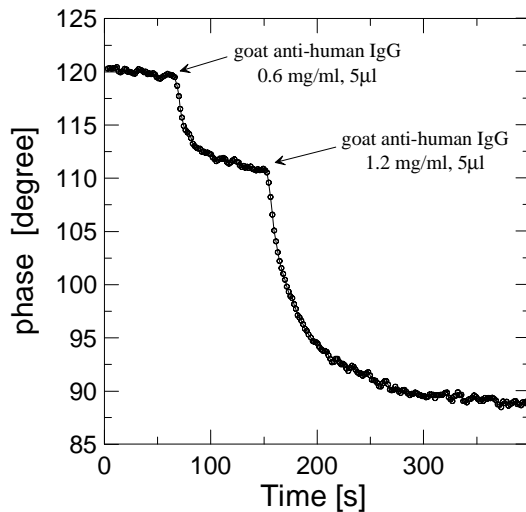


*Fig.4-16 The measurement was done by the sensor modified with very high concentration of the probe antibody, resulting in a maximal phase change of 30 degree.*

captured on the sensor surface. Fig.4-16 shows the result: while the 5µl specific goat anti-human IgG solution with of concentration 0.6 mg/ml was first added on the surface at 60 seconds, the phase change is about 10 degrees. At 150 seconds, the same antibody but with higher concentration was added again onto the sensor, the phase change reached an additional 20 degrees. Totally, phase change of 30 degrees was obtained. Comparing this result with the previous measurement, the net changes in phase are not much different. Therefore it can be concluded that the maximal phase change

is about 30 degrees when the sensor surface is saturated with object antigens.

Fig.4-17 shows a sensor response after a dilute antigen solution was pipetted on to the sensor. The total phase shift is about 3.5 degrees, accompanying with a noise level of 0.5 degrees. According to the equation (3-73), in this case the mass change per unit area  $D m_{min}$  detectable by the SAW sensor is  $21 \text{ pg} / \text{mm}^2$ . The noise corresponds to a mass change per unit area of  $3 \text{ pg} / \text{mm}^2$ , which is only one seventh of the minimal detectable mass change. The noise is not electronic noise but may result from the inhomogeneous temperature distribution on the sensor surface, although it was controlled by the

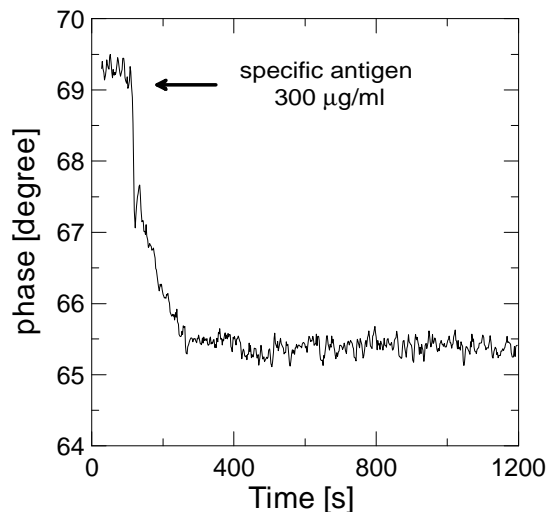
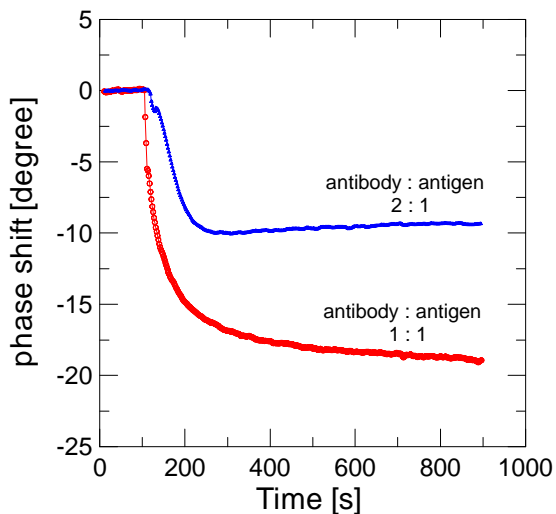


Fig.4-17 Noise level of a SAW device must be quite small than the main response. This measurement shows a noise level which is only one seventh the main response.

temperature regulator.

The maximal phase change occurs when the sensing surface is totally filled with captured object antigens in the case of the modified sensor surface. It is also interesting to observe what happens if the surface modification has not been done? A series of measurements using SAW sensors without surface modification was done to answer the question. The results are shown in Fig.4-17. The procedure was that at the beginning the solution of probe antibodies was placed on the sensor surface; since the antibodies did hardly bind with  $\text{SiO}_2$ , they stayed suspended in the liquid. When specific antigens were pipetted onto the sensor surface, and reacted with the probe antibody, the antibody-antigen complexes deposited on the sensor surface and resulted in a mass change which affected the SAW behavior. As



shown in Fig.4-18, the maximal phase change happens always only when the concentrations of antibody and antigens are comparable. Moreover, the total phase change is less than that obtained by the surface modification.

Fig. 4-18 Measurements without surface modification. The maximal phase shift happens when the concentrations of the probe antibody and target antigen are the same.

The larger the difference in concentration between antibody and antigen, the less phase change will be obtained. This conclusion is identical to the result from immunoprecipitation [Roitt 1996].

#### 4.3.4 Polymethyl methacrylate (PMMA) coating

Another method of surface modification was tested preliminarily. Instead of  $\text{SiO}_2$ , polymethyl methacrylate (PMMA) is deposited on the sensor surface as waveguide by spin-coating. PMMA is dissolved in 2-ethoxyethyl acetate to form a PMMA solution with 5% concentration. After coating, the sensors were baked at  $180^\circ\text{C}$  for 2 hours. The final thickness of the PMMA layer was 500 nm.

The antibody molecules can adsorb on the PMMA layer by physical attachment, not by the covalent binding. Hence, the binding strength and orientation of the antibody molecules is not as perfect as on a surface modified using protein A and gold layer. However, the advantage of PMMA is that it can be dissolved easily by organic solutions; therefore, the preparation of a PMMA layer and the cleaning process after each experiment can be simplified. Fig.4-19 shows the experimented result by a SAW sensor with PMMA waveguide. The responses of the sensor indicates a high specificity. The phase of the surface wave reacted only to the specific antibodies and almost no response to non-specific antibodies was obtained, implying that only the mass change on the sensor surface will be detected.

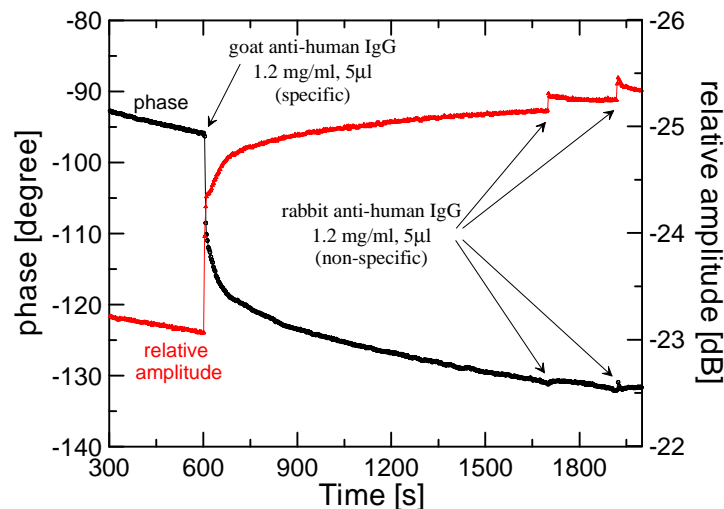


Fig. 4-19 Response of antibody-antigen reactions with PMMA-modified SAW sensor. 500 nm PMMA layer was coated on the surface for immobilizing the probe antibodies. The results indicates a high specificity.

# Chapter 5

## Theory of Capacitively Coupled Electrochemical Sensors

Apart from the surface acoustic wave sensor which is sensitive to the mass variation on the sensor surface, electrochemical sensing systems, however, are also convenient for the detection of biomolecules. The electrical properties of the surface, such as conductance and capacitance, will be modified by the interaction of biomolecules. Hence many electrochemical immunoassays have been developed based on these electrical phenomena [Warsinke 2000]. In this chapter, principles of the capacitively coupled electrochemical biosensor will be introduced.

### 5.1 Electrical model for bare electrode

The simplest version of electrical sensing is the two-probe conductive detector, which consists of two separated parallel plate electrodes with sample liquid between them [Fig.5-1(a)]. An alternating voltage with constant amplitude is applied to the electrodes, and the resulting current is measured. The impedance of the sample liquid is then given by

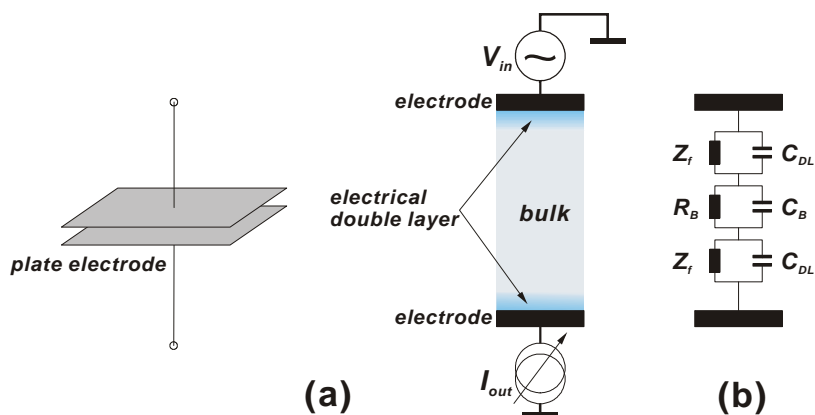


Fig.5-1 Scheme of (a) a 2-probe sensor with parallel plate electrodes, and (b) its equivalent electrical circuit.

the ratio of the applied voltage and the measured current. Generally, the electrical equivalent circuit for bare electrodes is shown in Fig.5-1(b), where  $R_B$  is the uncompensated ohmic resistance of the bulk solution, and  $C_B$  is the capacitance of the bulk solution. If the double layer capacitance  $C_{DL}$  formed at the solution-electrode interface is not taken into account, the bulk capacitance between two parallel bare plate electrodes is:

$$C_B = \epsilon \epsilon_0 \frac{A}{d} \quad (5-1)$$

where  $\epsilon_0 = 8.85 \times 10^{-12}$  [C/Vm] is the permittivity of the free space,  $\epsilon$  is the relative dielectric constant of the electrolyte solution,  $A$  is the area of the electrode,  $d$  is the separation of the electrodes. Since the reactance of the bulk capacitance  $X_B = 1 / (i\omega C_B)$  is much higher than the bulk resistance  $R_B$ , the total impedance of the bulk solution is dominated by the bulk resistance  $R_B$ .

In order to maintain the electrical neutrality at the liquid-electrode interface, the ions in the liquid will redistribute to form a layer of charges which opposite to the charges on the electrode. Hence, these two layers at the electrode-electrolyte interface are termed electrical double layer [Bagotzky 1993], which is analogous to the electrical capacitance. Any chemical or physical reactions happening at the interface may not only change the electrical properties of the bulk solution, but also disturb the stability and formation of the double layer, inducing a deviation in the measured current.

Besides double layer, the faradaic current will also change the surface characteristics. For example, the catalysis at the electrodes by enzymes results in a faradaic current; then the contribution of faradic impedance  $Z_f$  must be taken into account. The faradic impedance and the double layer capacitance are connected in parallel and form the double layer impedance, which is in series with the bulk resistance  $R_B$ . Therefore, if the voltage applied to the electrodes is low enough to prevent the oxidation-reduction reaction at the electrodes, the faradic impedance can be ignored.

## 5.2 Electrical model for insulated electrodes

The applied voltage on the bare electrode may stimulate the interaction between electrolyte and electrodes, such as the oxidation-reduction reaction, and give rise to

- (a) formation of gas bubbles at the electrolyte-electrode interface and
- (b) corrosion of the electrodes.

In order to protect the electrodes from damage and the measurement from read-out errors, an insulating coating for the electrodes is required. Metallic oxide, silicide, and polymer are popular materials for insulating coating. The electrical model for the

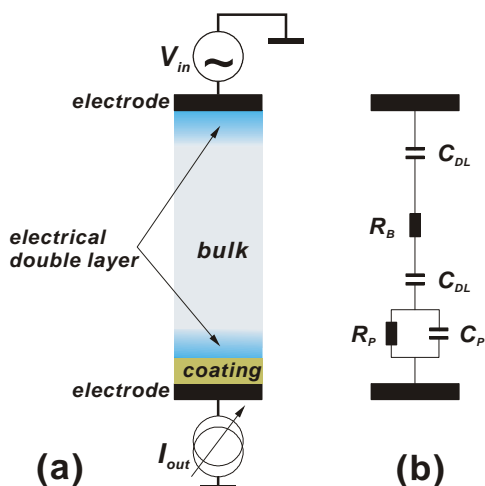


Fig.5-2 Scheme of the (a) electrical sensing system coated with insulating layer on the lower electrode, and (b) the equivalent circuit, where the bulk capacitance and faradic impedance are disregarded. The resistance of insulator  $R_p$  can also be neglected due to its infinity for a ideal insulator.

insulating layer is given by a parallel connected resistance  $R_p$  and capacitance  $C_p$  of the insulator. It is well known that the resistance of an ideal insulator  $R_p$  is infinity; hence, the equivalent circuit for the insulating layer can be simplified by a pure capacitor  $C_p$ . If only the lower electrode is coated with insulator, an electrical double layer will still arise at the insulator-electrolyte interface, [Bousse 1993]. Therefore, the insulating capacitance  $C_p$  can be seen as connected in series with the double layer capacitor  $C_{DL}$  in series [Fig.5-2].

If the sensor will operate in the high frequency range, a low capacitance of the insulating coating  $C_p$  is acceptable. But if the sensor will be used at low frequency, then a high  $C_p$  is necessary, i.e. high permittivity and thinner materials are preferred for applications at low frequencies. However, the drawback of a high capacity insulating layer is that: An unfavorable effect of the electrical double layer is unavoidable when the unknown double layer capacitance is smaller than that from the insulating layer. Since the bulk capacitance, the faradic impedance at the interface, and resistance of the insulating layer are disregarded, the total impedance of the system is approximately given by <sup>(\*)</sup>

$$Z_{total} \approx \left( R_B + \frac{2}{i\omega C_{DL}} + \frac{1}{i\omega C_p} \right) \quad (5-2)$$

### 5.3 Sensitivity of capacitively coupled sensors

Consider again that only the lower electrode is coated with insulator, and the double layer capacitance and liquid resistance remain constant. If probe antibodies have been immobilized homogeneously on the insulating layer of the lower electrode, the antibody layer can be seen as a capacitor in series with the capacitive insulating layer. Let the equivalent capacitance of these two capacitors in series be the background capacitance  $C_0$ . If the specific antigens are captured by immobilized antibodies, antigen-antibody

\* Here it is assumed that the double layer capacitances are approximately the same, either at the electrode surface or at the insulator interface.

complexes will deposit on the sensor surface, resulting an increase in total thickness of the biomolecular layer at the device surface. This implies that the electrical properties of the liquid-solid interface will be changed, if specific antigen-antibody reaction occurs. At liquid-solid interface, the capacitance change due to the specific immunoreaction is termed as  $\Delta C = C_{AG}$  [Fig.5-3]. As a result, the total capacitance at the liquid-solid interface  $C_{total}$  after the immunoreaction is [Gebbert 1992]:

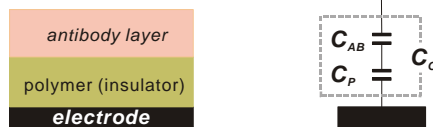
$$C_{total} = \frac{C_O \cdot \Delta C}{C_O + \Delta C} = \frac{C_O \cdot C_{AG}}{C_O + C_{AG}} \quad (5-3)$$

Here it is assumed that the bulk resistance  $R_B$  and the double layer capacitance  $C_{DL}$  of the solution do not change, and the equilibrium is established after the immunoreaction. Thus, the sensitivity of the sensor is the ratio of the change of total capacitance and the  $C_{AG}$ ,

$$sensitivity \equiv \left( \frac{\partial C_{total}}{\partial C_{AG}} \right)_{C_O} = \frac{C_O^2}{(C_O + \Delta C)^2} = \frac{C_O^2}{(C_O + C_{AG})^2} \quad (5-4)$$

From the above equation, it is clear that the sensitivity of the sensor approaches unity if the  $C_O$  is much greater than  $C_{AG}$ , i.e. the capacitance formed by the insulating layer and the immobilized probe antibodies must be as large as possible to get a large output signal. Since the dielectric constants of biomolecules are limited, therefore, a thinner layer composed of high permittivity materials are the most important factor related to the

(a)



(b)

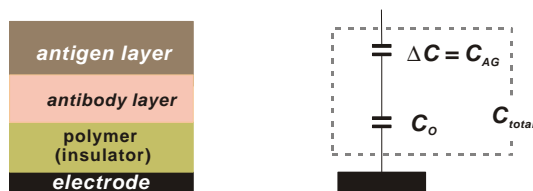


Fig.5-3 Scheme of (a) The electrode is covered with insulator and immobilized antibodies. The equivalent capacitance of these layers is  $C_O$  (background capacitance).

(b) After the specific antibody-antigen reaction, the total thickness of the coatings increases since the antibody-antigen complexes deposit on the sensor surface.  $C_{AG}$  denotes the capacitance change due to specific immunoreaction.

posed of high permittivity materials are the most important factor related to the sensitivity of capacitively coupled electrochemical biosensor since the background capacitance  $C_O$  will be great.

The discussion above is based on the fact that the antigen layer covers the surface homogeneously without vacancy. The vacancy may be caused by the defects or non-specific antigens which do not bind with the probe antibodies. Fig. 5-4 indicates the difference between an ideal electrode and practical electrode in a buffer solution.

Obviously, in Fig.5-4(a), when the whole surface is covered by the specific antigens, the layer of the antigens can be seen as a perfect capacitor  $C_{AG}$  in series with the background capacitance  $C_O$ . As indicated in equation (5-4),  $C_O$  should be much larger than the  $C_{AG}$  to yield the

maximal sensitivity. If some area of the active sites provided by the probe antibodies are vacancy or occupied by unknown molecules, then the contribution from the specific antigen layer will be decrease since the effective binding area will be reduced. According to equation (5-3), the increasing  $DC$  results in an increase in total capacitance  $C_{total}$ , and degrades the sensor sensitivity [equation (5-4)]. It should be noted that since the antibody and antigen prepared for the measurements are immunoglobulins, therefore, they should have similar electrical properties and size. When an antigen layer is attached to the antibody layer homogenously, the resulting capacitance  $C_{AG}$  should be the same as the antibody layer  $C_{AB}$ , resulting in a total capacitance half the capacitance of antibody layer  $C_{AB}$ . If the surface capacitance is dominated by the antibody layer, then the maximal sensitivity will be 25%, and a maximal 50% change in impedance even the surface are coated with antigen layer since the antigen layer is as thick as the antibody layer. Moreover, vacancy due to defects from antigen, probe antibody layer, or even from the insulating coating, may have a negative contribution to the capacitive measurement. These will be discussed in chapter 7.

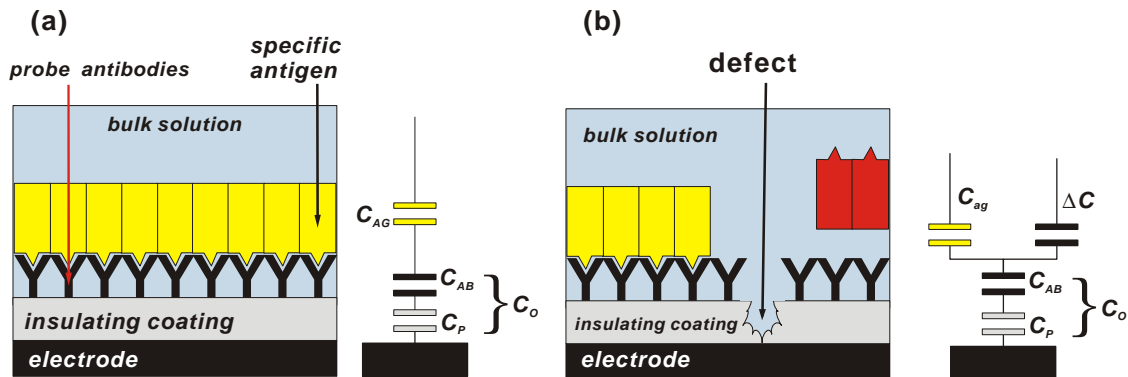


Fig.5-4 (a) Ideal specific binding results a perfect capacitive layer  $C_{AG}$ . (b) The vacancy due to defects or non-specific antigens which do not bind with probe antibody, will degrades the effective area of specific binding and increases the net capacitance of the detecting interface.



# Chapter 6

## Design of Capacitively Coupled Electrochemical Sensors

### 6.1 Two-probe Sensor

#### 6.1.1 Design and production of the electrode

As shown in Fig.6-1, two rectangular gold electrodes were arranged parallel on a glass slide. This pair of electrodes is 100  $\mu\text{m}$  in length and 30  $\mu\text{m}$  in width separated by a distance of 40  $\mu\text{m}$ . The production process is the same as for the surface acoustic wave sensor, only the substrate is glass instead of a lithium tantalite wafer. After the

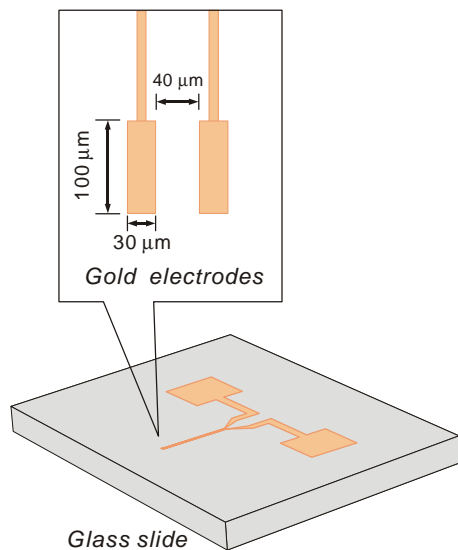


*Fig.6-1 The two-probe electrical sensor with thin 100 nm gold electrodes on the glass slide of 1 mm in thickness.*

UV-lithography and the development process in the clean room, 5 nm chromium was first sputtered on the glass slide for adhesion layer of gold and glass. Afterwards, 100 nm of gold was sputtered onto the chromium layer, followed by coating with polymer as the insulating layer.

#### 6.1.2 Electrical Model

The electrical model for two planar electrodes is shown in Fig.6-2.  $d_{AB}$  is the thickness of the bilayer due to the immobilized probe antibodies, and  $Dd$  is the thickness variation which is caused by specific binding of biomolecules, for example, the antigens. It should be noted that a constant voltage source is considered better than a

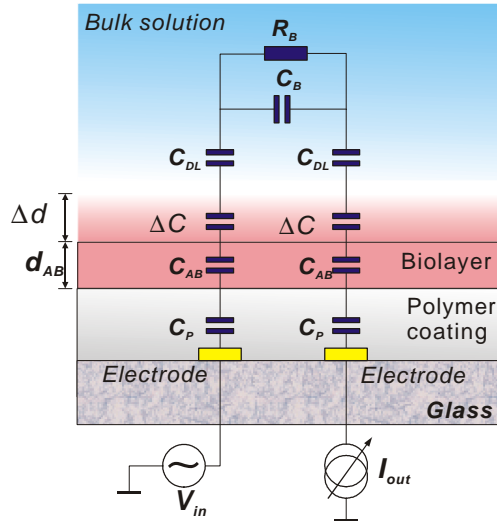


Fig.6-2 Scheme of electrical model of a two-probe sensor.  $\Delta d$  is the thickness change due to the specific immunoreaction

constant current source for this measurement; this will be discussed in the next section in detail. Since the insulating layer is dielectric, it can be treated as a plate capacitor  $C_P$  over the electrodes. The bulk electrolyte behaves as a conductor which can be represented by the bulk resistance  $R_B$  and bulk capacitance  $C_B$  in parallel. But as already discussed in chapter 5, the reactance of  $C_B$  is negligibly small; thus, only the bulk resistance dominates the total impedance of the bulk solution. After the specific immunoreaction, the antibody-antigen complexes will deposit on the surface of the sensor. Since the proteins are dielectric [Pethig 1987], this kind of physical precipitation of antibodies

and antigens will form a capacitive biolayer of thickness  $\Delta d$  attached to the sensor surface. An alternating input signal from the function generator with constant amplitude  $V_{in}$  at the electrode on the left hand side capacitively couples with the electrolyte solution, and continues to couple capacitively with the electrode on the right hand side again. Therefore, the output current  $I_{out}$  is strongly dependent on the total thickness  $d_{AB} + \Delta d$  of the biolayer and is given by

$$I_{out} = \frac{V_{in}}{Z_{total}} = V_{in} \left[ R_B + \left( \frac{2}{i\omega C_P} \right) + \left( \frac{2}{i\omega C_{AB}} \right) + \left( \frac{2}{i\omega C_{DL}} \right) + \left( \frac{2}{i\omega \Delta C} \right) \right]^{-1} \quad (6-1)$$

where  $Z_{total}$  is the total impedance of the system,  $\omega$  is the angular frequency of the applied voltage,  $C_P$ ,  $C_{AB}$ ,  $C_{DL}$ ,  $\Delta C$  are capacitance of the polymer coating, the layer of immobilized antibodies, the electrical double layer and the specific bound antigens, respectively.

### 6.1.3 Required Electronics

#### • Parasitic capacitance

The parasitic capacitance of the cables connecting the sensor to the read-out meters affects the accuracy of the electrical measurement. The magnitude of the parasitic capacitance depends on the length of the cable. A capacitance of about 100 pF is typical for a 1 meter long BNC cable. This parasitic capacitance will lead to a considerable

current leakage, if a constant current source is utilized for the capacitive electrical measurement, since the resulting impedance may be comparable to that of the sensor. To overcome this deficiency, shorter cables should be considered as lead wires to suppress the parasitic capacitance. However, the parasitic capacitance will still exist and cannot be completely eliminated.

An alternative solution is substituting a constant AC voltage source for the constant current source. Then the parasitic capacitance of the cable does not influence the imposed electrical potential at the electrode because both of them are connected in parallel [Fig.6-3(a)]. When a signal with constant amplitude  $V_{in}$  is applied to the first electrode, since the voltage is held constant, the resulting output current  $I_{out}$  represents the corresponding electrical conductive property of the system.

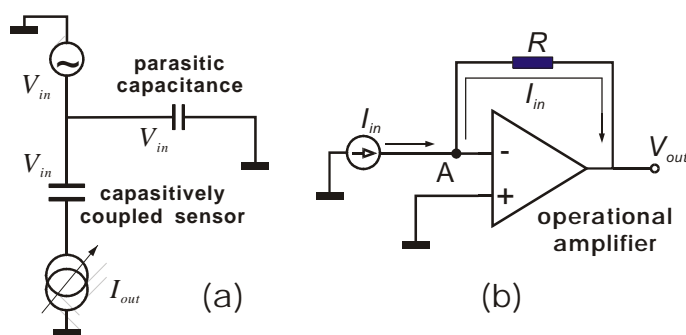


Fig. 6-3 (a) The constant voltage source for a capacitively coupled sensor can avoid the influence of parasitic capacitance from the lead wire since they are connected in parallel. The potential drop at the sensor electrode is the same as the voltage from the source  $V_{in}$ .

(b) Scheme of a transimpedance amplifier circuit.

### • Transimpedance Amplifier

Measurement of the current response of the two-electrode system was performed with a **transimpedance amplifier**, which consists of an operational amplifier in an inverting configuration and a feedback resistor  $R$  [Fig. 6-3(b)]. The input impedance of such an amplifier is lower than the output impedance of the sensor and the connecting cable, so the effect of parasitic capacitance can be minimized. A typical operational amplifier has an extremely high input impedance at both input terminals, so current does not flow into the amplifier. Thus, all input current flows through the feedback resistor  $R$ . Therefore, the input current  $I_{in}$  can be transformed into a voltage output  $V_{out}$  by the transimpedance amplifier with the relation  $V_{out} = G_{TA} I_{in}$ , whereas  $G_{TA}$  is the gain of this amplifier circuit. Hence, the transimpedance amplifier is also called a “*current-to-voltage converter*” (**I-V converter**).

Assuming that the operational amplifier in Fig.6-3(b) is ideal, while the non-inverting terminal (“+”) is grounding, the inverting input terminal (“-”) will be also at virtual ground, which means that the voltages at both inputs of the operational amplifier are zero. This non-inverting configuration can also minimize the effect of parasitic

capacitance owing to the fact that voltages at both inputs are virtually zero.

Applying **Kirchhoff first law** to node A at the inverting input, the summary of total current should be zero:  $I_{in} \cdot R + (V_{out} - 0) = 0$ . Thus, the output voltage  $V_{out} = -R \cdot I_{in}$  is read. The feedback resistance  $R$  determines the output voltage for a given input current in the circuit. For high sensitivity applications, extreme huge feedback resistances may be required. In such cases, any parasitic resistance coming from the surroundings, which is in

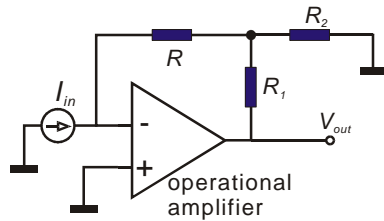


Fig.6-4 Improved transimpedance amplifier circuit with arbitrary high sensitivity by a T-network configuration.

parallel with the feedback resistance, will decrease the expected sensitivity and lower the circuit's precision. A general solution to this drawback is to employ a T-network configuration, as shown in Fig.6-4, which allows high sensitivity measurement without using impractically gigantic feedback resistances [Franco 2002].

According to Kirchhoff law, the total current at node B in a closed loop should be zero:

$$-\frac{V_B}{R} - \frac{V_B}{R_2} + \frac{(V_{out} - V_B)}{R_1} = 0, \quad \text{where } V_B = -R I_{in} \quad (6-2)$$

$V_B$  can be eliminated by  $V_{out} = -R \cdot I_{in}$ , resulting

$$V_{out} = -k R I_{in}, \quad \text{where } k = 1 + \frac{R_1}{R_2} + \frac{R_1}{R} \quad (6-3)$$

Now, an arbitrary high sensitivity can be reached by using the combination of three reasonable resistors  $R$ ,  $R_1$  and  $R_2$ .

### • Low pass compensation

The factors which affect the stability of the transimpedance amplifier are the internal resistance  $R_S$  and the internal capacitance  $C_S$  of the current source (in our case, the immunosensor itself, Fig. 6-5). The bandwidth of the amplifier will be reduced since  $C_S$  efficiently acts as a short circuit for the current source at high frequencies. While the current flows along the feedback path from the output terminal to the inverting input ("-"), the feedback resistance  $R$  and  $C_S$  form a low-pass filter which contributes negative phase to the feedback loop, making the circuit instable, to overshoot, to ringing or even to oscillations.

In order to restore stability and to counteract the undesirable low-pass filter effect by  $R$  and  $C_S$  in the feedback path, a high-pass filter in the same path is required. This can be done by adding an additional feedback capacitor  $C_F$  [Fig.6-5].

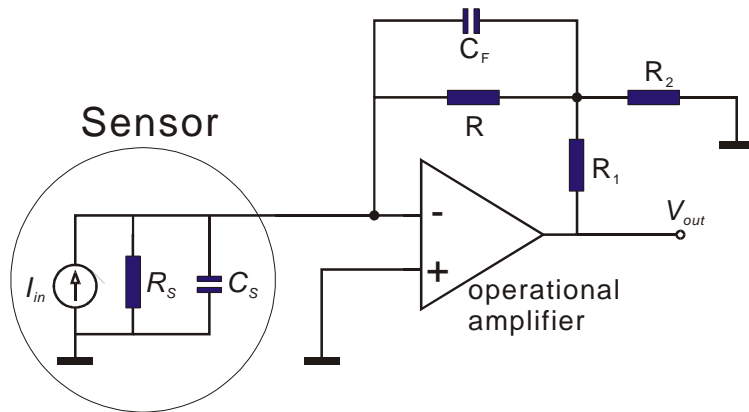


Fig.6-5 The feedback capacitance  $C_F$  and internal resistance  $R_S$  of the sensor form a high pass filter and compensates the effect of low pass filter by  $C_S$  and  $R$ .

As a result,  $C_F$  and  $R_S$  add supplementary positive phase to the loop and improve the stability of the circuit.  $C_F$  in parallel with the feedback resistance  $R$  in the feedback loop can also degrade the effect of parasitic capacitance at the output terminal [Karki 2000]. Table 6-1 lists the most common compensation methods for the parasitic capacitance in the inverting amplifier circuits.

Table 6-1 Inverting Amplifier: Capacitance location, Effect, and Compensation Summary

TOPOLOGY: INVERTING AMPLIFIER		
PARASITIC CAPACITOR LOCATION	EFFECT	COMPENSATION
All places	Various	Reduce capacitance and/or associated resistance
Negative input, $C_n$	Gain peaking or oscillation	Compensate with $C_F = C_n \cdot \frac{R_3}{R}$ across $R$ , and $C_1 = C_n$ across $R_3$
Positive input, $C_p$	None	None
Output, $C_o$	Gain peaking or oscillation	<ol style="list-style-type: none"> <li>If load is known, isolate with resistor, <math>R_i = R_o</math>. This causes load dependence.</li> <li>If load is unknown, isolate with resistor, <math>R_i = R_o</math> and provide ac feedback from isolated point with</li> </ol> $C_F = C_{out} \frac{R_o + R_i}{R_3 // R}$ Provide DC feedback from $V_{out}$ .
NOTES		
<p><math>R_o</math> is the output resistance of the operational amplifier. <math>C_n</math> is the parasitic capacitance in the inverting input.</p> <p>The input voltage difference between two input terminals is <math>V_i</math> and <math>a</math> is the open-loop gain of the operational amplifier.</p>		

### 6.1.4 System Setup

The total setup of the two-probe system is shown in Fig.6-7. The constant amplitude AC voltage signal was generated by a Hewlett-Packard HP 33120A function generator. An operational amplifier OPA 604 from Burr-Brown was utilized. The feedback configuration of  $C_F$  and  $R$  was 1 pF and 1 k $\Omega$ , respectively, while  $R_1$  and  $R_2$  were 50 k $\Omega$  and 1 k $\Omega$  respectively.

The current flowing through the sensing system is converted into voltage by the transimpedance amplifier and immediately read out by a FLUKE PM 3380A oscilloscope. For higher precision and resolution, a lock-in amplifier from the company Syncrotrack can be used for read-out, which will selectively detect signals at the measuring frequency and suppress the contributions from noise. Therefore, all other signals with different frequencies and noise will be filtered out. The whole process was controlled and monitored by a personal computer through GBIB interface.

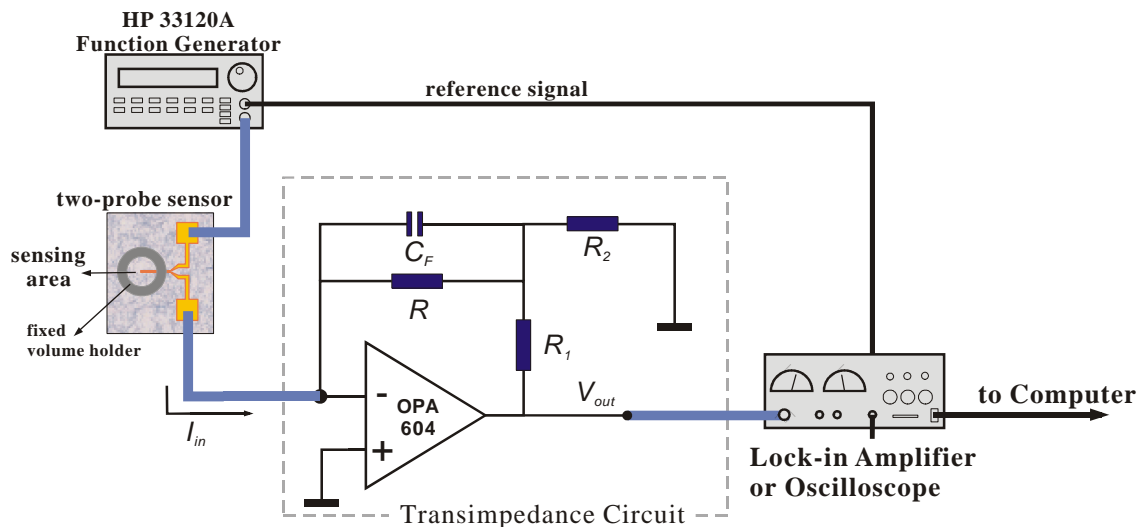


Fig.6-7 Total setup of a two-probe electrochemical immunosensor. An AC voltage signal with constant amplitude was sent by the function generator, the output current was measured by the transimpedance circuit. The read out device was an oscilloscope or a lock-in amplifier. The sensing area of the sensor was encircled by a volume holder to prevent the overflow of the sample solution.

## 6.2 Four-probe Sensor

As described above, the two-probe system is very sensitive to the capacitance change of the surface layer caused by the specific binding of the biomolecules. Another type of electrical sensing system is the four-probe system. It is also important to verify that the results with this technique are compatible with those of the two probe system.

### 6.2.1 Design and production of the electrodes

The four-probe sensor was fabricated in the same way as the two-probe system. Four gold electrodes were sputtered on the glass substrate. The geometry and the arrangement of electrodes are shown in Fig. 6-8(a). Each of the electrodes has identical dimension as the electrode of the two-probe system. The center gap is  $40\ \mu\text{m}$  wide, while the two outer gaps are  $20\ \mu\text{m}$  in distance. A thin insulating layer was applied on the whole surface of the sensor to protect the electrodes.

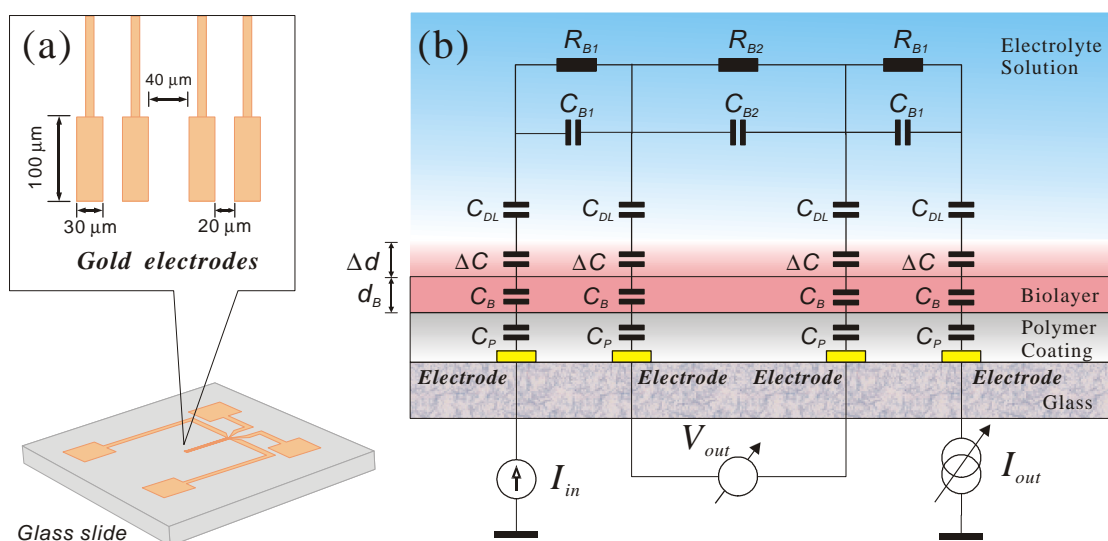


Fig.6-8 Schemes of (a) the four-probe electrical sensor with gold electrodes ,and (b) its electrical model. All the symbols are defined as in section 6.1.  $R_{B1}$  and  $R_{B2}$  are bulk resistances between different electrodes since the resistance of the bulk solution depends on the separation distance of the electrodes in liquid.

### 6.2.2 Electrical Model

Fig. 6-8(b) shows the electrical model for the four-probe system. The outer two electrodes are in principle subjected to a constant AC current  $I_{in}$ , and the voltage difference  $V_{out}$  between inner two electrodes is measured by the voltmeter. The total

current  $I_{out}$  can be measured by the transimpedance amplifier described in the section 6.1.3. Then, the impedance of the whole sensing system can be written as  $Z = V_{out}/I_{out}$ . The impedance increases with the increase in thickness of the biolayer caused by specific binding, which is theoretically identical to the case of the two-probe system. In practice, an AC voltage with a constant amplitude  $V_{in}$ , instead of a constant current source, was applied to the first electrode in order to suppress the effect of parasitic capacitance of the lead cable. In this case, according to the voltage dividing principle, the output voltage difference between inner two electrodes is given by

$$V_{out} = \frac{R_{B2} V_{in}}{(2/i\omega C_p) + (2/i\omega C_{AB}) + (2/i\omega \Delta C) + (2/i\omega C_{DL}) + R_{B2} + 2R_{B1}} \quad (6-4)$$

where  $\omega$  is the angular frequency of the applied voltage.  $R_{B2}$  and  $R_{B1}$  are bulk resistances but with different values since the resistances depend on the separation distance between the electrodes.

### 6.2.3 Required Electronics and Total Setup

Although a constant amplitude AC voltage was used as the source, a quasi-constant AC current source can be approximated by putting a large resistor of 100 M $\Omega$  which is much higher than the input impedance of the sensor between the voltage source (function generator) and the sensor. The readout device for the output current  $I_{out}$  was the same as the transimpedance amplifier described in the section 6.1. The readout device for the output voltage is a differential amplifier as follows:

#### • Difference Amplifier Circuit

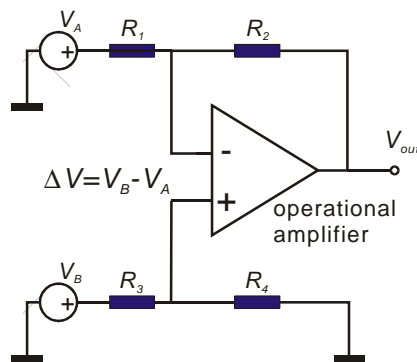


Fig.6-9 A typical difference amplifier circuit. The input voltage difference ( $V_B - V_A$ ) will be amplified at the output.

The most common used device for measuring the voltage difference is the difference amplifier shown in Fig.6-9. The operational amplifier utilizes a negative feedback resistance  $R_2$ , and a bias resistance  $R_4$  at the non-inverting input. Two different voltages,  $V_A$  and  $V_B$ , are imposed at the inverting and non-inverting inputs, respectively. Then the output voltage can be represented as

$$V_{out} = \frac{R_2}{R_1} \left[ \frac{1 + (R_1/R_2)}{1 + (R_3/R_4)} \cdot V_B - V_A \right] \quad (6-5)$$

It is important to note that if the resistors in Fig.6-9 are chosen specifically to satisfy the following relation, called **balanced bridge**:

$$\frac{R_3}{R_4} = \frac{R_1}{R_2} \quad (6-6)$$

The output voltage simplifies to

$$V_{out} = \frac{R_2}{R_1}(V_B - V_A) \quad (6-7)$$

The output voltage is directly proportional to the voltage difference of the inputs (differential-mode), indicating that if  $V_B$  equals to  $V_A$  (i.e. in common-mode condition), the output voltage should be zero for an ideal difference amplifier. This means that the common mode signal will not be amplified by an ideal difference amplifier. But actually due to the resistance mismatching and for a real difference amplifier in practical usage, the common-mode signals will still be amplified. This makes the output signal inaccurate. The countermeasure is to design an amplifier circuit which rejects the common-mode signals as follows:

- Common-Mode Rejection Ratio (CMRR)

The differential input component can be defined as  $V_{DM} \equiv V_B - V_A$  and common-mode input component as  $V_{CM} \equiv (V_B + V_A)/2$ . Hence, the inputs  $V_A$  and  $V_B$  can be represented in terms of the  $V_{DM}$  and  $V_{CM}$  as

$$V_A = V_{CM} - \left(\frac{V_{DM}}{2}\right), \quad V_B = V_{CM} + \left(\frac{V_{DM}}{2}\right) \quad (6-8)$$

These new expressions suggest that in reality for arbitrary inputs  $V_A$  and  $V_B$ , there always exists a low level differential-mode signal  $V_{DM}$  superimposed to a high level common-mode signal  $V_{CM}$ , but only the differential-mode signal  $V_{DM}$  is useful [Fig.6-10].

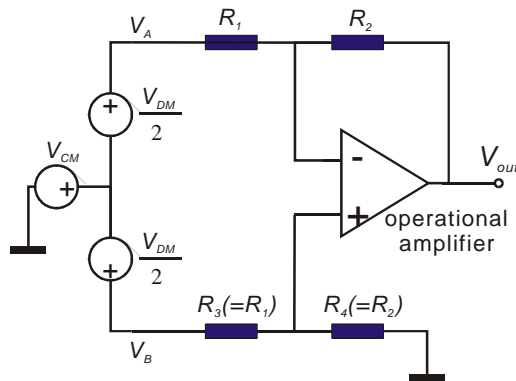


Fig.6-10 The inputs  $V_A$  and  $V_B$  can be expressed by the combinations of common-mode signal and differential-mode signal.

Therefore, the signal  $V_{DM}$  needs to be extracted from the high common-mode circumstance and be amplified. A difference amplifier does not respond to  $V_{CM}$  only when it is simultaneously ideal and satisfying the **balanced bridge** relation. To characterize the bridge imbalance an **imbalance factor  $b$**  is introduced, where  $0 \leq b \leq 1$ . It is assumed that only

the resistor  $R_4$  is deviating from its nominal value  $R_2$  to  $R_4 = R_2(1-b)$ , while the other

three resistors meet their required values. The imbalance of  $R_4$  changes the output voltage  $V_{out}$  in equation (6-7) to

$$V_{out} = -\frac{R_2(1-e)}{R_1} \cdot \left( V_{CM} - \frac{V_{DM}}{2} \right) + \frac{R_1 + R_2(1-e)}{R_1} \times \frac{R_2}{R_1 + R_2} \cdot \left( V_{CM} + \frac{V_{DM}}{2} \right) \quad (6-9)$$

$$\equiv A_{DM} \cdot V_{DM} + A_{CM} \cdot V_{CM}$$

where

$$A_{DM} = \frac{R_2}{R_1} \cdot \left( 1 - \frac{R_1 + 2R_2}{R_1 + R_2} \cdot \frac{e}{2} \right), \quad \text{and} \quad A_{CM} = \frac{R_2}{R_1 + R_2} \cdot e$$

As a result, the difference amplifier amplifies both  $V_{DM}$  and  $V_{CM}$  sensitively, if the balance bridge condition does not hold. The  $A_{DM}$  and  $A_{CM}$  are defined as **differential-mode gain** and **common-mode gain**, respectively. An ideal amplifier, with  $A_{DM} = R_2 / R_1$  and  $A_{CM} = 0$ , will be achieved only if the imbalance factor  $e$  approaches zero. The ratio of  $A_{DM}$  and  $A_{CM}$  in decibels [dB] is defined as the **Common-Mode Rejection Ratio (CMRR)**, which characterizes the immunity of an amplifier against common-mode signals:

$$\text{CMRR}_{\text{dB}} = 20 \log_{10} \left| \frac{A_{DM}}{A_{CM}} \right| \quad (6-10)$$

The CMRR approaches infinity for an ideal difference amplifier if  $A_{CM}$  approaches zero. The larger the ratio  $R_2 / R_1$ , the higher the CMRR of the difference amplifier circuit. Practically, the common-mode signal can be eliminated by adjusting one of the resistors, usually the bias resistor  $R_4$ , because  $R_1$  and  $R_2$  control the gain of the circuit. For inverting amplifiers, such as the transimpedance amplifier, the CMRR is not that important due to the virtual ground, where  $V_A = V_B = 0$ , and common-mode signal always equals zero, independent of common-mode gain  $A_{CM}$ .

### • Instrumentation Amplifier circuit

An ideal instrumentation amplifier has following advantages:

- A. Extremely high input impedance, ideally infinite, to prevent loading the sensor signal.
- B. Very low output impedance, ideally zero ohm,
- C. Accurate and stable gain,
- D. Extremely high common-mode rejection ratio.

The difference amplifier circuit described in the last two sections does meet the last three requirements, but not the first one. Taking Fig.6-10 for example, the operational amplifier utilized in that circuit has input impedance which consists of input resistance  $R_{DM}$  and input capacitance  $C_{DM}$  in parallel with two inputs [Fig.6-11(a)], where the lower

index “DM” represents that the amplifier operates in differential mode (i.e. no common-mode signal). The input resistance  $R_{DM}$  is usually extremely high ( $10^{12}$   $\Omega$  in our case), thus does not affect the total input impedance of the operational amplifier. But  $C_{DM}$  shorts the amplifier at high frequency, degrading the total input impedance.

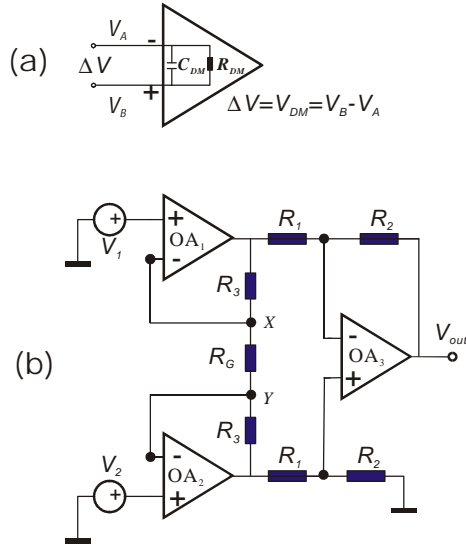


Fig.6-11 (a) The input impedance of an operational amplifier in differential-mode is composed of  $C_{DM}$  and  $R_{DM}$  in parallel with the differential input  $\Delta V$ .  
(b) The triple-OP-AMP instrumentation amplifier circuit. The gain of the circuit can be adjusted by only a single resistor  $R_G$ .

On the other hand, another essential drawback of the difference amplifier circuit is that the overall input impedances of the circuit are not high enough for both differential-mode and comm.-mode inputs, only  $2R_1$  and  $(R_1 + R_2)/2$ , respectively. Such a circuit with low input impedance following after a small signal source (in our case, the sensor itself) will load the source and result in a serious inaccuracy of measurements.

It is also not impractical to use resistors with huge resistance to improve the input impedance of the circuit, because it is difficult to maintain the balanced bridge relation [equation (6-6)] for high resistance. Moreover, the high value CMRR will not be retained, either, if when balanced bridge is not held. Nevertheless,

the gain of amplifier cannot be easily changed by regulating those resistors.

These drawbacks can be solved by preceding it with a high-input-impedance buffer amplifier (a so-called voltage follower) for each input of the amplifier circuit. The result circuit is the “**triple-OP-AMP instrumentation amplifier**” [Fig.6-11(b)]. The  $OA_1$  and  $OA_2$  form the so-called input buffer stage, and  $OA_3$  forms the output stage. The voltage across resistor  $R_G$  is  $V_Y - V_X$  which results in a current  $I_G$  flowing through the resistor  $R_G$ . The current flows through  $R_3$  is the same as  $I_G$ , since the feedback loops of the  $OA_1$  and  $OA_2$  draw no current. Because of the virtual ground,  $V_X = V_1$ ,  $V_Y = V_2$ , and from Ohm’s law, the current  $I_G$  can be written as:

$$I_G = (V_Y - V_X)/R_G = (V_2 - V_1)/R_G \quad (6-11)$$

The output voltages from the  $OA_1$  and  $OA_2$  buffer stages, respectively, are  $V_{O1}$  and  $V_{O2}$ :

$$V_{O1} = -I_G \cdot R_3 + V_X = -I_G \cdot R_3 + V_1 = -[(V_2 - V_1)/R_G] \cdot R_3 + V_1 \quad (6-12)$$

$$V_{O2} = I_G \cdot R_3 + V_Y = I_G \cdot R_3 + V_2 = [(V_2 - V_1)/R_G] \cdot R_3 + V_2 \quad (6-13)$$

The output stage is found by the  $OA_3$  and works as a difference amplifier, so the final output voltage  $V_{out}$  from the  $OA_3$  is:

$$V_{out} = \frac{R_2}{R_1} \cdot (V_{O2} - V_{O1}) = \frac{R_2}{R_1} \cdot \left(1 + \frac{2 \cdot R_3}{R_G}\right) \cdot (V_2 - V_1) \equiv A \cdot (V_2 - V_1) \quad (6-14)$$

$$\text{where } A = \frac{R_2}{R_1} \cdot \left(1 + \frac{2 \cdot R_3}{R_G}\right)$$

The factor A is defined as the total gain of this circuit. It is quite obvious that the gain of the instrumentation amplifier depends on the external resistors, usually by adjusting the resistor  $R_G$  and leaving the other resistors unchanged so as to keep the bridge balance condition.  $OA_1$  and  $OA_2$  are in the non-inverting configuration, so they provide extremely high closed-loop input resistance. Similarly, the output resistance of  $OA_3$  is quite low, since  $OA_3$  operates in the difference amplifier configuration. The maximal CMRR value of the circuit can be achieved by well adjusting of resistances  $R_2$  and  $R_1$  at the output stage. Besides, choosing a proper operational amplifier with high CMRR value for the output stage is also very significant. The CMRR of the circuit must satisfy the following equation:

$$\frac{V_{DM}}{V_{CM}} \ll 10^{CMRR/20} \quad \text{or} \quad CMRR \gg 20 \cdot \log_{10} \left| \frac{V_{DM}}{V_{CM}} \right| \quad (6-15)$$

In conclusion, this circuit does meet all the conditions an ideal instrumentation amplifier requires. But, even an amplifier circuit with high CMRR is built, there still exists a vital problem which degrades the CMRR: The parasitic capacitance of the cable, which results in the CMRR degradation with the frequency.

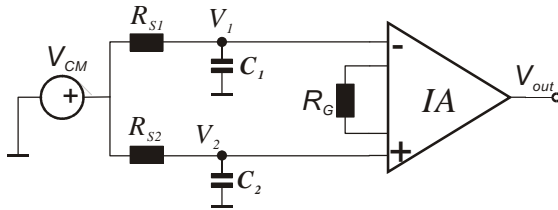


Fig.6-12 "IA" represents the instrumentation amplifier circuit. IA with source resistances  $R_{S1}$ ,  $R_{S2}$  and parasitic capacitances  $C_1$ ,  $C_2$  at input cables causes a RC imbalance and a voltage difference when only common-mode single exists.

For example, in Fig.6-12,  $R_{S1}$  and  $R_{S2}$  denote the source resistances at the inputs, while  $C_1$  and  $C_2$  denote the parasitic capacitances at each input. Even though the circuit operates ONLY under a common-mode input signal  $V_{CM}$ , the output voltage of this instrumentation amplifier may not be zero, if the time constants at each input,  $R_{S1}C_1$  and  $R_{S2}C_2$ , are not the same. In this case, the time constants imbalance makes the voltages irregular, i.e.  $V_1 \neq V_2$ , and the difference error will be amplified by the following instrumentation amplifier, resulting in a non-zero output, even if the inputs are common-mode signals. The CMRR due to a RC imbalance is [Burr 1987]:

$$CMRR \cong 20 \cdot \log_{10} \cdot \frac{1}{2p \cdot f \cdot R_{DM} \cdot C_{CM}} \quad (6-16)$$

where  $R_{DM} = |R_{S1} - R_{S2}|$  is the source resistance imbalance, and  $C_{CM} = (C_1 + C_2)/2$  is the common-mode capacitance between each wire and ground shield, and  $f$  is the

frequency of the common-mode input signal. For a signal with a frequency of 150 Hz, a resistance imbalance of  $R_{DM} = 1000 \Omega$  and a common-mode capacitance  $C_{CM} = 20 \text{ pF}$ , the CMRR reduces to 94.5dB even with an instrumentation amplifier possessing infinite CMRR. The situation gets worse when the circuit operates at high frequency. For example, at 100 KHz under the same resistance imbalance  $R_{DM}$  and common-mode capacitance  $C_{CM}$ , the CMRR degrades strongly to 30.1dB.

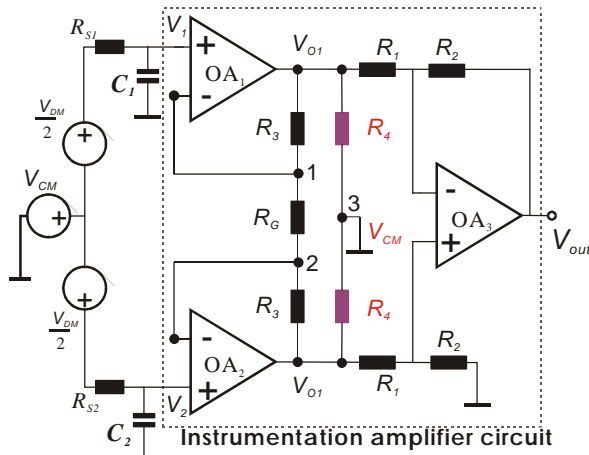


Fig.6-13 The parasitic capacitance in the input cables can be neutralized by driving the ground shield with the common-mode voltage itself ( $v_{CM}$ ). The  $v_{CM}$  can be obtained from the mean of  $V_{O1}$  and  $V_{O2}$  at node 3.

Therefore, it is necessary to modify the circuit in order to neutralize the common-mode capacitance  $C_{CM}$ . This is done by driving the ground shield with the common-mode voltage itself, so that the common-mode swing across  $C_{CM}$  is reduced to zero. The common-mode voltage are obtained as follows:

Let the voltages at inputs of  $OA_1$  and  $OA_2$  are  $V_1$  and  $V_2$  respectively, According to the definition of common-mode voltage for equation (6-8), the resulting common-mode voltage at present becomes  $v_{CM} = (V_1 + V_2)/2$ , which

can be obtained by the mean of output voltages from  $OA_1$  and  $OA_2$  :

$$\begin{aligned} v_{CM} &= (V_1 + V_2)/2 \\ &= (V_1 + V_3 + V_2 - V_3)/2 = (V_{O1} + V_{O2})/2 \end{aligned} \quad (6-17)$$

where  $V_3$  is the voltage drop across resistor  $R_3$ , and  $V_{O1}$ ,  $V_{O2}$  are output voltages of  $OA_1$  and  $OA_2$ . It should be noted that because of virtual ground, the voltage at nodes 1 and 2 are also  $V_1$  and  $V_2$  respectively. From equation (6-17), the common-mode voltage  $v_{CM}$  can be extracted by connecting two identical resistors  $R_4$  from  $V_{O1}$  and  $V_{O2}$ , to the ground shield, respectively, since the voltage at node 3 is just the same as  $v_{CM}$ . The common-mode voltage is now successfully be dropped out from the circuit [Franco 2001]. Now, the voltage difference between the inner two electrodes of the four-probe electrochemical immunosensor can be measured by the improved instrumentation amplifier circuit shown in Fig.6-13.

The operational amplifier INA 111 from Burr-Brown is chosen for the output stage  $OA_3$  because of its high CMRR (110 dB) with a differential-mode gain of 10 up to 200 Hz. The CMRR of INA 111 decreases 20 dB per decade above 200 Hz. In the frequency range from 100 Hz to 1 MHz equation (6-15) is valid. The OPA 604 from Burr-Brown is chosen to serve as the buffer stage  $OA_1$  and  $OA_2$  for its high input impedance of  $10^{12} \Omega$ .

### 6.2.4 System Setup

Fig.6-14 shows the complete setup of the four-probe sensing system. The output current was amplified and converted to voltage by the transimpedance amplifier circuit described in the section 6-1, followed by the FLUKE PM3380 oscilloscope from the company or by a Syncrotrack Lock-in amplifier. The voltage difference between the two inner electrodes was amplified by the instrumentation amplifier circuit described in the section 6.2.3 and followed by a readout device consisting of a Princeton Lock-in amplifier from the company. All the devices are connected to a personal computer through a GBIP interface for monitoring and registration of the data.

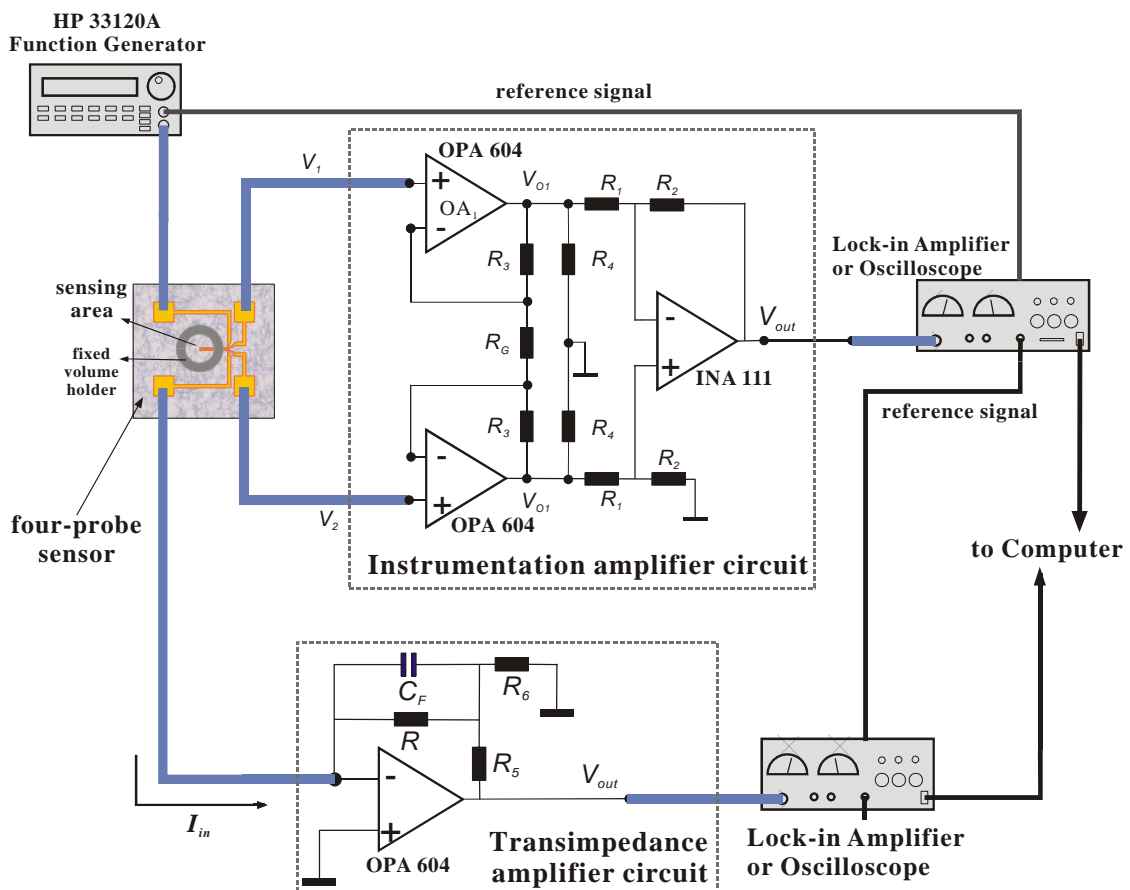


Fig. 6-14 Total setup of a four-probe electrochemical sensing system. The transimpedance amplifier measures the output current, while the instrumentation amplifier determines the output voltage between the two inner electrodes.

## 6.3 Measurements

### 6.3.1 Bare electrode

First of all, the electrical sensor with only bare electrodes was tested by measuring three kinds of aqueous solutions with given ionic concentration: sodium chloride (150 mM, milli-mole per liter), potassium chloride (150 mM) and PBS, obtained from a mixture of 137 mM NaCl, 2.7 mM KCl and 10 mM phosphoric acid solution. The electrical current in an electrolyte driven by a constant amplitude AC voltage is dependent on the concentration and the mobility of the ions in the aqueous liquid. The mobility of an ion is the final velocity that the particle achieves in an electric field of 1 Volt per meter. The units of mobility are therefore  $(\text{m/s}) / (\text{V/m}) = \text{m}^2 / (\text{s V})$ . Table 6-2, 6-3 lists the mobility and conductivity of some ions in water at 25 °C. It is obvious that for ions having the same valence, the larger ion possesses the higher mobility. This is because of the surface charge distribution (charge density) of small ions which is higher than that of large ions. Therefore, it attracts more water molecules, resulting in a larger hydrated ion radius, which drops mobility and conductivity.

Table 6-2 Ionic mobility in water

Ion	Atomic Weight (amu)	Mobility in Water [ $\text{m}^2/(\text{s V})$ ]
Hydrogen ( $\text{H}^+$ )	1.00	$36.3 \times 10^{-8}$
Lithium ( $\text{Li}^+$ )	6.94	$4.01 \times 10^{-8}$
Sodium ( $\text{Na}^+$ )	22.99	$5.19 \times 10^{-8}$
Potassium ( $\text{K}^+$ )	30.09	$7.64 \times 10^{-8}$
Chloride ( $\text{Cl}^-$ )	35.36	$7.91 \times 10^{-8}$

Table 6-3 Molar Conductivities at Infinite Dilution for Various Sodium and Potassium Salts in Aqueous Solution at 25 °C

Electrolyte	Conductivity [ $\Omega^{-1} \text{cm}^2 \text{mol}^{-1}$ ]	Electrolyte	Conductivity [ $\Omega^{-1} \text{cm}^2 \text{mol}^{-1}$ ]
<b>KCl</b>	<b>149.9</b>	<b>NaCl</b>	<b>126.5</b>
<b>KI</b>	<b>150.3</b>	<b>NaI</b>	<b>126.9</b>
$\frac{1}{2} \text{K}_2\text{SO}_4$	<b>153.5</b>	$\frac{1}{2} \text{Na}_2\text{SO}_4$	<b>130.1</b>

The proton, on the contrary, as a big exception, has a large mobility. This can be attributed to the strong hydrogen bond between  $\text{H}^+$  and  $\text{H}_2\text{O}$ , so that the proton always appears in the form of  $\text{H}_3\text{O}^+$ ,  $\text{H}_3\text{O}_2^-$ , or  $\text{H}_5\text{O}_2^+$ ...etc, which are larger than other ions. In our experiments, the concentration of  $\text{H}^+$  is quite low ( $\text{pH}=7.2$ ), so the  $\text{H}^+$  ions do not dominate the conductivity of the solution.

Sodium, which is 84% of the size of potassium, carries a charge density 43% higher than the potassium ions, and resulting in the attraction of a much larger water shell. Since the mobility of the  $\text{K}^+$  ion is higher than that of the  $\text{Na}^+$  ion, the conductivity of KCl solution is larger than

NaCl solution, when their concentrations are the same.

A droplet was dripped on the surface of the sensor, on which the sensing area was

already limited by a volume holder, for example, a circuit track marked by a biopen<sup>(\*)</sup> from the company G. Kisker, or by silicon rubber, or a glass wall, so as to constrain the sample liquid from overflow.

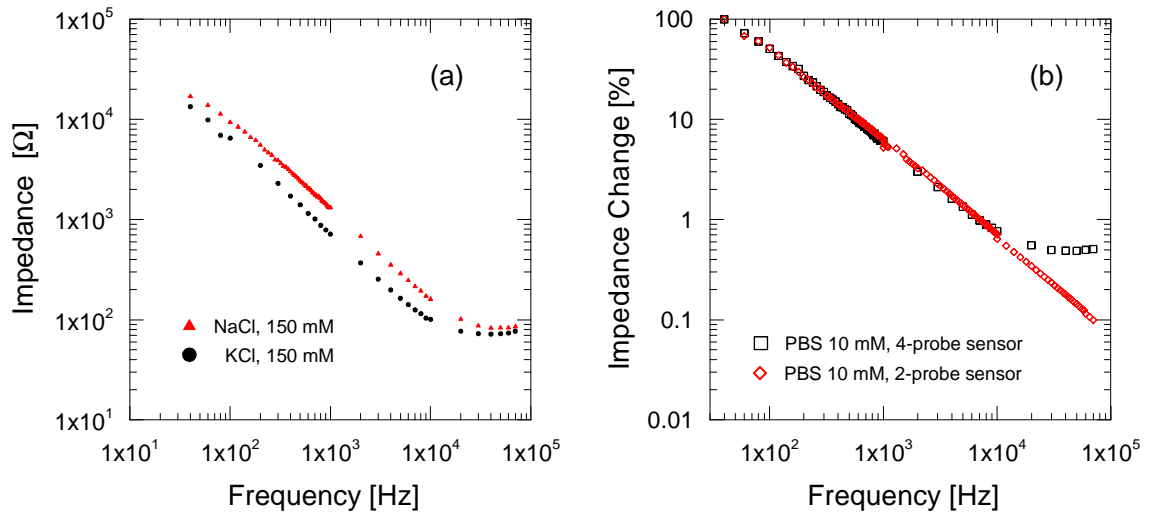


*Fig.6-15 Impedance measurements of (a) 150 mM KCl and NaCl solution measured with four-probe sensor, and (b) 10 mM PBS solution measured with two- and four-probe sensor. An ohmic impedance appears at lower frequencies for the four-probe sensor.*

In Fig.6-15(a), the impedance of KCl and NaCl with the same concentration was measured with the four-probe sensor in a given frequency range. The measured impedance of the KCl solution is smaller than that of NaCl, in coincidence with the above conclusions. Fig.6-15(b) demonstrates the difference between two- and four-probe sensors. In the case of the four-probe sensor, the impedance of the PBS solution in the low frequency range (below 10 kHz) behaves fully capacitively, while at higher frequency (above 10 kHz), the impedance seems to be ohmic. This is because the capacitances of all layers adjacent to the sensor surface are shorted at high frequency and only the ohmic resistance of the bulk solution contributes to the impedance of the system. However, the frequency necessary to short the capacitances in the two-probe sensor is much higher than for the four-probe sensor. The normalized impedance (with respect to the impedance at the lowest frequency of 40 Hz) in the case of the two-probe sensor behaves still completely capacitively even above 100 kHz, which almost exceeds the limit of the operation frequency of the lock-in amplifier. Therefore, at high frequencies, the four-probe sensor will suppress the effect of capacitance of the layers more strongly than the two-probe sensor, indicating that for capacitive measurements, for example the thickness change of a dielectric layer, the two-probe sensor is more suitable because it can operate in a wider frequency range. For measurements of very small deviations in conductivity of the bulk solution, for example electrophoresis, the four-probe sensor is

\* The biopen can be utilized to draw a ring track to confine the sample liquid to a fixed area, not to overflow. The ink is highly hydrophobic.

favorable since at higher frequencies (above 1 kHz), the ohmic resistance of the bulk solution dominates the impedance of the system [Laugere 2001]. However, if the experiments will be operated in low frequencies (below 1 kHz), the difference of results between using 2- and 4- probe systems is little.

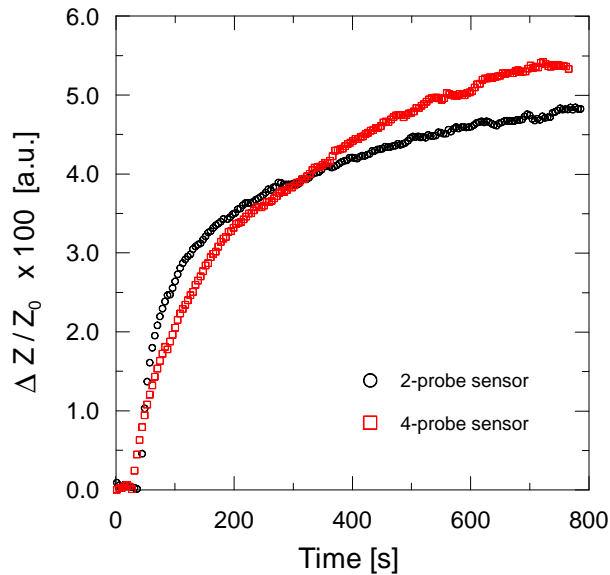
### 6.3.2 Antibody Immobilization

Measurements without immobilizing the antibodies on the sensor surface were carried out on bare electrodes at 25 °C, i.e. both antibodies and antigens were suspended in the 10 mM phosphate buffer solution with pH=7.2. The frequency and amplitude of the input AC voltage are 137 Hz and 100 mV (peak-to-peak). Bare electrodes were cleaned by absolute pure acetone first and then washed by distilled absolute pure water, followed by drying with compressed nitrogen. A droplet with probe antibodies was dripped on the surface of the sensor. When the monitored signal stabilized, the same amount of the droplet of target antigen was pipetted onto the sensing area of the sensor.

Unfortunately, there was no significant change of resulting signal in the case of two-probe sensor, even also the specific immunoreaction occurred. A similar result was obtained for the four-probe sensor, indicating that interaction of the biomolecules did not influence the electrical property of the PBS bulk solution. This can be explained by the fact that the PBS solution has high ohmic conductivity, which is not influenced by the activities of antibodies and antigens, even though they are dielectric particles if suspended in the bulk solution. Furthermore, the bulk capacitance does not dominate the electrical characteristics of a high conductivity electrolyte. Hence, the immobilization of antibodies on the surface of the sensor is required for electrical sensing.

Next, immobilization of antibodies using the “protein A” method, the same as for the SAW-sensor, was tried. The gold electrodes were incubated with protein A solution of concentration 500 µg/ml for 1 hour. After washing the surface with PBS, the sensor was dried by compressed nitrogen carefully, followed by immobilizing the probe antibody from a 1.2 mg/ml solution on the surface for 1 hour, and was washed again. Subsequently, the surface was blocked with 3% BSA (Bovine Serum Albumin, solved in PBS) solution for 30 minutes.

After the same cleaning process, a 5µl of PBS droplet was dripped on the sensor surface. When the monitored signal stabilized, 5µl of 1.2 mg/ml specific antigen solution was pipetted into the PBS droplet. The resulting variation of the output signal was still not optimal, only about 5% change obtained for two- and four-probe sensors (Fig 6-16). These phenomena could originate from that the protein A did not homogeneously cover all the electrode surface. According to the last section in chapter 5, there might be many vacant



binding sites on the electrode surface, providing the electric signals a direct coupling to the highly conductive electrolyte, thus degrading the effect of the capacitance change.

*Fig.6-16 Normalized impedance changes for a specific immunoreaction measured by two- and four-probe sensors. The probe antibodies were immobilized on the electrodes by protein A. The operating frequency is 137 Hz. Only about 5% of the expected change of impedance was observed for both sensors.*

### 6.3.3 PMMA Coating

Poly-methylmethacrylate (PMMA) is a popular insulating material which meets the requirements for insulating and protecting electrodes from aggressive buffer solution. The relative dielectric constant of PMMA is 2.2 ~ 3.2 at 1 MHz and 3.3 ~ 3.9 at 50 Hz (at 100 Hz,  $\epsilon = 3.6$ , and at 1000 Hz,  $\epsilon = 3.2$ ). The volume resistivity of PMMA is  $10^{15}$  [ohm-cm]. Like the preparation of PMMA for the SAW-sensor, 5% w/v PMMA solved in ethyl ethoxyacetate solution was spread homogenously on the surface of the sensor by the spin coating method, and was baked in the oven at 180 °C for at least hours for evaporating the ethyl ethoxyacetate, hardening the PMMA coating and smoothing the PMMA surface. An antibody solution of 5 micro liters with the concentration of 1.2 mg/ml was added onto the 5 $\mu$ l PBS solution placed already on the surface of the sensor for 1 hour, followed by the blocking process for 30 minutes with 3% BSA solution. Between each step the sensor was cleaned carefully by PBS and dried with compressed nitrogen. As usual, 5 $\mu$ l PBS was put on the sensing area before pipetting the antigen droplet. The resulting change of output signals from to different sensors is shown in Fig.6-17. Obviously, the output signals respond with a 15% variation in impedance to the binding of specific antigen with probe antibodies, and almost no response was obtained for the non-specific antigen, suggesting that PMMA provides good insulation and physical adsorption of antibody molecules like in the case of the surface acoustic wave sensor.

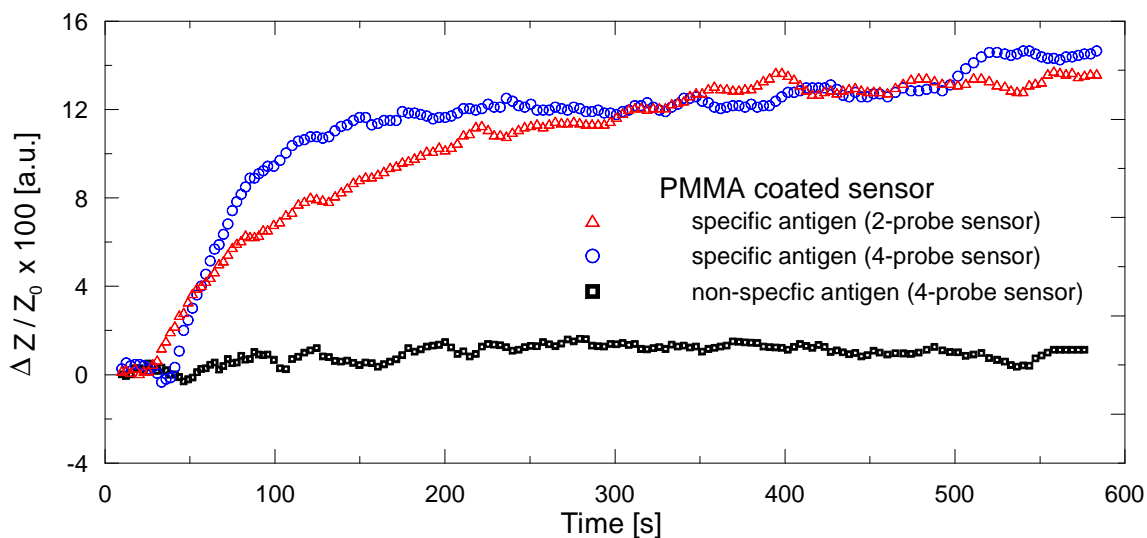


Fig.6-17 Normalized impedance changes due to immunoreactions of a PMMA coated sensor at 500 Hz. The concentration of antigen sample was 1.2 mg/ml. Both two- and four-probe sensor demonstrate about 15% impedance changes for the specific immunoreaction.

### 6.3.4 Polystyrene Coating

Polystyrene is also common for the insulation of electrodes for the reason that it has an extremely high electrical volume resistivity of  $10^{15} \sim 10^{17} \Omega\text{-cm}$ , and the relative dielectric constant of  $2 \sim 2.8$  in the frequency range between 50 Hz  $\sim$  1 MHz. Therefore, a contactless detection can also be achieved. The second reason is that polystyrene possesses high affinity to biomolecules, especially protein. Thus, antibodies can easily be attached to the sensor surface through physical adsorption at the polystyrene layer.

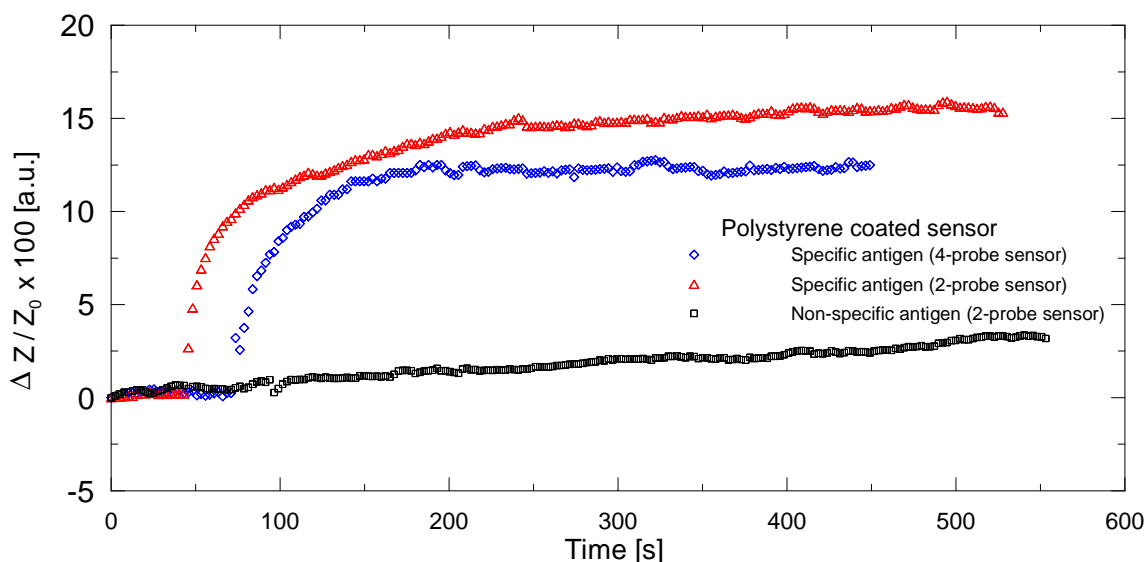


Fig.6-18 Normalized impedance changes due to immunoreactions of a polystyrene coated sensor at 500 Hz. The concentration of antigen sample was 0.9 mg/ml. Both two- and four-probe sensor demonstrate about 15% impedance changes for the specific immunoreaction.

A polystyrene solution (5% v/w, solved in the toluene) was prepared for the following surface coating. Using the spin-coating method, a polystyrene film was spread over the whole surface. Then, the sensor with polystyrene coating was baked in an oven at 100°C for at least 2 hours, in order to smoothen the polystyrene surface and to harden the coating.

The preparation of the probe antibodies and the measurements were identical with those described in the last section, and the results are shown in Fig.6-18. It is obvious that polystyrene also shows excellent suitability as a material for electrode insulation and protein immobilization.

Fig.6-19 shows a series of measurements for a two-probe sensor operated at 37 Hz. Obviously, the sensor did differentiate between specific and non-specific antigen. The first specific antigen sample caused a 40% change in output current while the second specific antigen sample with higher concentration resulted in an additional 20% change in the output current. At the end, the non-specific antigen sample did not cause a significant variation.

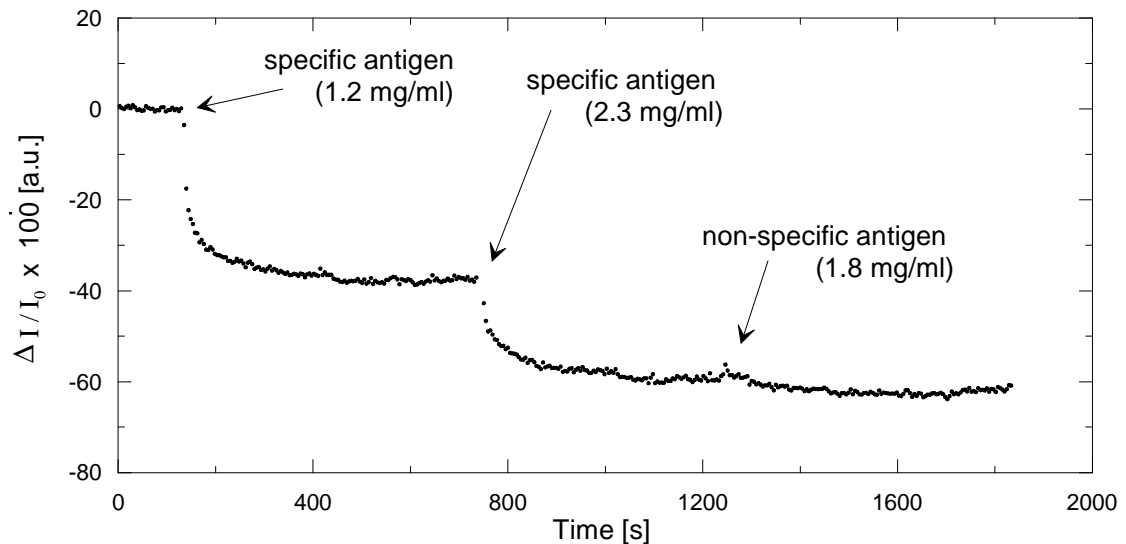


Fig. 6-19 A series of measurements measured with a two-probe sensor at 37 Hz. Specific antigen samples were added onto the sensor at two different concentrations, demonstrating a high specificity. The third measurement was carried out with a non-specific antigen sample.

### 6.3.5 Influence of the gap width

In this section, the separation distance between electrodes for the two-probe sensor will be discussed. A series of sensors with different separation distance was made: 20  $\mu\text{m}$ , 40  $\mu\text{m}$ , 100  $\mu\text{m}$ , 200  $\mu\text{m}$  and 400  $\mu\text{m}$ . From the electrical model in section 6-1, the distance between electrodes does not affect the layer capacitance, only the resistance and

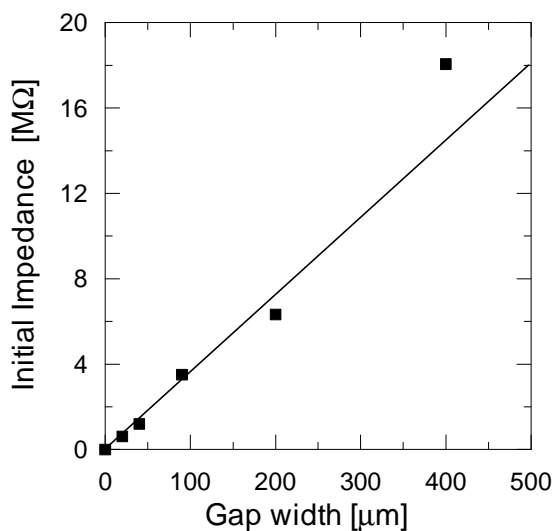


Fig.6-20 Initial input impedance of sensors with different gap width. The measurements were done using bare electrodes with 0.01 M PBS solutions.

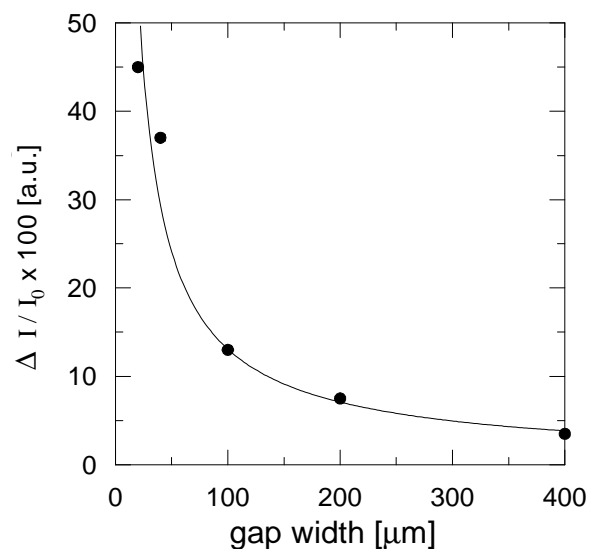


Fig.6-21 Specific immunoreaction measured with two-probe sensors at a frequency and an amplitude of applied voltage of 137 Hz and 0.1 V.

capacitance due to the bulk solution will be affected. In other words, only the background impedance is concerned with the gap width. Fig.6-20 indicates the initial impedance versus the gap width. The data were measured with bare electrodes covered only by 0.01M PBS solution at room temperature at an operation frequency of 137 Hz. It shows that the narrower the gap width of a sensor, the lower its impedance.

Fig. 6-21 shows the current changes associated with specific immunoreactions measured with sensors with different gap widths.



# Chapter 7

## Antibody Activities in Liquid - Effects of the AC Electrokinetics

AC electrokinetic techniques have been widely used to manipulate or separate biological particles, such as latex spheres, viruses, proteins [Morgan 1999], bacteria [Pohl 1978], and cancer cells from blood [Becker 1995]. In fact, during the measurement of the antibody-antigen reaction using the electrochemical sensor, the electrolyte and biomolecules are subjected to an alternating electric field at every moment. That means the target objects which we are dealing with are not in a static, but a dynamic and nonequilibrium state. In this chapter, the influence of the AC electric field onto both the electrolyte and biomolecules will be discussed; the factors that bring about the instability while performing the electrical sensing will also be examined.

Solid phase adsorption of protein at the solid-liquid interface has found with interest and has been discussed so far [Tilton 1990]. The protein adsorption happens in three main steps [Sarkar 1993]:

1. **Diffusion** of protein from bulk to solid-liquid interface. The diffusion rate is substantially proportional to the original concentration of the protein in bulk.
2. **Formation of complex** with active binding sites on the solid surface. The higher enthalpy a protein molecule possesses, the faster the active spots are saturated.
3. **Molecular rearrangement** through protein-protein interaction. This step is a slow process which does not strongly depend on the original concentration of protein in bulk. It allows to accommodate more proteins at the interface.

These conclusions above were obtained from measurements by spectro- photometry without the effect of applied electric field. The measured adsorption rate of protein at a solid-liquid interface is much slower than that from the diffusion theory [Penners 1981].

This is coincident with the measurement results by the electrical sensor in chapter 6. The observed curves did not behave themselves as smoothly as the curves obtained from the SAW-Sensor, and for long duration of measurements, the curves started to drift. It is reasonable to suspect that these unfavorable phenomena could have arisen from the effects of electric field which couples with the ions in the bulk solution. The bulk electrolyte is composed of many kinds of cations and anions, and will surely response to the applied electric field, which may either obstruct or promote the protein binding. The heating caused by electrical power may also be an important factor, which directly influences to the activity of every molecule in the bulk and protein itself. The total forces acting on the protein molecule are sedimentation, Brownian, dielectrophoretic, hydrodynamic, electrothermal, and electro-osmosis forces. In the following sections, the influence of the AC electric field to the protein-protein interaction will be discussed to verify the reliability of the sensor.

## 7.1 Dielectrophoresis

Induced charges accumulate at the particle-medium interface, when a particle suspended in the electrolyte is subjected to a uniform electric field. The amount of induced charge depends on the polarisability of the particle and the electrolyte. An effective electric dipole moment will be generated by these induced charges surrounding the particle. A force is exerted on the effective particle dipole, if the applied electric field is non-uniform. The resulting particle movement is called “*dielectrophoresis*” (DEP).

The effective dipole moment  $\bar{m}$  of a linear and isotropic dielectric spherical particle is [Stratton 1941]:

$$\bar{m}(\omega) = 4\pi a^3 \epsilon_m f_{CM}(\omega) \bar{E} \quad (7-1)$$

where  $a$  is the radius of the particle,  $\epsilon_m$  is the permittivity of the medium,  $\bar{E}$  is the applied electric field,  $\omega$  is the frequency. The factor  $f_{CM}$  is the Clausius-Mossotti factor, which represents the frequency dependence of the effective polarisability of the particle and is given by

$$f_{CM}(\omega) = \frac{\epsilon_p^* - \epsilon_m^*}{\epsilon_p^* + 2\epsilon_m^*} \quad (7-2)$$

where  $\epsilon^* = \epsilon - i\sigma/\omega$ ,  $\epsilon_p^*$  and  $\epsilon_m^*$  are the complex permittivity of the particle and medium respectively,  $\epsilon$  is the permittivity,  $\sigma$  is the conductivity. If the electric field is not uniform, the time-average dielectrophoretic force  $F_{DEP}$  is given by [Jones 1995]:

$$\begin{aligned} \langle \bar{F}_{DEP} \rangle &= \text{Re}[(\bar{m} \cdot \nabla) \bar{E}] = \frac{1}{2} \text{Re}[(\bar{m}(\omega) \cdot \nabla) \bar{E}^*] \\ &= 2\pi a^3 \epsilon_m \text{Re}[f_{CM}(\omega)] \nabla |E_{rms}|^2 \end{aligned} \quad (7-3)$$

where  $E_{rms}$  is the rms electric field. The real part of the Clausius-Mossotti factor is between 1 and -1/2. If  $\text{Re}[f_{CM}(\omega)]$  is positive, then the particle will be subject to a positive dielectrophoresis force, which drives the particle toward the region of high electric field (Fig. 7-1).

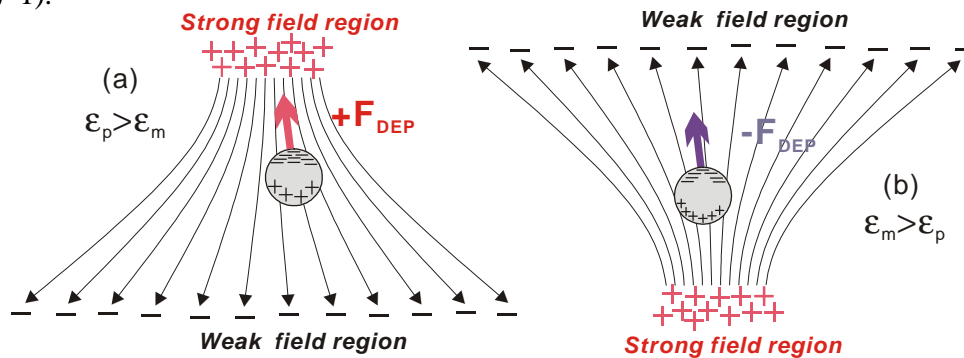


Fig. 7-1 Dielectrophoretic forces when (a)  $\epsilon_p > \epsilon_m$ , dielectric particle tends to region of high field density, and (b)  $\epsilon_p < \epsilon_m$ , tends to region of low field density.

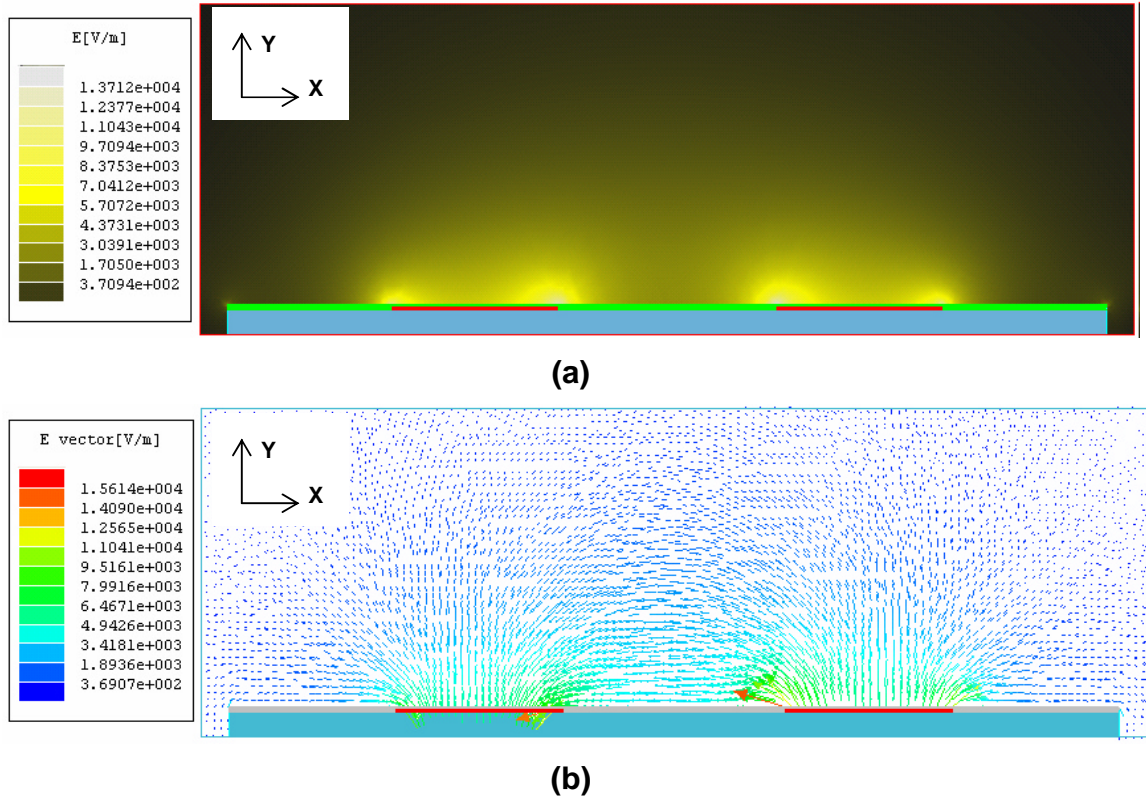


Fig.7-2 Finite element simulations of (a) electric field intensity and (b) electric field vector distributed in the 10 mM PBS solution in the case of the two-probe sensor. The input voltage is  $0.1 V_{peak-peak}$ . The electric field in the liquid generated by the applied voltage is non-uniform. The highest field is at the inner edges (near the gap) of the separated electrodes.

The dielectric properties of various protein molecules have been calculated from computer simulation, which shows that the values of relative permittivity of different proteins are widely discrepant from 2 to 40 [Pitera 2001]. It is obviously to infer that the real part of the Clausius-Mossotti factor in our case is negative, because the medium, PBS solution, has a relatively higher permittivity (near that of water) than antibody molecules. For example, assuming that the relative dielectric constant of antibody  $\epsilon_p = 5$  and of the 10 mM PBS solution (with only 0.7 % salt in water)  $\epsilon_m = 78.5$ , the resulting Clausius-Mossotti factor is minus 0.4 under the conditions of the measurements at a frequency of 137 Hz in chapter 6, indicating that the antibody molecule experiences a negative dielectrophoretic force and be pushed to the region of low electric field strength, i.e. the center part between electrodes. A finite element simulation of the electric field generated by the 2-probe electrical sensor by the Ansoft Maxwell 2D software is shown in Fig. 7-2(a), and (b). From the simulation, the high field regions are at the edges of the electrodes, while the low field regions are at the center of the gap between the electrodes. Fig 7-3 describes the square of the gradient of the of electric field versus horizontal position at different vertical position above the surface, which implies that the highest

dielectrophoretic force appears at the edges of the electrodes, and it decreases with distance from the sensor surface.

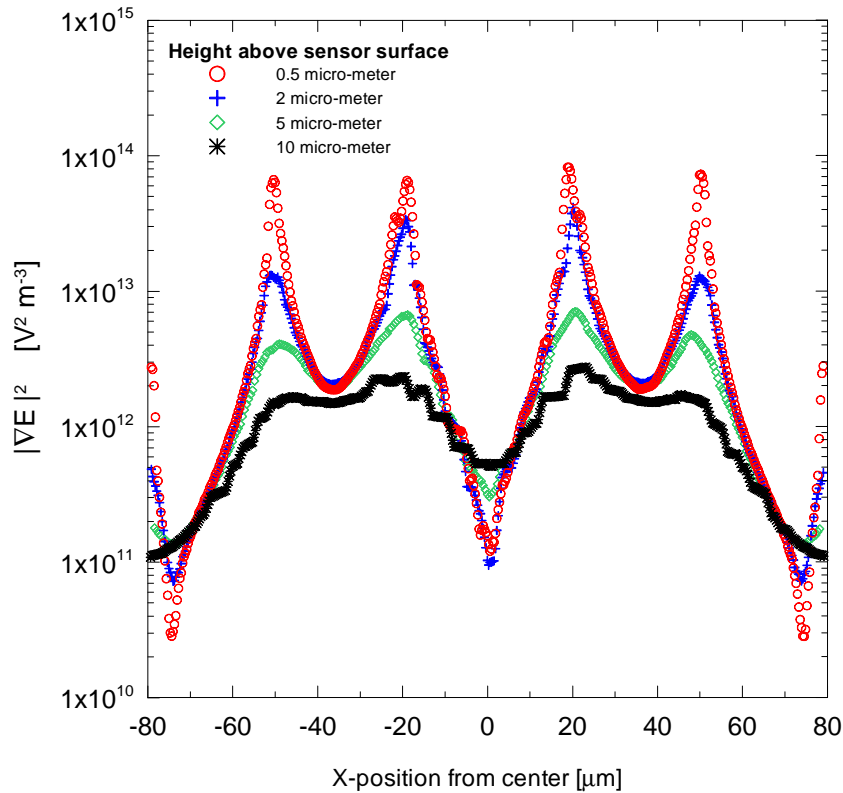


Fig.7-3 Square of the gradient of the electric field versus x-position at different heights (along y-axis) indicates that at the same horizontal plane on the electrode, the dielectric force is greater when the particle is near the electrode surface.

The dielectrophoretic forces acting on the antibody molecule located at the edge of the right electrode ( $x = 20 \mu\text{m}$ ) and resulting velocity with different heights are listed in Table 7-1. The velocity of the molecule can be estimated from Stoke's equation:

$$\mathbf{u}_{DEP} = \frac{F_{DEP}}{6\pi\eta a}$$

where  $\eta$  is the viscosity of the medium and  $a$  is the radius of the molecule, assuming that the viscosity  $\eta \sim \eta_{\text{water}} = 8.9 \times 10^{-4} \text{ [Ns/m}^2\text{]}$  and the antibody molecule is quasi-spherical with a radius  $a = 5 \text{ nm}$ .

Table 7-1. The dielectrophoretic forces acting upon an antibody molecule at  $x = 20 \mu\text{m}$  (inner edge of the right electrode) and resulting velocity at different heights.

Height above the surface [μm]	Square of Gradient of Electric field [V <sup>2</sup> m <sup>-3</sup> ]	Negative dielectrophoretic force [N]	Dielectrophoretic velocity [mm/s]
0.5	$1.04 \times 10^{14}$	$2.27 \times 10^{-20}$	$2.71 \times 10^{-4}$
2	$4.41 \times 10^{13}$	$9.62 \times 10^{-21}$	$1.14 \times 10^{-4}$
5	$7.52 \times 10^{12}$	$1.64 \times 10^{-21}$	$1.95 \times 10^{-5}$
10	$2.64 \times 10^{12}$	$5.76 \times 10^{-22}$	$6.87 \times 10^{-6}$

In principle, the real part of Clausius-Mossotti factor is also dependent on the frequency of the applied electric field, suggesting that there is a crossover frequency at which the dielectrophoretic force equals to zero. However, whenever permittivity and conductivity of the antibody molecule are smaller than that of the bulk electrolyte solution, the crossover frequency will be infinitely low. Therefore, the dielectrophoretic force effect is unavoidable when applying the electrical detection for antibody-antigen binding. This can be avoided by choosing a buffer solution, whose conductivity or permittivity is lower than that of the antibody molecule. Fortunately, the calculated velocity of this movement is not so fast in our measurement conditions. By the  $0.1 V_{p-p}$  applied voltage, an antibody at  $0.5 \mu\text{m}$  above the inner edge of electrode needs several hours to escape from the electrode edge to the center of the gap. However, at a position which is infinitely close to the surface, the dielectrophoretic force is large enough to move the antibody molecule out of the surface and interfere with the measurement.

## 7.2 Brownian motion and diffusion

Aside from the dielectrophoretic force, there are other factors that present problems when scaling AC Electrokinetics from the micrometer to nanometer scale. These include Brownian motion, induced by thermal noise in the surrounding medium, and effects of conduction and convection of the medium, induced by the high electric fields. For sufficiently high concentrations of particles, a diffusion force would also be significant; however, the majority of work on dielectrophoresis has used sufficiently low concentrations of particles for each particle to be regarded as single and isolated.

Brownian motion due to thermal noise is well documented [Einstein 1905]. For small particles, especially of molecular size, the dielectrophoretic interaction may be defeated by the thermal randomization [Washizu 1994]. To overcome this situation, the dielectrophoretic potential  $U_{DEP}$  must be greater than the thermal energy, in order of magnitude:

$$U_{DEP} = 2\mathbf{p} a^3 \mathbf{e}_m \operatorname{Re}[f_{CM}(\mathbf{w})] |E_{rms}|^2 \geq kT \quad (7-4)$$

where  $k$  is the Boltzmann constant and  $T$  the temperature. In the case of the 2-probe system, the applied electric field  $|E_{rms}|$  is about  $1.8 \times 10^3$  [V/m], and the resulting DEP potential  $U_{DEP}$  is about  $5.7 \times 10^{-16}$  J, which is much greater than the thermal energy  $kT \sim 4.1 \times 10^{-21}$  J at 25 °C, indicating that the Brownian motion caused by thermal noise is of secondary importance and does not significantly affect the motion of the antibody molecule.

This result is similar to other studies of dielectrophoretic force required to trap particles against Brownian motion [Pohl 1978; Washizu 1994; Hughes 1998]. Experimental studies with proteins [Washizu 1994; Bakewell 1998] have demonstrated that Brownian motion does not prevent the trapping of particles as small as 68 kDa (equivalent to a cube 6 nm along a face) by negative dielectrophoresis or 25 kDa by positive dielectrophoresis.

For a collection of particles, a statistic is also needed to predict the movement and distribution of the ensemble [Kittel 1965]. The particle conservation equation is:

$$\frac{\partial n}{\partial t} + \bar{\mathbf{u}} \cdot \nabla n = -\nabla \cdot \bar{\mathbf{J}}_T \quad (7-5)$$

where  $n$  is the number of particle per unit volume and  $\bar{\mathbf{J}}_T$  is the total flux consisting of the sum of the diffusion, sedimentation and dielectrophoretic fluxes:

$$\bar{\mathbf{J}}_T = \bar{\mathbf{J}}_D + \bar{\mathbf{J}}_g + \bar{\mathbf{J}}_{DEP} \quad (7-6)$$

$$\text{where } \bar{J}_D = -D\nabla n, \bar{J}_g = \frac{n\bar{F}_g}{6pha}, \bar{J}_{DEP} = \frac{n\bar{F}_{DEP}}{6pha}$$

The gravitational force pulls the particles downwards, i.e. from the bulk solution to the sensor surface, so the dielectrophoretic force, either negative or positive. By being pulled through gravitational and dielectrophoretic forces, the antigens are captured by immobilized antibodies on the sensor surface. As a result, a concentration gradient is formed due to the simultaneous decrease in concentration of particles in the bulk solution above the electrodes, suggesting that a diffusion flux is generated, which is in the same direction as the dielectrophoretic force according to equation (7-6).

This motion will continue until all of the antigens are captured. Therefore, as long as the antigens are captured specifically and held strongly, sedimentation and diffusion will enhance the effects of the dielectrophoretic force; otherwise, the diffusion force will act upon the antigens and make them diffuse back to the bulk solution, until the total system reaches a static state, in which the antigens are redistributed and the net flux is zero. So, Brownian motion is insignificant against the dielectrophoretic force for the 2-probe sensor, and diffusion has a positive contribution to the dielectrophoretic force.

## 7.3 Electrohydrodynamics

In the previous sections, the effects of the high strength AC electric field, which is generated by planar electrodes, and the thermal noise acting on the antibody molecules have been discussed. In fact, the AC electric field does manipulate not only the protein particles, but also the electrolyte, i.e. the buffer solution, itself. Two main mechanisms cause the motion inside the liquid; one of them is the Joule heating by the AC electric field. The resulting localized temperature gradients may change the dielectric properties of the electrolyte, which produce gradients in conductivity and permittivity. The interactions of the AC electric field and the non-uniform properties of the electrolyte locally form bulk forces on the fluid, which drives the fluid flow; for example, the local liquid density change causes buoyancy force, which leads to a natural convection; the local conductivity change gives rise to formation of free volume charges, which interact with the non-uniform AC electric field, implying that a Coulomb force arises. The regional permittivity difference induces dielectric force in an AC electric field.

The other important mechanism which drives the inner liquid flow is electro-osmosis, which will be discussed in detail in the next section. In this section, the first inevitable effect of the electrical Joule heating will be considered.

### 7.3.1 Joule heating by applied AC voltage

The AC electric fields suggest that there is a power density generated in the electrolyte around the electrodes. The power generation per unit volume  $W$  is given by

$$W = \mathbf{s} E^2 \quad \text{W}\cdot\text{m}^{-3} \quad (7-7)$$

where  $\mathbf{s}$  is the conductivity of the electrolyte and  $E$  is the strength of the electric field. For the two-probe sensor, the average electric field strength  $|E_{rms}|$  is  $1.76 \times 10^3 \text{ V}\cdot\text{m}^{-1}$ , and the typical conductivity of the PBS solution  $\mathbf{s}$  is considered to be  $0.011 \text{ S}\cdot\text{m}^{-1}$ . Then the average power dissipation per unit volume in the inter-electrode volume can be estimated to be  $3.43 \times 10^4 \text{ W}\cdot\text{m}^{-3}$ . The volume over which the heat is generated between the two electrodes is about  $40 \mu\text{m} \times 40 \mu\text{m} \times 1500 \mu\text{m} = 2.40 \times 10^{-12} \text{ m}^3$ . So the time average power dissipation for the sensor is  $8.23 \times 10^{-8} \text{ W}$ . Let us compare this value with the power dissipation from the measured data: at 100 Hz, the electrical impedance  $R$  of a two-probe sensor with bare electrodes is  $4.66 \text{ M}\Omega$ , while the applied voltage is  $V_{rms} = 0.035 \text{ V}$ , the resulting power dissipation is  $2.62 \times 10^{-10} \text{ W}$ ; at 100 kHz, the impedance is

6.30 k $\Omega$  and resulting power dissipation is  $1.98 \times 10^{-7}$  W, implying that the time average power dissipation from equation (7-7) is of the same order of magnitude as the measured data..

The Joule heating caused by the applied electric field produces a local temperature gradient, resulting in a non-uniform distribution in permittivity and conductivity. A body force will be induced, since the AC electric field interacts with a bulk electrolyte with non-uniform dielectric properties. Consequently, an inner movement of the bulk solution occurs. In order to estimate the temperature change due to the applied AC field, the energy balance equation must be used:

$$\mathbf{r}_m c_p \frac{\partial T}{\partial t} + \mathbf{r}_m c_p \bar{\mathbf{v}} \cdot \nabla T = k \nabla^2 T + \mathbf{s} E^2 \quad (7-8)$$

where  $\mathbf{r}_m$  is the mass density,  $c_p$  is the specific heat at constant pressure,  $\bar{\mathbf{v}}$  is the fluid velocity,  $k$  is the thermal conductivity,  $\mathbf{s}$  is electrical conductivity of the medium,  $T$  is the temperature and  $E$  is the electric field. It is assumed that at the beginning, the system is in a steady-state, i.e. the temperature of the system, including the liquid and the electrodes, is stable and does not change with time; therefore, the first term approaches zero. Further, from the observation of the motion of latex spheres in the 2-probe system, the velocity of latex particle is in the range of 1-10  $\mu\text{m/s}$ , therefore the ratio of convection of heat to heat diffusion is very small, i.e.  $\mathbf{r}_m c_p \bar{\mathbf{v}} \cdot l/k \sim 10^{-3} \ll 1$ . Then the equation (7-8) can be simplified to [Ramos 1998]

$$k \nabla^2 T + \mathbf{s} E^2 = 0 \quad (7-9)$$

The solution to this equation is

$$T = T_0 + \frac{\mathbf{s} E^2 d}{2k} \left( x - \frac{x^2}{d} \right) \quad (7-10)$$

with the boundary conditions  $T = T_0$  at the electrode surface,  $x = 0$  and  $x = d$ , where  $d$  is the separation of the electrodes. The maximum temperature occurs at the center of the separation:

$$T = T_0 + \frac{\mathbf{s} E^2 d^2}{8k} \quad (7-11)$$

The temperature difference is  $\Delta T = \frac{\mathbf{s} V_{rms}^2}{8k}$ . In our case the electrical conductivity of PBS solution is about  $0.011 \text{ S}\cdot\text{m}^{-1}$  and the input voltage  $V_{rms}$  is 0.0707 V. The resulting temperature rise is estimated to be  $1.5 \times 10^{-5} \text{ }^\circ\text{C}$ , which is too small to cause a response of the two-probe sensing system. Fig. 7-4 shows the sensor response while adding a 5  $\mu\text{L}$  PBS drop of  $50 \text{ }^\circ\text{C}$  into the same solution with  $25 \text{ }^\circ\text{C}$  only, indicating that for a temperature difference up to  $25 \text{ }^\circ\text{C}$ , the signals come back to their initial values and thermal equilibrium is established within 10 seconds. Therefore, the Joule heating caused by the electric field can be ignored whilst the applied voltage is not too high. On the other

hand, the antibody molecules will not be denatured by such a small temperature difference.

Equation (7-11) also means that electrolytes with higher conductivity lead to larger temperature differences. After the long duration of the measurement, the exceeding temperature rise caused by the high conductivity may speed up the evaporation rate of the water and cause further increase on the conductivity of the buffer solution; thus, the situation becomes a vicious circle. Even though the sensor is not sensitive to temperature change, the antibodies may possibly be denatured.

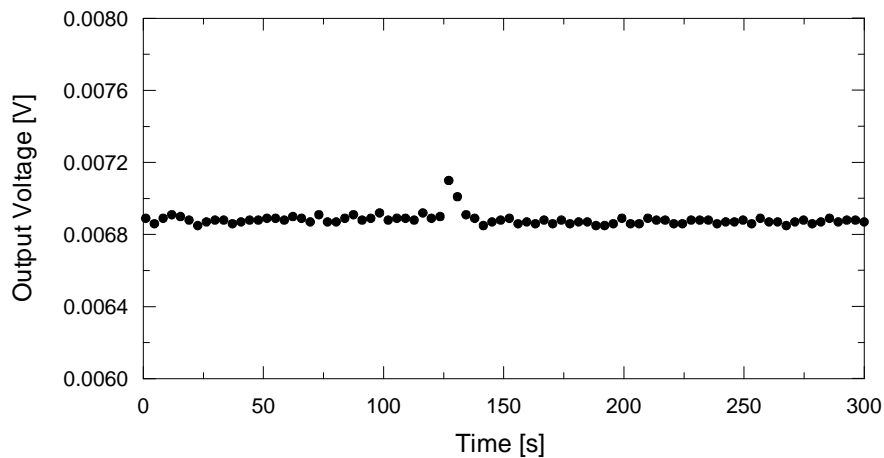


Fig.7-4 (a) Temperature response of the 4-electrode sensor. At 120 seconds 50 °C, 5 $\mu$ L PBS was added into the same amount of 25 °C PBS solution. The thermal equilibrium was restored within 10 seconds. The applied AC voltage was 0.5 Volt at 500 Hz.

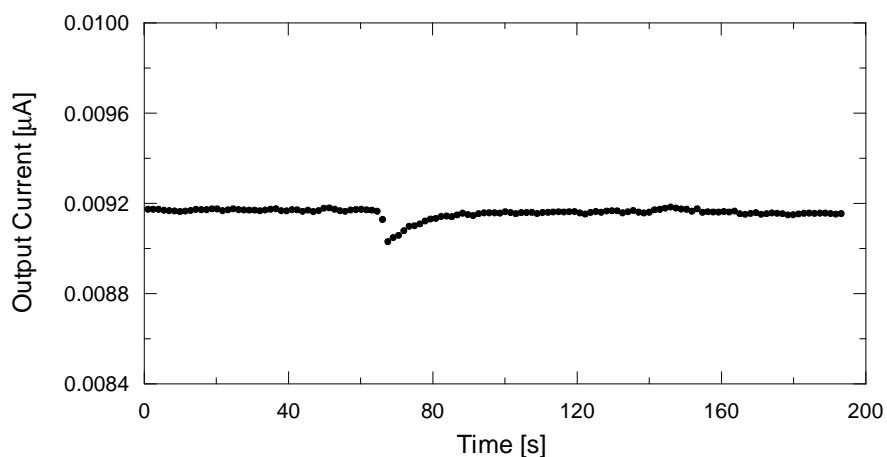


Fig.7-4 (b) Temperature response of the 2-electrode sensor. At 70 seconds 50 °C, 5 $\mu$ L PBS was added into the same amount of 25 °C PBS solution. The thermal equilibrium was restored within 10 seconds. The applied voltage was 0.8 Volt at 137 Hz.

### 7.3.2 Coulomb and dielectric force

The inhomogeneity in temperature gives rise to several body forces: buoyancy force, which brings about the natural convection, Coulomb force, and dielectric force. The electrical force per unit volume on a liquid is given by [Stratton 1941]

$$\vec{f}_E = \mathbf{r}_q \bar{E} - \frac{1}{2} \bar{E}^2 \nabla \mathbf{e} + \frac{1}{2} \nabla \left( \mathbf{r}_m \frac{\partial \mathbf{e}}{\partial \mathbf{r}_m} \bar{E}^2 \right) \quad (7-12)$$

where  $\mathbf{r}_q$  is the volume charge density,  $\mathbf{r}_m$  is the liquid mass density, and  $\mathbf{e}$  is the permittivity of the electrolyte. The third term at the right hand side can be neglected because for an incompressible liquid it does not contribute to the dynamics. Supposing that the deviation of permittivity and conductivity due to temperature inhomogeneity is small, the total electric field can be written as  $\bar{E} = \bar{E}_0 + \bar{E}_1$ , where  $\bar{E}_0$  is the applied AC field,  $\bar{E}_1$  is the perturbation term and  $\bar{E}_0 \gg \bar{E}_1$ . Assuming that  $\nabla \cdot \bar{E}_0 = 0$ , then the charge density can be represented by

$$\mathbf{r}_q = \nabla \cdot (\mathbf{e} \bar{E}) = \nabla \mathbf{e} \cdot \bar{E}_0 + \mathbf{e} \nabla \cdot \bar{E}_1 \quad (7-13)$$

Substituting equation (7-13) into (7-12), to the first-order approximation, we have

$$\vec{f}_E = (\nabla \mathbf{e} \cdot \bar{E}_0 + \mathbf{e} \nabla \cdot \bar{E}_1) \bar{E}_0 - \frac{1}{2} \bar{E}_0^2 \nabla \mathbf{e} \quad (7-14)$$

The charge conservation equation is

$$\nabla \cdot (\mathbf{s} \bar{E} + \mathbf{r}_q \bar{\mathbf{u}}) + \frac{\partial \mathbf{r}_q}{\partial t} = 0 \quad (7-15)$$

where  $\mathbf{r}_q \bar{\mathbf{u}}$  is the convection of the charge, which can be neglected because its divergence is quite small comparing with the divergence of the ohmic current:

$$\frac{|\nabla \cdot (\mathbf{r}_q \bar{\mathbf{u}})|}{|\nabla \cdot (\mathbf{s} \bar{E})|} \cong \frac{|\mathbf{r}_q \bar{\mathbf{u}}|}{|\mathbf{s} \bar{E}|} = \frac{|\nabla \cdot (\mathbf{e} \bar{E}) \bar{\mathbf{u}}|}{|\mathbf{s} \bar{E}|} \cong \frac{\mathbf{e} / \mathbf{s}}{l / \mathbf{u}} \quad (7-16)$$

where  $l$  and  $\mathbf{u}$  denote the distance and velocity, respectively. Equation (7-16) represents the important physical statement that the ratio of the convective current and ohmic current is of the order of the ratio of the charge relaxation time of the electrolyte and the time needed for a particle in electrolyte to travel a distance  $l$ . For example, taking a distance of 1  $\mu\text{m}$  and a velocity of 10  $\mu\text{m/s}$ , the time needed is 0.1 second, which is much greater than the charge relaxation time of the bulk solution. The charge-conservation equation can be rearranged by substituting for  $\bar{E}$  and neglecting the convective term:

$$\nabla \mathbf{s} \cdot \bar{\mathbf{E}}_0 + \mathbf{s} \nabla \cdot \bar{\mathbf{E}}_1 + \frac{\partial}{\partial t} (\nabla \mathbf{e} \cdot \bar{\mathbf{E}}_0 + \nabla \mathbf{e} \cdot \bar{\mathbf{E}}_1) = 0 \quad (7-17)$$

In our case the electric field varies with time,  $\bar{\mathbf{E}}_0(t) = \text{Re}(\bar{\mathbf{E}}_0 e^{i\omega t})$ , thus

$$\nabla \mathbf{s} \cdot \bar{\mathbf{E}}_0 + i\omega \nabla \mathbf{e} \cdot \bar{\mathbf{E}}_0 + \mathbf{s} \nabla \cdot \bar{\mathbf{E}}_1 + i\omega \mathbf{e} \nabla \cdot \bar{\mathbf{E}}_1 = 0 \quad (7-18)$$

Assuming that the bulk solution is non-dispersive in the frequency range of interest, the divergence of the perturbation field is given by

$$\nabla \cdot \bar{\mathbf{E}}_1 = \frac{-(\nabla \mathbf{s} + i\omega \nabla \mathbf{e}) \cdot \bar{\mathbf{E}}_0}{\mathbf{s} + i\omega \mathbf{e}} \quad (7-19)$$

Assuming that the bulk solution does not respond to the instantaneous value of the force at the frequency of applied field, the time-averaged force per unit volume can be found by substituting for the divergence of the perturbation field:

$$\begin{aligned} \langle \bar{f}_E \rangle &= \frac{1}{2} \text{Re} \left[ (\nabla \mathbf{e} \cdot \bar{\mathbf{E}}_0 + \mathbf{e} \nabla \cdot \bar{\mathbf{E}}_1) \bar{\mathbf{E}}_0^* - \frac{1}{2} |E_0|^2 \nabla \mathbf{e} \right] \\ &= \frac{1}{2} \text{Re} \left[ \left( \frac{-(\mathbf{e} \nabla \mathbf{s} + \mathbf{s} \nabla \mathbf{e}) \cdot \bar{\mathbf{E}}_0}{\mathbf{s} + i\omega \mathbf{e}} \right) \bar{\mathbf{E}}_0^* - \frac{1}{2} |E_0|^2 \nabla \mathbf{e} \right] \\ &= -\frac{1}{2} \left[ \left( \frac{\nabla \mathbf{s}}{\mathbf{s}} - \frac{\nabla \mathbf{e}}{\mathbf{e}} \right) \cdot \bar{\mathbf{E}}_0 \frac{\mathbf{e} \bar{\mathbf{E}}_0}{1 + (\omega \tau)^2} + \frac{1}{2} |E_0|^2 \nabla \mathbf{e} \right] \end{aligned} \quad (7-20)$$

where  $\tau = (\epsilon / \sigma)$  is the charge relaxation time of the electrolyte solution. The first term on the right hand side of the equation (7-20) is defined as Coulomb force and the second term is the dielectric force. Either Coulomb or dielectric force dominates in certain frequency ranges, i.e. these two forces compete with each other. There is a specific transition frequency  $f_c$  at which the magnitude of Coulomb force is the same as the magnitude of the dielectric force. The transition frequency derived from equation (7-20) is

$$\omega_c = 2\pi f_c \approx \frac{1}{\tau} \left( 2 \frac{\left| \frac{\partial \mathbf{s}}{\partial T} \right|}{\left| \frac{\partial \mathbf{e}}{\partial T} \right|} \right)^{1/2} \quad (7-21)$$

where we use the gradients in permittivity and conductivity due to small temperature rises

$$\nabla \mathbf{e} = \left( \frac{\partial \mathbf{e}}{\partial T} \right) \nabla T, \quad \nabla \mathbf{s} = \left( \frac{\partial \mathbf{s}}{\partial T} \right) \nabla T \quad (7-22)$$

Taking water for example, the transition frequency is 1.52 MHz [Green 2000]. An order of magnitude estimate of the  $f_c$  for the PBS solution can be simplified to the inverse of the charge relaxation time, i.e. about 4.7 MHz, which is much higher than the frequency used for the measurement. As a result, at low experimental frequencies the liquid is mainly subject to Coulomb forces, while at high frequency to the dielectric forces. At frequencies lower than  $f_c$ , the total electrical force acting on the bulk solution due to the applied

voltage  $V_{rms}$  in the 2-probe system can be calculated as [Appendix A]

$$\langle f_E \rangle = -M(\mathbf{w}, T) \left( \frac{e \mathbf{s} V_{rms}^4}{8k \mathbf{p}^3 r^3 T} \right) \left( 1 - \frac{2q}{\mathbf{p}} \right) \hat{n}_q \quad (7-23)$$

where the factor  $M(\mathbf{w}, T)$  is

$$M(\mathbf{w}, T) = \left( \frac{\frac{T}{\mathbf{s}} \frac{\partial \mathbf{s}}{\partial T} - \frac{T}{e} \frac{\partial e}{\partial T}}{1 + (\mathbf{w}t)^2} + \frac{1}{2} \frac{T}{e} \frac{\partial e}{\partial T} \right) \quad (7-24)$$

The direction and the magnitude of the force at frequencies lower than  $f_c$  are shown in Fig. 7-5.

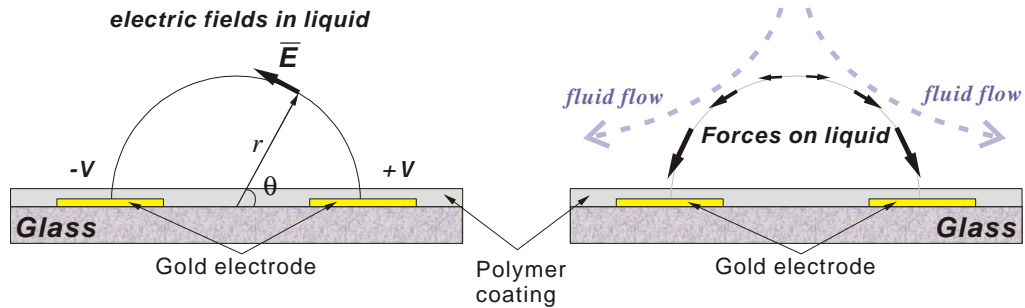


Fig.7-5 The induced non-uniform electric field (left) and the resulting forces acting upon the liquid, which causes the internal liquid flow (right). Note that magnitude and direction of the induced forces change with the position of the liquid and with the period of the applied voltage.

In our case (low frequency), at  $10 \mu\text{m}$  above the gap between electrodes, i.e.  $r = 10 \mu\text{m}$  and  $\theta$  around  $\pi/2$ , the resulting electrical force density is about  $6.24 \times 10^{-6} \text{ N}\cdot\text{m}^{-3}$ . Taking the characteristic length  $l = 40 \mu\text{m}$  as an example, the resulting flow velocity  $\mathbf{u}_{flow}$  is [Ramos 1998]

$$\mathbf{u}_E \approx \frac{|\bar{f}_E| l^2}{h} = 1.1 \times 10^{-5} [\mu\text{m}]$$

which is of the same order of magnitude as the velocity from the dielectrophoretic force, only the directions are opposite to each other. The electric force acting on the liquid generates inner fluid flows, whose directions are indicated by the large arrows in Fig 7-5. At the bottom of the liquid, the electrolyte flows from the center of the gap to both sides away from the center. The antigens suspended in the liquid will be dragged by this fluid flow rather than by the dielectrophoretic force. But at frequencies higher than the transition frequency, the inner liquid flows are in the same direction as the dielectrophoretic force. This technique is widely used for the trapping of particles in

certain positions [Müller 1996], or separation of different bio-molecules [Morgan 1999]. As the antigens were being dragged onto the surface of the electrodes by the fluid flow, the specific one will be captured by the antibodies immobilized on the electrodes, while non-specific one will continue to flow away with the inner liquid flow.

### 7.3.3 Convection

Natural convection happens in the bulk solution when it undergoes a buoyancy force due to the changes in the local mass density, which mostly arises from a local temperature gradient. The buoyancy force density  $\bar{f}_b$  can be obtained as

$$\begin{aligned}\bar{f}_b &= \Delta \mathbf{r}_m \bar{g} = \frac{\partial \mathbf{r}_m}{\partial T} \Delta T \bar{g} \\ &= \left( \frac{\partial \mathbf{r}_m}{\partial T} \right) \frac{\mathbf{s} V^2}{2k} \left( \frac{\mathbf{q}}{\mathbf{p}} - \frac{\mathbf{q}^2}{\mathbf{p}^2} \right) \bar{g}\end{aligned}\tag{7-25}$$

by substituting for the temperature change from equation A-7 in Appendix A, where  $\bar{g}$  is the acceleration of gravity. From the above equation, the maximum buoyancy force occurs at  $\theta = \pi/2$  for the same conditions. The resulting buoyancy force density is  $1.5 \times 10^{-8} \text{ N}\cdot\text{m}^{-3}$ , which is significantly smaller than that of the electrical force discussed in the last section. As a result, the effect of natural convection in the liquid can be neglected.

## 7.4 Electro-osmosis

The above sections have revealed many complicated dynamic phenomena existing in liquid while AC electrical sensing was performed. It may be these dynamics that perturb the stability of the sensor. These hydrodynamic models have been verified especially in the high frequency range by many authors [Müller 1996, Ramos 1998, and Green 2000]. However, in low frequency ranges the observed velocity of fluid flows is faster than the predicted velocity from the models above.

The additional contribution to the fluid movement originated in a mechanism called “electro-osmosis” [Ramos 1999, Scott 2001, Green 2002, and Castellanos 2003], which is based on the interaction of the AC electric field and the electrical double layers formed near the surface of the electrodes.

### 7.4.1 Electrical double layer

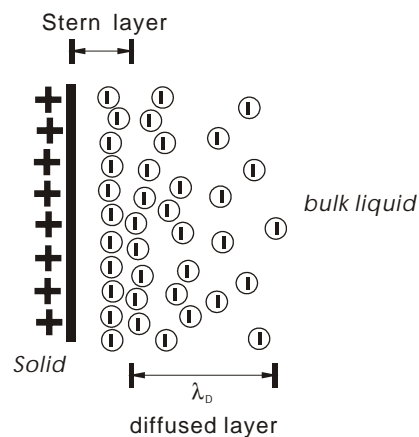


*Fig.7-6 Near the solid surface an electrical double layer are formed, which consists of the Stern layer and diffused layer. In the stern layer ions stay locally are close to the interface. In the diffused layer the ions can move more freely than those in the Stern layer.*

which is out of the Stern layer and characterized by a screening distance  $\lambda_D$ , namely the Debye length. Although the ions in the solution are mobile, it should be noted that an order of magnitude scale of the thickness of the double layer depends principally only on the temperature and the concentration of the ions [Hunter 1988].

The thickness of the electrical double layer  $\lambda_D$  near the solid-electrolyte is in the

In aqueous solution, the distribution of the charges near the planar surface is determined by the solution of Poisson-Boltzmann equation. As shown in Fig.7-6, at the electrode-electrolyte interface, the inner part of the double layer is called “Stern layer”. However, the ions keep a very small distance (sub-nanometer) from the surface of the solid phase. This is because the ions have a finite size so that they are not able to get closer than a certain distance from the solid surface [Hunter 1988]. Most of the ions are distributed in a diffused layer

order of magnitude of nanometers. According to the Debye-Hückel approximation, i.e. if the electrical energy across the electrode-electrolyte interface is smaller than the thermal energy ( $|z_i e \mathbf{y}| < kT$ , where  $z_i$  is the valence of the  $i_{th}$  ion and  $e$  is the charge of the electron,  $\mathbf{y}$  is the electrical potential across the interface), the thickness of the electrical double layer  $l_D$  is given by

$$l_D = \frac{\sqrt{\epsilon_m RT}}{F \left( \sum_i z_i^2 c_i \right)^{1/2}} \quad (7-26)$$

where  $\epsilon_m$  is the permittivity of the medium,  $R$  is the gas constant,  $T$  is the temperature,  $F$  is Faraday's constant,  $z_i$  and  $c_i$  are the valence and concentration of the  $i_{th}$  ion in the medium. The concentrations of the main components of the phosphate buffered saline (PBS) are listed in table 7-2. The calculated thickness of the electrical double layer of PBS in our application is only about 20 nm, which is merely twice as large as the length of an antibody molecule.

Table 7-2. The concentrations of the ions in the PBS solution.

Main ion in PBS	Concentration $M$ [mole / Liter]
Na <sup>+1</sup>	0.137
Cl <sup>-1</sup>	0.139
K <sup>+1</sup>	0.002
H <sub>2</sub> PO <sub>4</sub> <sup>-1</sup>	0.01
HPO <sub>4</sub> <sup>-2</sup>	0.01

The electrical double layer accumulates electrical energy as a capacitor. If the period of the applied AC field is much higher than the charge relaxation time of the medium, then the double layer can be in local quasiequilibrium. As a result, the double layer can be considered to behave as an ideal capacitor [Gunning 1995].

At frequencies which are higher than the characteristic frequency of the bulk solution, the voltage is dropped entirely across the bulk solution due to the shortcut of double layer capacitor, while at frequencies lower than  $f_c$  the voltage is almost dropped across the electrical double layer [Schwan 1968, Bard 1980]. In our case, the  $f_c$  is 3.85 MHz for a PBS solution with a conductivity of 0.011 [S/m] and relative dielectric constant of 78.5. However, the operating frequency of the electrical sensor is much lower than the characteristic frequency  $f_c$  of the PBS solution. Under this condition the double layer will work in a capacitive manner.

## 7.4.2 Thickness of layers determination

A succession of measurements with the same sensor was carried out to verify the certainty of the effect of the electrical double layer, which possesses a definitive influence upon the liquid sensing. Apart from the experiments in the last chapter, these four

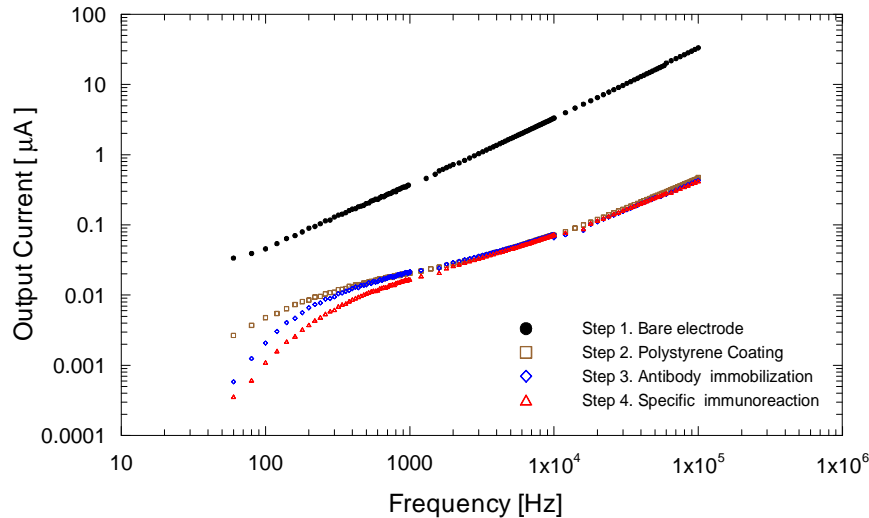
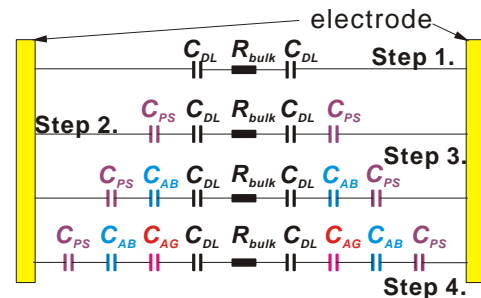


Fig.7-7 (above) Output current versus frequency of the applied voltage for the two-electrode sensor. The curves were measured after each preparation step. The applied voltage was  $0.2 V_{rms}$ . (Right) Electrical equivalent circuit for each preparation step. For each step, the circuit can be treated as the bulk impedance  $R_{bulk}$  connected with corresponding capacitors in series.



measurements were performed in the frequency domain after every preparation process (Fig.7-7). First of all, in step 1, the output currents of the pure PBS solution in a wide frequency range was measured using a two-probe sensor, which did not have any coating on its electrodes. Next, in step 2, after the polystyrene coating, the same measurement was done again by the same sensor. The third (step 3) and last measurements (step 4) were made after the immobilization of the probe antibodies and the specific immunoreaction respectively. Between each step, the sensor was washed by PBS carefully, followed by drying with compressed nitrogen.

At 100 Hz, for example, the impedances of each process were calculated. At a frequency of 100 Hz, the total impedance measured by the bare electrode sensor was  $4.66 M\Omega$ , which is composed by the series of two double layer capacitances  $C_{DL}$  and a connected in series with bulk resistance  $R_{Bulk} = 6.7 k\Omega$  and bulk capacitance  $C_{Bulk} = 131 nF$ , which are measured at 100 Hz by an impedance meter. According to the equivalent circuit shown in the lower figure of Fig.7-7 the calculated value of double layer capacitance  $C_{DL}$  is 483 pF, by which the corresponding thickness of double layer  $I_D$  is 19.06 nm, which is quite close to the theoretical value 20 nm. According this model, the calculated capacitances of the polystyrene coating ( $C_{PS}$ ), immobilized probe antibodies ( $C_{AB}$ ) and specific antibody- antigen reaction ( $C_{AG}$ ) are 42 pF, 25 pF and 20 pF.

Apparently, the immobilization of probe antibodies results in a similar change in capacitance as the change due to specific antibody-antigen reaction. This is understandable as the thickness changes in both processes are comparable, resulting in a 47% change in total impedance. According to equation (5-2), the sensitivity of this 2-probe sensor is 19 %, exactly reaches three fourth its maximal value ( $S_{\max}=25\%$ ).

The capacitance is directly related to the thickness of the protein layer developed on the sensor surface. Because the exact permittivity of the antibody used for these measurements is unknown, we assume that the permittivity of the antibody is 2, which is the lowest possible value for protein molecules, and the total area of the electrodes is homogeneously covered by the probe antibodies and the specific antigens. Under this assumption, during the immobilization and immunoreaction, the thickness changes estimated from the  $C_{AB}$  and  $C_{AG}$  are still twice as large as the size of an antibody: The calculated thickness of the antibody layer is 9.05 nm, and 11.48 nm for antigen layer, which are quite close to the dimension of an antibody molecule (8 ~ 10 nm). This indicates that the efficiency of immobilization of probe antibodies is optimal.

But if the permittivity of antibodies is assumed to be 5, then the results above are different: A layer of thickness which doubles the dimension of an antibody molecule is obtain.

The reason for this inaccuracy might be as follows: From the electric equivalent circuit model described in the chapter 5, the more antibodies are immobilized on the planar electrode, the more capacitance the system will have. The calculated thickness is based on the assumption that the total sensing area is covered by the layers of antibody and antigen. The thickness is inversely proportional to the area for a given capacitance, which means the effective area has not been covered. The reasons that caused this inefficiency may be follows:

- A.** The mechanism of antibody immobilization on polystyrene is physical attachment, such as Van der Waals forces and hydrogen bonds. Thus, these bindings are easier broken than the covalent bonds, while the environment conditions vary.
- B.** The immobilized antibodies are denatured by the non-uniform forces described in the previous sections.
- C.** While applying an external electric field, the antibodies cannot easily reach the proper position on the detecting area at the surface of the sensor due to the forces described in the above sections. The worst one is electro-osmosis force in the following sub-section.

### 7.4.3 Electro-osmosis

Again, for a parallel planar electrode pair like the 2-probe sensor, the applied AC voltage constructs both spatial and time depending non-uniform electric fields [Fig 7-8].

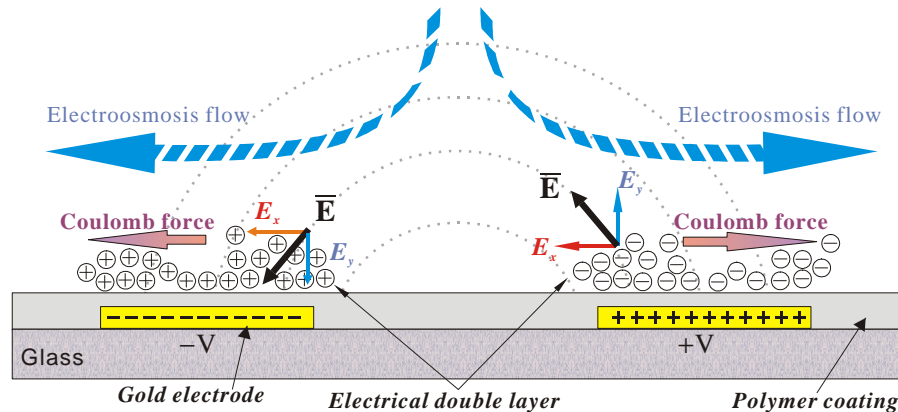


*Fig.7-8 Schematic representation for the electro-osmosis flow in liquid. The applied voltage induces a non-uniform electric field in liquid which gives rise to a Coulomb force which will continuously push the ions in the electrical double layer.*

The time required to form an electrical double layer is of the order of the charge relaxation time  $\tau$  of the solution [Bockris 1977], implying that whenever the frequency of the applied voltage is lower than the characteristic frequency  $f_c = 1 / 2\pi\tau$ , the charges in the double layers alternate with each half cycle of the applying AC voltage.

The tangential part of the electric fields distributed in the liquid produces Coulomb forces acting on the charges in the double layers. The directions of the Coulomb forces are from the center of the electrodes out to both sides of the electrodes. Although the polarization of the electrodes changes with the time varying voltage, the directions of the Coulomb forces remain unchanged, because the induced charges in electrical double layers and applied AC field alternate together. These Coulomb forces drag the ions away from the surface of the electrodes and give rise to an inner liquid flow which interferes with the formation of the double layers. This kind of movement of the liquid is called AC electro-osmosis.

For a small electrode gap, the electrical current fluxes between two separated polarized planar electrodes of the same size are shown in Fig.7-9. The current flux tubes are parallel and the electric field lines are along the circumferences of the flux tubes, which is semicircular if the distortion of the field lines at the edges of the electrodes is ignored.

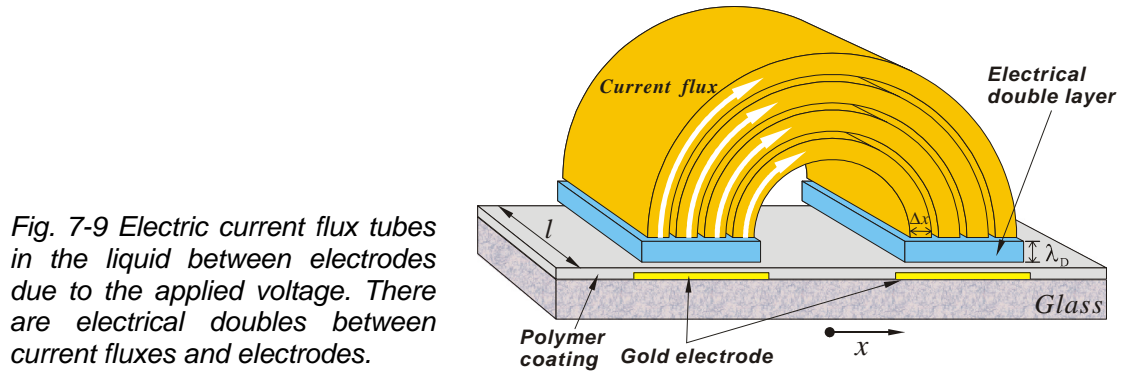


Fig. 7-9 Electric current flux tubes in the liquid between electrodes due to the applied voltage. There are electrical doubles between current fluxes and electrodes.

Since the frequency is lower than the characteristic frequency and the applied voltage is too low to induce the ionization of bulk solution, the double layer will keep stable and behaves in a capacitive manner. For simplification, the impedance of the bulk solution is assumed to be resistive; thus, the impedance of the whole system is composed of resistance of the bulk solution and the double layer capacitance. The capacitance of the double layer at each end of the flux per unit length of the electrode is given by

$$\Delta C_{DL} = \epsilon_m \frac{l \Delta x}{l_D} \quad (7-27)$$

where  $\epsilon_m$  is the permittivity of the medium,  $l$  is the length of the electrode. Note that the electric fields induced in the medium by applied voltage  $V = V_0 \exp(i\omega t)$  are spatially non-uniform, so the voltage dropped across the double layer is a function of position on the electrode and can be written as

$$V_{DL}(x) = V - I \left( R_B(x) + \frac{1}{i\omega \Delta C_{DL}} \right) = \frac{V}{2} \frac{1}{\left( 1 + \frac{\omega \epsilon_m \rho x}{2l_D s} i \right)} \quad (7-28)$$

where  $R(x) = \rho x / s l_D x$  is the resistance of each tube, and  $I$  is the total current through the bulk and is equal to  $V$  divided by the total impedance of the system. The resulting horizontal field above the electrodes is given by

$$E_H(x) = \frac{d}{dx} V_{DL}(x) = \frac{V}{2} \frac{i \omega \epsilon_m \rho / 2l_D s}{\left( 1 + i \omega \epsilon_m \rho x / 2l_D s \right)^2} \quad (7-29)$$

It is this tangential field that induces the movement of the ions accumulated in the double layer. If the viscous drag across the layer per unit area  $F_{vis}/A$  is equal to the electrostatic force, then the velocity of the ions and corresponding fluid flow  $\mathbf{u}_{DL}$  is determined [Brown 2000]:

$$\frac{F_{vis}}{A} = \mathbf{r}_{DL} E_H = \mathbf{h} \frac{\mathbf{u}_{DL}}{l_D} \quad (7-30)$$

where  $\mathbf{r}_{DL} = V_{DL} \Delta C / \Delta x = \epsilon V_{DL} / l_D$  is the charge density of ions in the double layer and

$h$  is the viscosity of the water. So the velocity of the ions due to the Coulomb force is

$$\mathbf{u}_{DL} = \mathbf{I}_D \mathbf{r}_{DL} E_H / h \quad (7-31)$$

Therefore, at the position  $x$ , the average velocity of the ions above the electrode can be estimated as

$$\langle \mathbf{u}_{DL}(x) \rangle = \frac{1}{2} \operatorname{Re} \left\{ \frac{\mathbf{I}_D \mathbf{r}_{DL} E_H^*}{h} \right\} = -\frac{e_m V_0^2}{8hx} \frac{(wx/w_0)^2}{[1 + (wx/w_0)^2]^2} \quad (7-32)$$

where  $w_0 = 2I_D s / e_m p$ . At the inner edge of the electrodes, the calculated velocity of the fluid flow in our case is about 1.28  $\mu\text{m}$  per second, with the direction from the center of the gap to the outer edge of the electrode, where the velocity reduces to 1.23  $\mu\text{m}$  per second, however. This implies that the inner fluid flows are quite strongly and it can sweep over the whole surface in 30 seconds. The flow patterns due to the interaction of the non-uniform field and the electrical double layer at different frequencies were

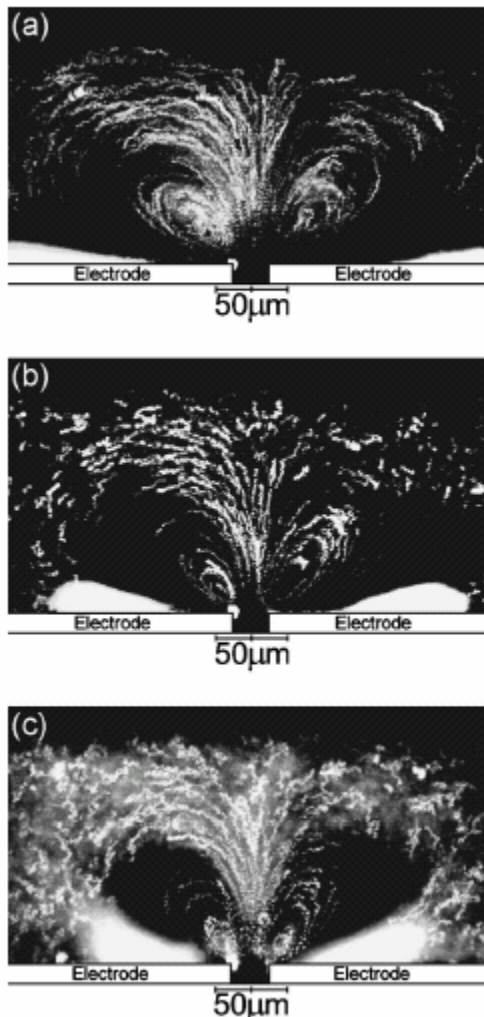


Fig.7-10 The camera images of internal fluid flows between two planar electrodes at (a) 100 Hz (b) 300 Hz and (c) 1000 Hz by Green *et al* [Green 2000].

recorded by Green *et al* [Green 2000] and are shown in Fig.7-10. The flow tracks were clearly in symmetric rolls above the electrodes with the highest velocity at the inner edges of the electrodes. The particles in the bulk solution will be dragged by this electro-osmosis flow from the center top of the bulk to the center bottom near the inner edges of the electrodes and then be pulled through the whole area of the electrode and back to the top of the bulk solution to circulate repeatedly.

As a result, if the antigens (in our case they are also antibody molecules) are added to the bulk solution of PBS, they will also be dragged by the movement of the inner fluid flow. It is reasonable to conclude that if the antigens are captured by the immobilized antibodies on the sensor surface, the structure of the electrical double layer will be temporarily destroyed, since the size of the antibody molecule and the thickness of the electrical double layer

are comparable. The reconstruction of the double layer could be completed after the immunoreactions are finished. This electro-osmosis flow can also account for the deviation between double layer calculated from the measurements in section 7.4.2 and the theoretical value. As long as the electro-osmosis flow continues, the thickness of the double layer will never be fixed.

The non-specific antigens or excess specific antigens will continue to drift circularly with the electro-osmotic flow. However, some specific antigens which are already captured by the antibodies may also be broken away from the antibodies, if the binding between antibody and antigen can not resist the drag force by the electro-osmotic flow after a long duration. This can be seen in Fig.7-11, which shows that after a long time of measurement the current started to increase spontaneously. Of course this increase of the current may be caused by the evaporation of the water in the bulk solution, which gives rise to a higher ionic concentration and simply enhances the electric current. Even though, the increase of the salt concentration of the bulk solution degrades the resistance of the bulk solution and results in a higher voltage drop across the double layer, and causes a faster electro-osmosis flow. The antibodies and antigens could be dragged out of the solid phase to the bulk solution by this faster internal liquid flow.

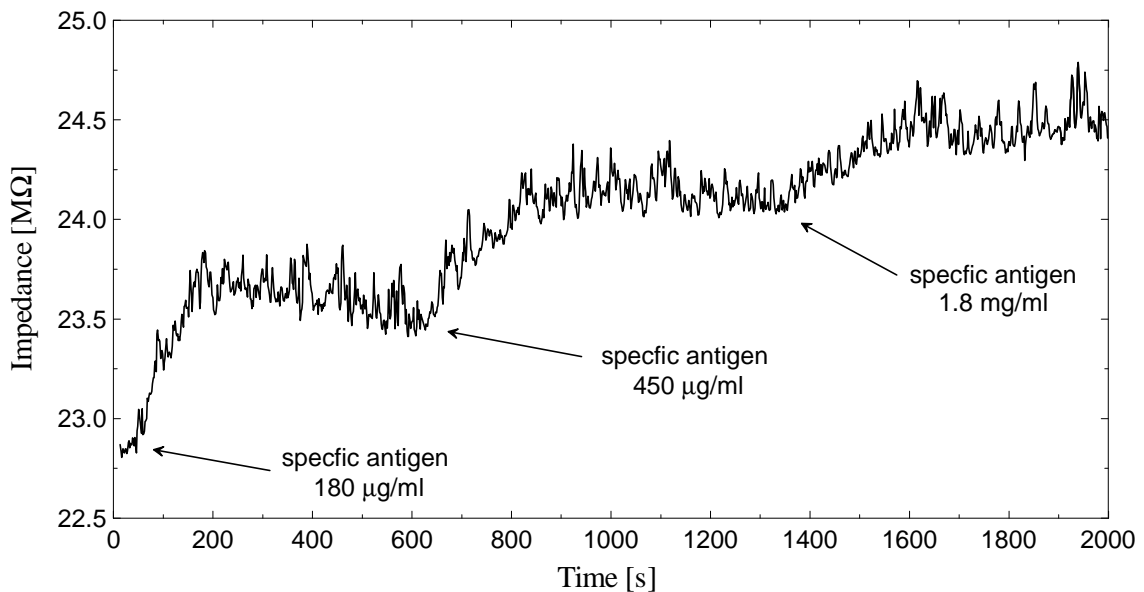


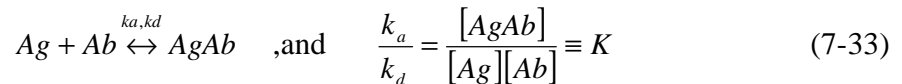
Fig.7-11 Impedance of a two-electrode sensor at high input voltage (1 V at 137 Hz) while specific immunoreaction progresses. It is demonstrated that at such a high input voltage the output signal zigzags seriously during the whole measurement and drifts downward after hundreds of seconds. This can be attributed to the instability in the liquid, such as strong electro-osmosis flow induced by high input voltage. The impedance change is 3.4% with a noise level 1.7%, corresponding to a capacitance change in 28.2 nF/mm<sup>2</sup>.

From equation (7-32), the electro-osmosis flow velocity depends directly on the liquid permittivity and the square of both the amplitude and the frequency of the applied signal

From this discussion it can be concluded that the stability of the sensor response is strongly influenced by the interaction of electric field and double layer. For example, during the immunoreaction, the electro-osmosis force will cause the destruction and reconstruction of the double layer due to the coupling of the tangential component of the applied electric field and the charges which accumulate in the electrical double layer.

## 7.5 Binding kinetics of immunoreaction

As discussed in chapter 2, the antibody (Ab) - antigen(Ag) reaction is reversible. When the rates of association ( $k_a$ ) and dissociation ( $k_d$ ) approach an equilibrium, the reaction can be expressed by the law of mass action:



where  $[\ ]$  denotes the concentration of the reactants or products,  $K$  the equilibrium constant is defined as the ratio of association and dissociation rate. The typical  $K$  of an immunoreaction is between  $10^5 \dots 10^9$  l/mol [Absolom 1986, Roitt 1996]. In the cases of the SAW and electrical biosensors, the object antigens are suspended in the solution while the probe antibodies were immobilized on the sensor surface, so we defined an adsorption rate ( $r_a$ ) and desorption rate ( $r_d$ ):

$$r_a = k_a \cdot [Ag] \cdot r_s \cdot (1 - \Theta), \quad r_d = k_d \cdot r_s \cdot \Theta \quad (7-34)$$

where  $r_s$  is the surface density of the binding sites provided by the immobilized probe antibodies,  $\Theta$  is the proportion of the occupied binding sites. In the equilibrium state, the  $r_a$  equals  $r_d$  and the fraction of occupied binding sites  $\Theta_{eq}$  is

$$\Theta_{eq}([Ag]) = \frac{K \cdot [Ag]}{1 + K \cdot [Ag]} \quad (7-35)$$

In the case of the SAW sensor, it is assumed that: (a) The phase shift ( $\Delta j$ ) of the surface wave depends on the captured antigen molecules on the surface, and (b) the required surface area for each captured object antigen is constant. In equilibrium, the ratio of occupied area ( $F_{eq}$ ) and the maximal area of active binding sites ( $F_{sat}$ ) are related to the phase shift:

$$\begin{aligned} \frac{F_{eq}([Ag])}{F_{sat}} &= \Theta_{eq}([Ag]) = \frac{\Delta j([Ag])}{\Delta j_{sat}} \\ \Rightarrow \Delta j([Ag]) &= \Delta j_{sat} \cdot \frac{K[Ag]}{K[Ag]+1} \end{aligned} \quad (7-36)$$

where  $Dj_{sat}$  is the maximal phase shift of a SAW sensor. Fig.7-12(a) shows the comparison of phase shifts for different antigen concentrations. It should be noted that the concentration indicated here is the concentration *in situ*, i.e. the concentration after the antigen solution was pipetted onto the sensing area of the sensor, not the concentration in the test tubes. Fig.7-12 shows the fit curves with respect to the data from Fig.7-12(a) equation (7-36). The fitting equilibrium constant  $K = 3.4 \times 10^5$  l/mol. According to the data shown in Table 2-1, this equilibrium constant corresponds to a nearly monovalence antibody-antigen reaction, indicating that the binding capacity for an antibody molecule in these measurements was not saturated since for an IgG molecule the maximal effective valence is 2.

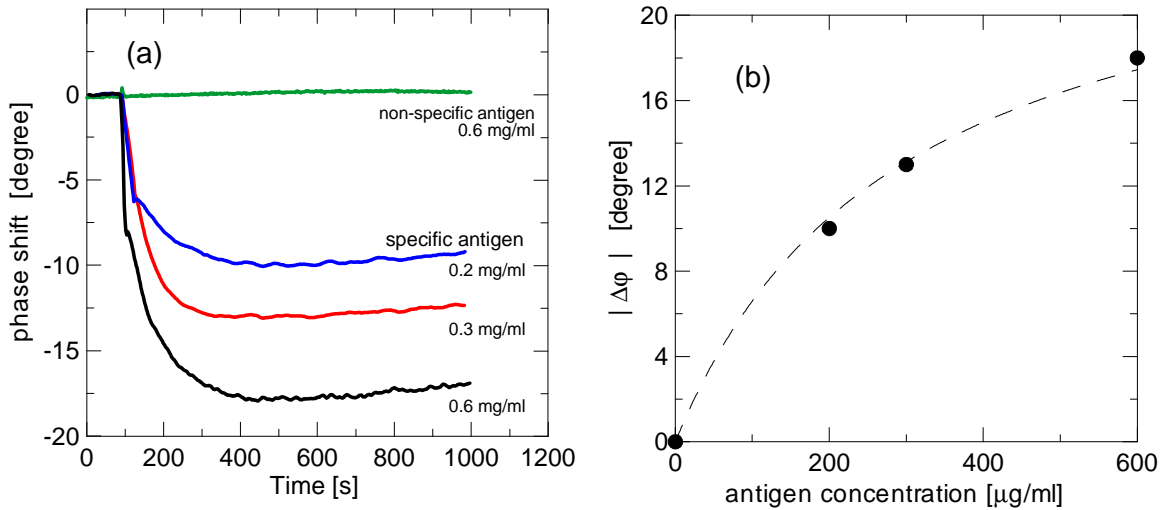


Fig.7-12 (a) Phase shifts measured with SAW sensors due to the specific antibody-antigen reaction. (b) The fitting curves of phase shifts versus antigen concentration gives an equilibrium constant of  $K=3.4 \times 10^5$  l/mol. More measurements with much lower antigen concentration are necessary to prove the accuracy.

For the electrochemical sensor, Fig.7-13(a) shows the normalized current changes with different concentrations of probe antibody solutions. The reaction time coincides with the results from measurements from the SAW sensor [Fig.7-12(a)]. It is assumed that the normalized current change is defined by  $g \equiv \Delta i/i_0$ , then the impedance change with respect to the  $g$ , is

$$\left| \frac{\Delta z}{z_0} \right| = \left| \left( \frac{1}{g} - 1 \right) \right| \quad (7-37)$$

where  $z_0$  is the initial impedance before immunoreaction. From our experiments, the

maximal impedance change is  $47\% \approx 1/2$ , i.e.  $D_{z_{sat}} = Z_0/2$ . Likewise, the impedance of the sensor depends on the area of antigen coverage on the surface, the more area is covered, and the higher is the impedance. Hence, equation (7-37) is related to (7-36)

$$\frac{\Delta z([Ag])}{z_0} \approx \frac{\Delta z([Ag])}{2 \cdot \Delta z_{sat}} = \frac{\Theta_{eq}([Ag])}{2} \quad (7-38)$$

$$\Rightarrow \frac{\Delta z([Ag])}{z_0} = \frac{1}{2} \cdot \frac{K[Ag]}{K[Ag]+1} = \left| \left( \frac{1}{g} - 1 \right) \right|$$

The normalized impedance change corresponding to the current change is shown in Fig.7-13(b). The solid curve is a fit to the above equation. This fitting gives the equilibrium constant  $K = 5 \times 10^6$  [l/mol], which is almost consistent with the bivalent antibody in the literature [Table 2-2].

So far, from the above measurements and theoretical calculations, it is evident that the immunosensors developed in this work have operated successfully in the laboratory. Both, the SAW and the electrochemical sensors, are suitable for qualitative and quantitative measurements, demonstrating a great potential for utilization in clinical application.

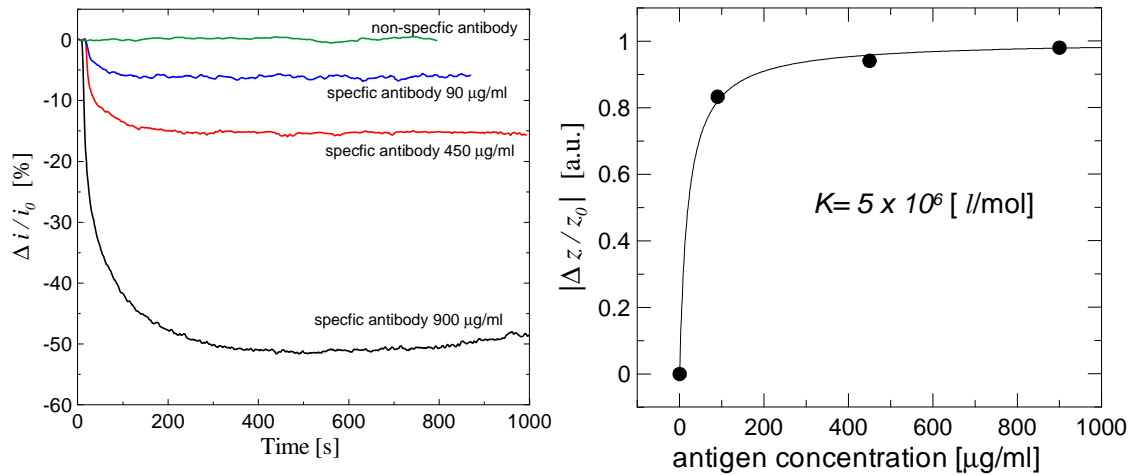


Fig.7-13 (a) Measurements with different antigen concentrations for a two-probe sensor. The maximal current change is about 50%. (b) The fitting curve is based on the data in Fig.7-13(a). The equilibrium constant is  $5 \times 10^6$  [l/mol], corresponding to a bivalent antibody.

# Chapter 8

## Summary and Prospect

In this work, immunosensors based on surface acoustic waves have been developed for monitoring the antibody-antigen interaction. Surface acoustic waves are ultrasonic waves propagating at the surface of a substrate that are highly sensitive to the variations in physical and chemical characteristics of the substrate surface since the energy of the ultrasonic waves concentrates within several wavelengths from the surface. Mass change due to the deposition of antibody-antigen complexes results in an additional stress on the surface and perturbs the wave propagation, so that the velocity and amplitude of the wave will be reduced.

For the application of SAW sensors in the liquid environment, shear-horizontal (SH) polarized acoustic wave has a definitive advantage because the SH-wave prevents the emission of acoustic energy into the liquid owing to the fact that the displacements of substrate elements near the surface are parallel to the liquid-solid interface. In this work, SH-waves were generated by applying RF-signals to the interdigital transducers (IDTs) which were arranged on the surface of  $36^\circ$  rot YX-cut  $\text{LiTaO}_3$  substrate. In order to protect the IDTs, a thin  $\text{SiO}_2$  layer with a thickness of  $1\ \mu\text{m}$  was deposited on the whole surface, so that the IDTs were covered. The  $\text{SiO}_2$  layer not only ensures the IDTs from aggressive solutions, but also guides the waves to propagate and localize at the  $\text{SiO}_2$ - $\text{LiTaO}_3$  interface. These guided waves on the surface are called “Love waves”, which have a velocity slower than that of all other bulk waves; therefore, Love waves are not interfered by the bulk waves and preserve their energy from decaying into the substrate. From the theoretical calculation, the longitudinal and shear-vertical components of the waves are minimized when  $1\ \mu\text{m}$   $\text{SiO}_2$  thin layer is utilized as the waveguide. The high dielectricity and conductivity of aqueous solutions which affect the substrate piezoelectricity are for the most part shielded by the  $\text{SiO}_2$  layer.

To simplify the production process of the sensor, an inductively coupled contactless immunosensor has been developed. With this design, the surface coating with either  $\text{SiO}_2$  or polymer is easily achieved since the junction areas between leads and IDTs do not exist any more.

Surface modification is required for the reason that probe antibodies have to be immobilized on the sensing area to reach the maximal binding capacity. With the help of protein A and gold layer the probe antibodies were orientated on the surface, so that the  $F(ab')_2$  fractions of antibodies are toward upwards. An alternative is Polymethyl methacrylate (PMMA) coating, which adsorbs the antibodies through physical attachment. Without the surface modification, the maximal phase shift happened only when the concentrations of the antibody and antigen are the same, although only about 2/3 of the maximal phase shifts were obtained.

The operation frequency of the inductively coupled SAW immunosensor was 435 MHz. The measured insertion attenuation are between -20 dB (PMMA coating) to -30 dB ( $SiO_2$  coating) loaded with buffer solution (PBS). The sensitivity of the SAW sensor is for the moment  $21 \text{ pg/mm}^2$ , accompanying with a noise level of corresponding mass sensitivity  $3 \text{ pg/mm}^2$ . The detectable limit should be improved to  $9 \text{ pg/mm}^2$  when it is assumed that the reliable detecting limit is three times greater than the noise level.

Another type of immunosensors developed in this work was the electrochemical sensor, which is based on the detection of the conductive property in a liquid-biomolecular layer system. It was done by use of two or four planar electrodes on glass substrate. Likewise, a thin polymer film of either PMMA or Polystyrene (PS) was coated on the sensor surface to protect the electrodes from aggressive solutions. The AC signals couples between electrodes capacitively since the polymer layer insulates the surface. When antibody-antigen complexes form a bilayer on the surface, the impedance of the total system increases because the layer becomes thicker.

For the two-electrode setup, an AC voltage source with constant amplitude was sent to the sensor. The resulting changes in output current were measured by a transimpedance amplifier circuit, which can convert the output currents into voltage signals. It has extremely high input impedance ( $10^{12} \Omega$ ) so as to avoid loading the sensor. Hence, even a tiny current can be measured. For four-electrode setup, the current changes were measured from two outer electrodes using a transimpedance amplifier, while an instrumentation amplifier circuit was utilized for monitoring the voltage difference between two inner electrodes. The instrumentation amplifier has the advantages of, first, the extremely high input impedance ( $10^{12} \Omega$ ); second, the high common-mode rejection ratio (110 dB at 200 Hz), so that only the voltage difference will be amplified, while the common-mode signals will be filterer out; and third, arbitrary output gain can be controlled by only single resistor.

The measurements with PBS solution using bare electrodes indicate that four-probe sensor suppresses the contribution of the capacitance; therefore, two-probe system is suitable for measurements of capacitive properties of a dielectric layer. Moreover, in high frequency range (above 10 kHz), liquid dominants the total impedance, while at low

frequencies the capacitive insulating layer dominates. So the measurements were carried out at very low frequencies around 100 Hz. The sensitivity of the electrochemical sensor is 0.19 for a 47% change in impedance. The minimal detectable limit is 20.6 nF / mm<sup>2</sup> for a 3.4 % change in impedance with a noise limit 303.8 nF/mm<sup>2</sup>.

The effective sensing area of an electrochemical sensor is the surface directly over the electrodes. It is quite the contrary to the SAW immunosensor, whose sensing area is on the delay path between two sets of IDT. Therefore, in the case of electrochemical sensor, either the composed ions of buffer solution or biomolecules (antibodies and antigens) are subject to the electric fields, which are generated from the applied voltage and have high strength directly above the electrode. The maximum strength of the electric fields is at the electrode edges. Hence, particle movements due to the influence of the electric fields have to be considered. The molecule movement induced by:

- A. dielectrophoretic forces, which is caused by the interaction between two substances with different dielectric constants under non-uniform electric field,
- B. AC electrohydrodynamic forces, which is caused by the Coulomb, dielectric forces and electrical heating,
- C. convection and Brownian motion

are negligible small. The most influential is the AC electro-osmosis forces, which is induced by the interaction between AC electric fields and electrical double layer. This force pushes the ions in the double layer to move parallel to the surface, i.e. from the middle gap to outer edges of the electrodes. This movement is quite fast and produces a vortex in the bulk solution above each electrode. Antibody molecules will therefore move accompanying with the AC electro-osmosis flow and have a velocity of 1.28  $\mu\text{m}$  per second at the edge near the gap. With this speed an antibody molecule sweeps through the electrodes in 30 seconds. It is speculated that the AC electro-osmosis force is the reason for the noise and unstable behaviors of the electrochemical sensor. SAW sensors do not have this problem since

- A. the antibody and antigen molecules are located mainly above the delay line away from the IDT electrodes,
- B. the electric fields accompanying with the surface acoustic wave on the delay line are too weak to induce osmosis flow,
- C. the operation frequency of the SAW sensor is higher than the charge relaxation frequency, the electrical double layers do not exist at such high AC frequency.

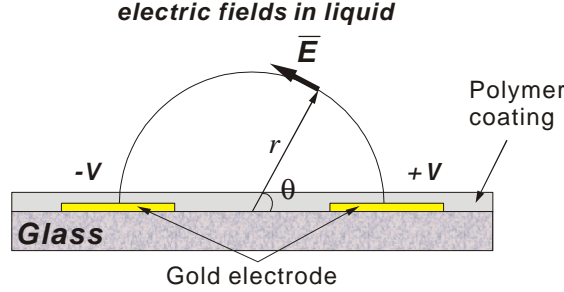
The equilibrium constant  $K$  of antibody-antigen immunoreaction has been summarized from the concentration-depending phase shifts (SAW sensor) and impedance

change (electrochemical sensor). The  $K_{SAW} \approx 3.4 \times 10^5$  l/mol indicates a nearly monovalent immunoreaction, while the  $K_{electro.} \approx 5.0 \times 10^6$  l/mol implies an approximately bivalent antibody-antigen reaction.

Both of SAW and electrochemical sensors are feasible for qualitative detection for their high specificity. They are also qualified to perform accurate quantitative measurements, such as the determination of binding constant of two biomolecules. But there are many factors which influence the electrical properties at the sensor surface and readout signals; for example, AC electro-osmosis flow, double layer capacitance, parasitic capacitance within the leads and cables; therefore, the requirements of an electrochemical sensing system is higher than a SAW sensor and restrict the prevalence.

The sensitivity of both sensors can be improved further. For example, SAW sensors with higher operation frequencies in gigahertz range are necessary to improve the mass detection limit. Next, instead of using whole IgG molecules, measurements with various subsections of antibody molecules, which have different molecular weight, are also recommended to exam and calibrate the sensitivity. For electrochemical devices, material of high permittivity and an ultra thin insulating layer is demanded in order to increase the background capacitance. Besides, antibody immobilization with long chain orientated polymer, which provides a more specific, covalent, and well-arranged binding, or conductive polymer, which is sensitive to the electrical responses, are worth to proceed. In addition, AC electro-osmosis flow can be also employed to setup a micro pump or liquid propeller for the integrated sensing system on a single chip (Lab-on-a-chip), micro total analysis systems ( $\mu$ -TAS), and micro-electro-mechanical systems (MEMS) since it is easy to construct a microfluidic flow by simple electrodes and AC fields. Then, a total automation micro sensing system for clinical, educational and industrial purpose will be achieved.

# Appendix A



The force induced by a pair of planar electrodes in liquid can be derived as follows:  
The electric field results from the electrodes with potential  $V$  at position  $(r, \mathbf{q})$  is

$$\vec{E}(r) = \frac{V}{\rho} \frac{1}{r} \hat{n}_q \quad (\text{A-1})$$

and the power dissipated per unit volume is

$$W(r) = \mathbf{s} \cdot E^2 = \frac{\mathbf{s}V^2}{\rho^2} \frac{1}{r^2} \quad (\text{A-2})$$

Substituting these equation into equation (7-9) gives

$$\frac{k}{r} \frac{\partial}{\partial r} \left( r \frac{\partial T}{\partial r} \right) + \frac{k}{r^2} \frac{\partial^2 T}{\partial q^2} = -\frac{\mathbf{s}V^2}{\rho^2} \frac{1}{r^2} \quad (\text{A-3})$$

A particular solution to the above is  $T_p = -\frac{\mathbf{s}V^2}{2\rho^2} \frac{q^2}{k}$  and the general solution is

$$T(\mathbf{q}) = -\frac{\mathbf{s}V^2}{2\rho^2} \frac{q^2}{k} + \frac{\mathbf{s}V^2}{2\rho} \frac{q}{k} \quad \text{with} \quad T_{\max} = T\left(\frac{\rho}{2}\right) = \frac{\mathbf{s}V^2}{8k} \quad (\text{A-4})$$

which satisfies the boundary condition  $q=0$  and  $q=\rho, T=0$ , i.e. the electrode is assumed to be thermal baths, and the reference temperature is set to be zero. The time averaging AC fields causes a gradient of temperature

$$\nabla T = \frac{\mathbf{s}V^2}{2\rho k} \left( 1 - \frac{2q}{\rho} \right) \frac{1}{r} \hat{n}_q \quad (\text{A-5})$$

Substituting (A-5) into equation (7-20) with the relation  $\nabla \mathbf{s} = \frac{\partial \mathbf{s}}{\partial T} \nabla T$  and  $\nabla \mathbf{e} = \frac{\partial \mathbf{e}}{\partial T} \nabla T$

the time averaged force with an applied AC voltage  $V_{rms}$  is

$$\langle f_E \rangle = -M(\mathbf{w}, T) \left( \frac{\mathbf{e} \mathbf{s} V_{rms}^4}{8k \rho^3 r^3 T} \right) \left( 1 - \frac{2q}{\rho} \right) \hat{n}_q, \quad \text{where} \quad M(\mathbf{w}, T) = \left( \frac{\frac{T}{\mathbf{s}} \frac{\partial \mathbf{s}}{\partial T} - \frac{T}{\mathbf{e}} \frac{\partial \mathbf{e}}{\partial T}}{1 + (\mathbf{w}t)^2} + \frac{1}{2} \frac{T}{\mathbf{e}} \frac{\partial \mathbf{e}}{\partial T} \right) \quad (\text{A-6})$$



# Reference

Alder R., *Simple theory of acoustic applications*, IEEE Transactions on Sonics and Ultrasonics, **SU-18**, p.115-118, 1971

Auld B.A., *Acoustic fields and waves in solids, vol. I*, 2<sup>nd</sup> edition, Krieger Publishing Company, Florida 1990

Bagotzky V.S., *Fundamentals of Electrochemistry*, Plenum Press, London 1993

Bakewell D.J.G., Hughes M.P., Milner J.J., Morgan H., *Dielectrophoretic Manipulation of Avidin And DNA*, Proc. 20th Annual International Conference of the IEEE Engineering in Medicine and Biology Society. 1998

Bard A.J., Faulkner L.R., *Electrochemical Methods: Fundamentals and Applications.*, Wiley, New York, 1980.

Beck K., *Induktive Anregung und Detektion von Oberflächenwellen: Entwicklung und Anwendung eines neuen Konzepts für die Gassensorik*, Dissertation, Institut für Angewandte Physik, Universität Heidelberg 1999

Becker F.F., Wang X.B., Huang Y., Pethig R., Vykoukal J., Gascoyne P.R.C., *Separation of human breast cancer cells from blood by differential dielectric affinity*, Proc. Natl. Acad. Sci. USA, **92**, p.860-864, 1995

Bockris J.O'M., *Electrochemistry*. Plenum Press, New York, 1977

Bousse L., Bergveld P., *On the impedance of silicon dioxide/electrolyte interface*, Journal of Electroanalytical Chemistry, **152**, p.25-39, 1993

Burr-Brown, *Instrumentation Amplifiers: Versatile Differential Input Gain Blocks*, Application Note AN-75, Burr-Brown Handbook of Linear IC Application, Burr Brown, Tucson, AZ, 1987

Einstein A., *On the movement of small particles suspended in a stationary liquid demanded by the molecular kinetics theory of heat*, Annals of Physics, **Leipz. 17**, p.549-560, 1905

Fasold W., Kraak W., Schirmer W., *Taschenbuch Akustik*, VEB Verlag Technik, Berlin 1984.

Franco S., *Design with operational amplifiers and analog integrated circuits*, 3<sup>rd</sup> edition, Mc Graw Hill, New York 2002

Gebbert A., Alvarez-Icaza M., Stöcklein W., Schmid R.D., *Real-time monitoring of immunochemical interactions with a tantalum capacitance flow-through cell*, Analytical Chemistry, **64**, p.997-1003, 1992

Gentes W., *Numerische Berechnung von Schallwellen in piezoelektrischen Schichtsystemen*,

- Diplomarbeit, Institut für Angewandte Physik, Universität Heidelberg 1994
- Green, N.G., Ramos A., Morgan H., *AC electrokinetics: a survey of sub-micrometre particle dynamics*, Journal of Physics D: applied physics, **33**, p.632-641, 2000
- Green N.G., Ramos A., Gonzalez A., Morgan H. and Castellanos A., *Fluid flow induced by non-uniform AC electric fields in electrolytic solutions on micro-electrodes. Part III: Numerical simulation and streamlines*. Physical Review E, **66**, p.026305, 2002
- Gunning J., Chan D.Y.C., White L.R., *The Impedance of the Planar Diffuse Double layer: An Exact Low-Frequency Theory*, Journal of Colloid Interface Science, **170**, p.522-537, 1995
- Harlow E., Lane D., *Antibodies - A Laboratory manual*, Cold Spring Harbor Laboratory. 1988
- Hoffmann J., *Immunosensorik mit Akustischen Oberflächenwellen*, Diplomarbeit, Institut für Angewandte Physik, Universität Heidelberg 1999
- Hughes M.P., Morgan H., *Dielectrophoretic Manipulation of Single Sub-micron Scale Bioparticles*, Journal of Physics D: applied physics, **31**, p.2205-2210, 1998
- Hunter R.J., *Foundations of Colloid Science*, Clarendon Press, Oxford 1987.
- Josse F., Shana Z.A., *Acoustoionic Interaction of SH surface waves with dilute ionic solutions*, IEEE Trans. Ultrasonics, Ferroelectrics and Frequency control, **38**, p.297-304, 1991
- Karki J., *Effect of parasitic capacitance in OP AMP circuits*, Application Report of Texas Instruments, September 2000.
- Kittel C., *Elementary Statistical Physics*, Wiley, New York, 1965
- Kohlrausch F., *Praktische Physik*, Teubner Verlag, Stuttgart 1986
- Kondoh J., Shiokawa S., *A liquid sensor based on a shear horizontal SAW device*, Electronics and communications in Japan, part 2, **76**, No. 2, 1993
- Landau L.D., Lifschitz E.M., *Lehrbuch der theoretischen Physik. Elastizitätstheorie*, Akademie Verlag, Berlin 1975.
- Lewis M., *Surface skimming bulk waves*, IEEE Ultrasonics Symposium Proceeding, p.744-752, 1977
- Love A.E.H., *Some problems of geodynamics*, Cambridge University Press, 1911
- Morgan H., Hughes M.P., Green, N.G., *Separation of submicron bioparticles by dielectrophoresis*, Biophysical Journal, **77**, p.516-525, 1999
- Müller T., Gerardino A., Schnelle T., Shirley S.G., Bordoni F., DeGasperis G., Leoni R., Fuhr G., *Trapping of micrometre and sub-micrometre particles by high-frequency electric fields and hydrodynamic forces*, Journal of Physics D: applied physics, **29**, p.340-349, 1996

- North J., *Immunosensors: antibody-based biosensors*, Trends in Biotechnology, **3**, p.180-186, 1985
- Penners G., Priel Z., Silberberg A., *Irreversible Adsorption of Triple Helical Soluble Collagen from Solution to Glass and Other Surfaces*. Journal of Colloid and Interface Science, **80**, p.437-444, 1981
- Pethig R. and Kell D.B., *The passive electrical properties of biological systems: their significance in physiology, biophysics and biotechnology*. Physics in medicine and biology, **32**, p.933-970, 1987
- Pitera J.W., Falta M., van Gunsteren W.F., *Dielectric Properties of Proteins from Simulation: The Effects of Solvent, Ligands, pH, and Temperature.*, Biophysical Journal, **80**, p.2546-2555, 2001
- Pohl H.A., *Dielectrophoresis*, Cambridge University Press, Cambridge, UK 1978
- Paul R., Kaler K.V.I.S., *Theory of Electrode Polarization in Dielectrophoresis and Electrorotation*, Journal of Colloid and Interface Science, **194**, p.239-248, 1997
- Ramos A, Morgan H, Green N.G, Castellanos A., *AC electrokinetics: a review of forces in microelectrode structures*, Journal of Physics D: applied physics, **31**, p.2338-2353, 1998
- Ramos A, Morgan H, Green N.G, Castellanos A., *AC electric-field-induced fluid flow in microelectrodes*, Journal of Colloid and Interface Science, **217**, p.420-433, 1999
- Ricco A.J., Martin S.J., Zipperian T.E., *Surface acoustic wave gas sensor based on film conductivity changes*, Sensors & Actuators, **8**, p.319-333, 1985
- Rogers K.R. and Gerlach C.L., *Environmental Biosensors: A Status Report*. Environmental Science & Technology, November 1996.
- Roitt I., Brostoff J., Male D., *Immunology*, 4th edition, Mosby, London, UK 1996.
- Royer D., Dieulesaint E., *Elastic waves in Solid I: Free and guided propagation*, Springer-Verlag, Berlin-Heidelberg 2000
- Sarkar D., Chattoraj D.K., *Activation parameters for kinetics of protein adsorption at Silica-water interface*, Journal of Colloid and interface science, **157**, p.219-226, 1993
- Shiokawa S., Moriizumi T., *Design of SAW sensor in liquid*, Japanese Journal of Applied Physics, **27**, *Supp. 27-1*, p.142-144, 1988
- Smith W.R., Gerard H.M., Collins J.H., Reeder T.M., Shaw H.J., *Analysis of interdigital surface wave transducers by use of an equivalent circuit model*, IEEE Trans. on Microwave Theory and Techniques, **MTT-17**, p.856-864, 1969
- Stratton J.A., *Electromagnetic theory*, Mc Graw Hill, New York, 1941.
- Schwan H.P., *Electrode polarization impedance and measurements in biological materials*.

Annals of the New York Academy of Sciences, **148**, p.191-209, 1968

Tancrell R.H., Holland M.G., *Acoustic surface wave Filters*, Proceedings of IEEE, **59**, p.393-410, 1971

Tilton R.D., Robertson C.R., Gast A.P., *Lateral diffusion of bovine serum albumin adsorbed at the solid-liquid interface*. Journal of Colloid and Interface Science, **137**, p.192-203, 1990

Turner A.P.F., Karube I., Wilson G.S., *Biosensors: Fundamentals and Applications.*, Oxford University Press, Oxford, UK 1987

Viktorov I.A., *Rayleigh and lamb waves*, Plenum, New York, 1967

Wagner J., *Mikrostrukturen*, Diplomarbeit, Institut für Angewandte Physik, Universität Heidelberg 1998

Warsinke A., Benkert A., Scheller F.W., *Electrochemical immunoassays*, Fresenius Journal of Analytical Chemistry, **366**, p.622-634, 2000

Washizu M., Suzuki S., Kurosawa O., Nishizaka T., Shinohara T., *Molecular Dielectrophoresis of biopolymers*, IEEE Transactions on Industry Applications, **30**, p.835-843, 1994

Williamson R.C., *Reflection Grating Filters*, in H. Matthews(ed.): *Surface wave filters*, John Wiley & Sons, New York 1977

Yamanouchi K., *Temperature dependence of Rayleigh waves and piezoelectric leaky surface waves in rotated Y-cut LiTaO<sub>3</sub> and SiO<sub>2</sub>/LiTaO<sub>3</sub> structures*, Wave Electronics, **3**, p.319-333, 1979

# A cknowledgement

Hereby, I am very grateful for those who contributed to the success of this work. Their participation is precious. With all my heart, I would like to thank:

- Professor Dr. S. Hunklinger for the admission in his working group, the assignment of this interesting topic and the valuable discussions during the group discussion.
- Dr. M. von Schickfus for the innumerable and valuable advice and discussions. His complaisance provides an agreeable working atmosphere.
- Dr. J. Wagner for the benignant and kind cooperation, especially in the field of electronics he provides advices.
- Mr. V. Schultheiss and Mr. T. Wolf at the clean room and chemical laboratory for wafer preparation as well as thin film sputtering.
- Mr. P. Frauenfeld at the electronic laboratory and Mr. S. Spiegel at the mechanical workshop for instrumental guidance for the measurement setup.
- Dr. R. Dahint at the Institute of Physical Chemistry and Mr. J. Beimborn at the company Heidelberg Instruments for the bountiful and generous help in the urgent preparation of masks and sensors.
- Dr. C. Müller, Dr. P. v. Bülow, Dr. S. Preuss, Dr. J. Freudenberg, Mr. S. Rupp, Mr. M. Philipp, Ms. S. Wilms and all members from the group of low temperature physics for the comfortable collaboration in the laboratory and good times in Heidelberg.
- Taiwan National Cheng-Kung Foundation and German Academic Exchange Service (Deutscher Akademischer Austausch Dienst, DAAD) for the support of my research and living in Germany in the past four years.

Last, but not least, I wish to express again my appreciation to my families, particularly the warming cares from my wife Wan-chen, who always has patience with me and enheartens me especially during this work. Thank you all honestly!!